Arctic paleoceanography: unraveling the controls on planktic foraminiferal geochemistry to better understand how the Arctic Ocean responds to climate perturbations

By

CAITLIN MARIE LIVSEY
DISSERTATION

Submitted in partial satisfaction of the requirements for the degree of

DOCTORATE OF PHILOSOPHY

in

Earth and Planetary Sciences

in the

OFFICE OF GRADUATE STUDIES

of the

UNIVERSITY OF CALIFORNIA

DAVIS

Approved:

_____

Tessa M. Hill, Chair

_____

David A. Gold

_____

Jennifer Fehrenbacher

Committee in Charge

2021

ACKNOWLEDGEMENTS

I am greatly indebted to many people and organizations that contributed to the completion of this dissertation.

On a logistical note, I am thankful for funding from the Cushman Foundation for Foraminiferal Research, UC Davis Durrell fund, Sigma Xi, and the NSF OCE program. Further, I thank the WiscSIMS laboratory and scientists there who helped with numerous analyses that were vital to my dissertation research. I appreciate Greg Baxter, Nick Botto, and Irina Delusina at UC Davis for assistance on various instruments and sample preparation. I am very thankful for wonderful collaborations, scientific discussions, and laboratory training with Kate Davis, Oscar Branson, Jenn Fehrenbacher, Ed Chu, Anthony Menicucci, Ann Russell, and many others at UC Davis. Finally I would like to thank Reinhard Kozdon for his steadfast support and incredible edits and scientific discussions on two of my three dissertation projects.

On a more personal note, I am grateful for the support that I received from my family, friends, and mentors during my tenure as a graduate student at UC Davis. I could not have completed this dissertation without the support and guidance of those close to me. To my family: particularly my mom, dad, sister, brother, brother-in-law, and niece, I want to say thank you for listening to me talk about geology on family vacations, sitting through practice presentations, pretending to want to read my papers, and overall just always being there for support. To my mom particularly, thank you for always answering the phone to listen to me complain, and for discussing teaching pedagogy and strategies for hours on end. I hope to one day be the kind of teacher that you are. To all of my friends throughout the years at UC Davis, thank you for happy hours, outdoor adventures, pool parties, and team dinners. I especially want to thank Trevor Waldien, Jordan Carey, and Veronica Vriesman for fun times and steadfast support; it made a huge impact even if

that wasn't always clear at the time. Finally, my best friend and constant companion, Newton (Newt). From the first year of my PhD Newt has been a constant source of love and support and I owe so much to him.

I appreciate my committee members Jennifer Fehrenbacher, and David Gold for the knowledge and wisdom that they've shared with me over the past few years and stepping up to join my committee in the last stages of my degree. Lastly, to Tessa Hill, who stepped into the position of my primary advisor without hesitation and gave me the support I needed in order to finish this degree. I immensely appreciate your hard work, dedication, and collaboration, which have allowed me to grow freely into the scientist and person that I am today. I feel that your mentorship has given me the tools to become an excellent mentor myself, and I look forward to our future endeavors.

ABSTRACT

The Arctic Ocean is currently experiencing increases in temperature twice as fast as lower latitudes. Changes in air and surface water temperatures as well as fluctuations in rates and volume of deep-water formation in the North Atlantic will have substantial impacts on global climate. Therefore, understanding how the structure of the Arctic Ocean has changed in response to variations in past climate will help us to better predict what changes we can expect as the Earth warms over the next century. To do this, we rely on one of the fundamental tools used to reconstruct past ocean conditions- the geochemistry of foraminiferal calcite. *Neogloboquadrina pachyderma* is the species of planktonic foraminifera that dominates high latitude assemblages and is therefore the principal species utilized to study the paleoceanography of the polar regions. The calcification of *N. pachyderma* is unusual in that it grows its primary (lamellar) calcite in the surface waters and subsequently adds a thick $CaCO_3$ crust at depths below the mixed layer. Therefore, geochemical analyses on whole shells produce results that are difficult to interpret as they are derived from mixed lamellar and crust calcite contributions that are unequal in mass. Analytical tools capable of high spatial resolution such as electron microprobe, laser ablation ICPMS (LA-ICPMS) and secondary ion mass spectrometry (SIMS) can measure the geochemistry of discrete regions of *N. pachyderma* shells, therefore allowing us to analyze ontogenetic and crust calcite separately.

For the first portion of my dissertation, I analyze the *in situ* Mg/Ca and $\delta^{18}O$ in discrete calcite zones using LA-ICPMS, EPMA and SIMS within modern *N. pachyderma* shells from the highly dynamic Fram Strait and the seasonally isothermal/isohaline Irminger Sea. I compare shell geochemistry to the measured temperature, salinity and $\delta^{18}O_{sw}$ in which the shells calcified to better understand the controls on *N. pachyderma* geochemical heterogeneity. The results

include a new relationship between Mg/Ca and temperature in *N. pachyderma* lamellar calcite that is significantly different than published equations for shells that contained both crust and lamellar calcite. Further, this data revealed that the $\delta^{18}O$ of the crust and lamellar calcite of *N. pachyderma* from an isothermal/isohaline environment are indistinguishable from each other, indicating that shifts in *N. pachyderma* $\delta^{18}O$ are primarily controlled by changes in environmental temperature and/or salinity rather than differences in the sensitivities of the two calcite types to environmental conditions.

Next, I evaluate intrashell trace element (TE)/Ca data from *N.pachyderma* shells that were grown and subsequently produced a crust in culture at various temperatures. These shells reveal marked shifts in the Mg/Ca, Ba/Ca, Zn/Ca, Al/Ca, and Mn/Ca between the lamellar and crust calcites grown in culture with no associated changes in either the environmental conditions or trace element concentrations of the seawater. The TE/Ca data were compared to the hydrologic conditions (i.e. temperature, salinity, pH, [TE]), to better understand the relationships between the crust and lamellar geochemistry and the environment in which the shells calcified. My results demonstrate that the Mg/Ca in the LC agrees with the calibration relationship previously described in Livsey et al. (2020), while the study reveals that Mg/Ca in the crust calcite is not primarily controlled by temperature. Though these results cannot definitively resolve what is controlling the transition in geochemistry between the LC and crust, they do reveal that neither changes in the environmental conditions, $[Te]_{sw}$, nor a change in the calcification rate are the dominant factors.

Finally, I quantified patterns of freshwater outflow from the Arctic associated with the draining of glacial Lake Agassiz. This meltwater event at ~11.5 ka likely triggered a slowdown of global ocean currents and initiated the northern hemisphere cold interval known as the

Younger Dryas. I combine LA-ICPMS trace element measurements with $\delta^{18}O_{calcite}$ analyses on *N. pachyderma* shells to reconstruct the $\delta^{18}O$ of Lake Agassiz-derived Mackenzie River meltwater. Remarkably, these results indicate that the geochemistry of the meltwater entering the Arctic Ocean varies throughout the Younger Dryas event, revealing the inaccuracy of current model simulations. Further, I illustrate that the meltwater pulse was not continuous throughout the interval, with at least one cessation of drainage that is linked to a shift in the chemistry of the meltwater. Overall, the time-resolved isotopic evolution of meltwater in the Arctic Ocean through the Younger Dryas reveals the unexpected complexities of meltwater pulses, which have large implications for our understanding of volumes and rates of freshwater discharge into the North Atlantic in the past and provides insights on the source of the meltwater for the Younger Dryas event.

SUPPLEMENTARY MATERIALS

Chapter 1:

Data Set S1. Raw laser counts per second (CPS) for elements B^{11}, Mg^{24}, Mg^{25}, Al^{27}, Ca^{43}, Ca^{44}, Sr^{88} and Ba^{138} with Time (sec) through analysis for the Fram Strait Plankton tow samples. Each file is named by the sample_ID and contains between 1-3 ablation profiles with background between each.

Data Set S2. Raw laser counts per second (CPS) for elements B^{11}, Mg^{24}, Mg^{25}, Al^{27}, Ca^{43}, Ca^{44}, Sr^{88} and Ba^{138} Time (sec) through analysis for the Irminger Sea sediment trap samples. Each file is named by the sample_ID and contains between 1-3 ablation profiles with background between each.

Data Set S3. Contains .tiff and .eps files of EPMA scans of polished samples colored by relative Mg/Ca concentrations. There are no units on the color-scales as they are all relative concentrations of Mg/Ca within each scan. Accompanying .txt files are raw data for each scan with analytical settings and complete scan parameters.

Data Set S4. SEM photomicrographs of individual Fram Strait plankton tow shells at various stages of processing including cleaned shells mounted for LA-ICP-MS, shells mounted in epoxy and polished for SIMS, gold-coated shells post-SIMS analysis.

Data Set S5. SEM photomicrographs of individual Irminger Sea shells at various stages of processing including cleaned shells mounted for LA-ICP-MS, shells mounted in epoxy and polished for SIMS, gold-coated shells post-SIMS analysis.

Chapter 2:

Data Set 2 S1. Raw laser counts per second (CPS) for elements B^{11}, Mg^{24}, Mg^{25}, Al^{27}, Ca^{43}, Ca^{44}, Sr^{86}, Sr^{87}, Sr^{88} and Ba^{138} with Time (sec) through analysis for the cultured samples. Each file is named by the sample_ID and contains between 1-3 ablation profiles with background between each.

Data Set 2 S2. SEM photomicrographs of individual cultured foraminifera prior to LA-ICPMS analyses.

Chapter 3.

Data Set 3 S1. Raw laser counts per second (CPS) for elements B^{11}, Mg^{24}, Mg^{25}, Al^{27}, Ca^{43}, Ca^{44}, Sr^{88} and Ba^{138} Time (sec) through analysis for the AOS 94b-17. Each file is named by the sample_ID and contains between 1-3 ablation profiles with background between each.

Data Set 3 S2. SEM photomicrographs of individual foraminifera prior to LA-ICPMS analyses.

Ch. 1: High-resolution Mg/Ca and $\delta^{18}O$ patterns in modern *Neogloboquadrina pachyderma* from the Fram Strait and Irminger Sea

Caitlin M. Livsey[1], Reinhard Kozdon[2,6], Dorothea Bauch[3,4], Geert-Jan A. Brummer[5], Lukas Jonkers[6], Ian Orland[7,8], Tessa M. Hill[1], Howard J. Spero[1]

[1]*Department of Earth and Planetary Sciences, University of California Davis, Davis, CA 95616, USA.*

[2]*Department of Earth and Environmental Sciences and Lamont–Doherty Earth Observatory of Columbia University, 61 Route 9W, Palisades, NY 10964, USA.*

[3]*GEOMAR Hemholtz Centre for Ocean Research, Kiel, Germany.*

[4] *Leibniz Laboratory for Radiometric Dating and Stable Isotope Research, Kiel University, Kiel, Germany.*

[5]*NIOZ, Royal Netherlands Institute for Sea Research, Department of Ocean Systems, and Utrecht University, Texel, The Netherlands.*

[6]*MARUM, Universität Bremen, Leobenerstraße 8, Bremen, Germany.*

[7]*WiscSIMS, Department of Geoscience, University of Wisconsin, Madison, WI, 53706, USA.*

[8]*Wisconsin Geological and Natural History Survey, University of Wisconsin, Madison, WI 53705, USA*

This chapter was published in 2020 in *Paleoceanography and Paleoclimatology*

Abstract

Neogloboquadrina pachyderma is the dominant species of planktonic foraminifera found in polar waters and is therefore invaluable for paleoceanographic studies of the high latitudes. However, the geochemistry of this species is complicated due to the development of a thick calcite crust in its final growth stage and at greater depths within the water column. We analyzed the *in situ* Mg/Ca and $\delta^{18}O$ in discrete calcite zones using LA-ICP-MS, EPMA and SIMS within modern *N. pachyderma* shells from the highly dynamic Fram Strait and the seasonally isothermal/isohaline Irminger Sea. Here we compare shell geochemistry to the measured temperature, salinity and $\delta^{18}O_{sw}$ in which the shells calcified to better understand the controls on *N. pachyderma* geochemical heterogeneity. We present a relationship between Mg/Ca and temperature in *N. pachyderma* lamellar calcite that is significantly different than published equations for shells that contained both crust and lamellar calcite. We also document highly variable SIMS $\delta^{18}O$ results (up to a 3.3‰ range in single shells) on plankton tow samples which we hypothesize is due to the granular texture of shell walls. Finally, we document that the $\delta^{18}O$ of the crust and lamellar calcite of *N. pachyderma* from an isothermal/isohaline environment are indistinguishable from each other, indicating that shifts in *N. pachyderma* $\delta^{18}O$ are primarily controlled by changes in environmental temperature and/or salinity rather than differences in the sensitivities of the two calcite types to environmental conditions.

1 Introduction

Numerous paleoceanographic proxies have been developed that utilize the trace element and stable isotope compositions of the calcium carbonate shells of planktonic foraminifera (e.g.

Urey, 1948; Epstein et al., 1953; Emiliani, 1955, 1961; Nürnberg et al., 1996; Lea et al., 1999; Kucera, 2007; Ravelo and Hillaire-Marcel, 2007; Zeebe et al., 2008; Hönisch et al., 2011, 2013; Allen et al., 2012). Traditionally, geochemical analyses on planktonic foraminifera have pooled multiple shells and analyzed them together to obtain a single geochemical data point. However, studies on single foraminifera shells reveal that there is significant intra-shell geochemical heterogeneity in chamber walls that may be due to environmental, biological, or diagenetic factors (Duckworth, 1977; Wu and Hillaire-Marcel, 1994; Eggins et al., 2003, 2004; Kozdon et al., 2009; Fehrenbacher and Martin, 2010; Sadekov et al., 2010; Jonkers et al., 2012; Vetter et al., 2013a; Fehrenbacher et al., 2015, 2017; Spero et al., 2015). These micron-scale variations in chamber wall geochemistry can be measured in foraminifera using different methods, including laser ablation-inductively coupled plasma-mass spectrometry (LA-ICP-MS) for trace elements and secondary ion mass spectrometry (SIMS) for stable isotopes such as $\delta^{18}O$. Combining trace element and $\delta^{18}O$ values from discrete domains of calcite within individual foraminifera has the potential to provide linked paleoceanographic information from exceptionally small samples (e.g., Vetter et al., 2017). The combination of such high-resolution analyses on distinct domains of calcite from specific depths potentially greatly expands our capacity to reconstruct past water column hydrography on a scale that was not previously possible.

Neogloboquadrina pachyderma (sinistral-coiling) is the only polar species of planktonic foraminifera and dominates high latitude assemblages (Bauch et al., 1997), and is therefore the primary species used to study the paleoceanography of polar regions. The exact depth habitat of *N. pachyderma* varies greatly by location and is likely controlled by the vertical temperature and chlorophyll concentration gradients (e.g. Jonkers and Kucera, 2015; Greco et al., 2019). For most of its ontogeny, *N. pachyderma* dwells near the surface where it secretes chambers composed of

$CaCO_3$ that is commonly referred to as lamellar calcite (LC) (Reiss, 1957; Erez, 2003). Prior to the completion of its life cycle, *N. pachyderma* sinks through the mixed layer/upper pycnocline and it adds a thick $CaCO_3$ crust that envelops the finer-grained LC (Arikawa, 1983; Carstens et al., 1992; Kohfeld et al., 1996, Simstich et al. 2003). Assuming that the geochemistries of these two calcite domains reflect the chemistry of the water in which they were precipitated, single shell chamber walls could record hydrographic information from both the near surface and the deeper pycnocline (Kozdon et al., 2009; Vetter et al., 2013b). Because shell [Mg] varies predominantly with temperature (Nürnberg, 1995; Lea et al., 1999), and shell $\delta^{18}O$ is modified by temperature and $\delta^{18}O_{seawater}$ ($\delta^{18}O_{sw}$; which varies with salinity and local hydrology), populations of individually analyzed *N. pachyderma* shells hold the potential to reconstruct temperature and salinity/$\delta^{18}O_{sw}$ with depth in the polar oceans.

However, while high resolution geochemical analysis on *N. pachyderma* has the potential to revolutionize high latitude paleoceanography, there are a number of outstanding questions that need to be addressed. First, the presence of calcite grown at different depths complicates precise interpretation of *N. pachyderma* whole shell geochemical analyses, as the ratio of crust to LC differs between individuals (Arikawa, 1983; Kohfeld et al., 1996; Stangeew, 2001; Kozdon et al., 2009, Simstich et al., 2003). Furthermore, the relationship between the geochemistry of the shell and the hydrologic conditions in which the crust and the LC precipitates, respectively, may be different (Kozdon et al., 2009; Jonkers et al., 2010; Bolton and Marr, 2013; Davis et al., 2017). Consequently, the relationships between water temperature and shell Mg/Ca and $\delta^{18}O_{calcite}$ need to be evaluated separately for *N. pachyderma* lamellar and crust calcite in order to accurately interpret geochemical data from individual shell analyses.

Here we address these outstanding questions on modern *N. pachyderma* from the Fram Strait and the Irminger Sea. The Fram Strait is the only deep-water connection between the Arctic and North Atlantic Oceans, and therefore is the channel through which the majority of Arctic water exchange occurs (Zweng et al., 2018), contributing to the formation of North Atlantic Deep Water (NADW; Bryan, 1986). At sub surface depths of 50-200 m (Cokelet et al., 2008), warm/salty Atlantic water enters the Arctic via the West Spitsbergen Current (>2°C, >35 psu), while cold and low salinity surface water leaves the Arctic via the East Greenland Current (0-2°C, 33-34.4 psu; Consolaro et al., 2018). The movement of diverse water masses through the Fram Strait results in significant temperature and salinity gradients within and across the channel. Therefore, the Fram Strait is an ideal location to explore potential relationships between the geochemistry of *N. pachyderma* and the hydrological conditions in which the calcite was precipitated. For comparison with the Fram Strait samples, we have also analyzed *N. pachyderma* shells collected from the Irminger Sea that calcified in an isothermal and isohaline water column to evaluate the non-environmental controls influencing the geochemistry of the two calcite domains in a shell. Starting in January, convective mixing to >400 m depth in the central Irminger Sea produces a vertical gradient of <0.5 ºC and <0.3 psu (de Jong et al., 2010). Because the crust and lamellar calcite for these shells grew under identical hydrologic conditions, neither geochemical variability within the shell or systematic differences between the two domains can be attributed to temperature, salinity or $\delta^{18}O_{sw}$ changes.

In this study, we report results of *in situ* analyses of the geochemistry of *N. pachyderma* lamellar and crust calcite Mg/Ca using LA-ICP-MS and electron probe microanalysis (EPMA), as well as $\delta^{18}O_{calcite}$ data measured using SIMS. In addition, we conducted whole shell $\delta^{18}O_{calcite}$ analyses using standard isotope ratio mass spectrometry (IRMS) on single or pooled shells from

both study sites. Hydrographic measurements (i.e. temperature, salinity, $\delta^{18}O$) of the water in which the samples were collected are utilized to better understand the relationships between the geochemistry of the crust and lamellar domains of *N. pachyderma* and the environmental conditions during foraminiferal growth.

2 Materials and Methods

2.1 Sample Collection

Fram Strait

Living planktonic foraminifera were collected in the Fram Strait using a vertical Hydrobios multinet tow with a 63 μm mesh from the Polarstern ARK XV/2 cruise during the summer of 1999. At each of the eight stations (Figure 1a), tows were taken from 0-50, 50-100, 100-200, 200-300 and 300-500 m depths. Onboard sample treatment and initial foraminifera picking methods were previously described by Stangeew (2001) and consisted of conserving the plankton tow collected samples in 90% denatured ethanol and storage at 4°C. Samples used in this study were *N. pachyderma* that were living at the time of capture as indicated by Rose-Bengal staining. Following the cruise, stained foraminifera were picked from the >63 μm tow samples, rinsed in distilled water, dried at room temperature, and transferred to micropaleontology slides (complete sample list and station information can be found in Table S1). Water samples were collected at each of the stations using a CTD rosette at 0, 25, 50, 100, 200, 300, 400 and 500 m depths while temperature and salinity measurements were recorded every 10 m (Figure 1b). The water samples were later analyzed for $\delta^{18}O_{sw}$, $\delta^{13}C_{DIC}$, and nutrient concentrations (Stangeew, 2001).

Irminger Sea

Details of the sediment trap design and deployment information in the Irminger Sea are described in Jonkers et al. (2010). These sediment traps (~2750 m depth) were sampled every 16 days and all samples used in this study were collected during the month of April (2006 or 2007) when the water column displayed isothermal/isohaline characteristics (Jonkers et al., 2010). Before the collection bottles were deployed in the traps, they were filled with ambient seawater, poisoned with $HgCl_2$, and buffered with Borax. Upon recovery, the bottles were kept at 4°C until samples could be processed and stored dry. Eight shells from trap IRM-3 (sample A-14) and twelve shells from trap IRM-4 (sample A-15) were picked from the dried 150-250 μm size fraction for subsequent analyses.

2.2 Sample preparation

For LA-ICP-MS and SIMS analyses, individual *N. pachyderma* were picked, cracked into multiple fragments using a scalpel, and cleaned to remove remnant organics using an oxidative 1:1 solution of 35% H_2O_2:0.1N NaOH in conjunction with 8 rinses in methanol, and 3 rounds of 30 seconds in methanol while in an ultrasonic bath (Mashiotta et al., 1999). Between each rinsing step, the methanol is aspirated using a pipette. This cleaning procedure is sufficiently rigorous to remove organic contamination, while avoiding physical breakage of the shells or dissolution of the fragile calcite layers. After cleaning, *N. pachyderma* fragments (>50 μm surface area) were mounted on carbon tape and imaged in variable pressure mode using a Hitachi TM300 scanning electron microscope (SEM) in the UC Davis Department of Earth and Planetary Sciences. The resultant images were reviewed to assess shell microstructure and to note the orientation of the shells for subsequent analyses. Figure 2 illustrates shells from the Irminger Sea (a-d) and Fram Strait (e-h) foraminifera shells at various stages of processing and sample preparation.

2.3 LA-ICP-MS analyses and data processing

Typically two LA-ICP-MS spots from 40 uncrusted shells mounted on carbon tape from the Fram Strait plankton tows (n=84 spots) and 20 crusted shells from the Irminger Sea sediment traps (n=48 spots) were obtained to quantify domain-specific metal/Ca profiles through shell walls. The resulting data come from shells that were collected in the 0-50, 50-100, and 100-200 m depth tows at each of the eight stations across the Fram Strait and from the IRM-4 and IRM-3 sediment trap samples. *N. pachyderma* fragments were analyzed for Me/Ca trace elements (^{11}B, ^{24}Mg, ^{25}Mg, ^{27}Al, ^{43}Ca, ^{44}Ca, ^{55}Mn, and ^{56}Ba) by ablating from the interior of the shell wall to the exterior using a Photon Machines pulsed 193 nm ArF UV excimer laser with a HelEx dual-volume sample chamber attached to an Agilent 7700x Quadrupole ICP-MS at the UC Davis Stable Isotope Laboratory in the Department of Earth and Planetary Sciences. Square 40x40 μm spots were ablated using a repetition rate of 5 Hz and a fluence of 0.87 J/cm^2 to generate replicate profiles from each shell, while acquiring enough material to measure multiple elements simultaneously. LA-ICP-MS spot locations were chosen preferentially on areas of the F or F-1 chambers that were oriented perpendicular to the laser beam. Complete analytical settings are summarized in Table 1.

The data collected by the LA-ICP-MS system was reduced using the LAtools software package (specific settings shown in Table 1; Branson et al., 2019). Data reduction included removal of abnormal spikes/noise from ablation profiles, identifying and excluding the background counts, and applying a background correction to the data calculated using a 1D interpolation. Sensitivity drift was accounted for using counts on NIST glass standards 610, 612, and 614 during each analytical session, which were used to generate and subsequently apply a time-sensitive calibration calculation and standardization to absolute concentration in LAtools. Elemental counts were normalized to ^{43}Ca counts, and contaminated domains were filtered out

using Mn/Ca or Al/Ca concentrations above 0.5 mmol mol^{-1} (Pena et al., 2008). For each LA-ICP-MS spot, Mg/Ca profiles through the shell wall (inside to the outside) are plotted against ablation time (seconds) to reveal the internal pattern of Mg/Ca variability (all laser profiles raw pre-processed laser data, and the LAtools minimal export files can be found in the Supplementary Materials).

2.4 Oxygen isotope analyses

LA-ICP-MS ablated fragments were removed from the carbon tape using ethanol and mounted for $\delta^{18}O_{calcite}$ analyses with a CAMECA IMS 1280 SIMS at the WiscSIMS Laboratory, University of Wisconsin, Madison. Fragments were arranged based on size and placed within 5 mm of the center of a 1-inch diameter circular mold along with two grains of the WiscSIMS calcite standard UWC-3 ($\delta^{18}O$ = +12.49 ‰ VSMOW or -17.17 ‰ VPDB; Kozdon et al., 2009). Samples were cast in Buehler EpoxiCure resin under vacuum, and subsequently polished to expose cross-sections of the shell walls close to regions that were analyzed by LA-ICP-MS. Images of the polished shells were generated with SEM BSE to qualitatively determine the thickness of exposed shell walls and cross section geometry prior to analysis (see Figure 2c,g and all remaining SEMs in Supplementary Materials). Immediately before analysis, the epoxy mounts were cleaned with ethanol and DI-water, dried in a vacuum oven, and gold coated. Between 1-7 spots within the lamellar calcite of each shell was analyzed for $\delta^{18}O$ using a 3-µm-diameter $^{133}Cs^{+}$ beam with analytical settings and conditions similar to those described in Kozdon et al., (2009). After every ~10th SIMS spot analysis, UWC-3 calcite standard was measured four times to bracket the samples to correct for instrumental mass fractionation. No additional correction was made for instrumental drift.

Reproducibility of the individual spot analyses of UWC-3 standard (bracketing samples) is assigned as precision (reproducibility) of unknown samples. Average precision for all 19 brackets of 3-micron spots is ±0.77‰ (2SD); reproducibility (2SD) of UWC-3 in individual brackets varied from 0.37 to 1.43‰ with only three brackets >1.0‰ (Table S2). The bracketing standards, and sample $\delta^{18}O$ data were finally corrected and converted from VSMOW to VPDB using the conversion of Coplen et al. (1983). All subsequent ‰ values presented are reported on the VPDB scale. After SIMS analysis, the sample mounts were imaged by SEM BSE and all SIMS spots were screened post-analysis to ensure that only calcite was measured and to exclude data from "irregular pits" (Cavosie et al., 2005; Linzmeier et al., 2016). Furthermore, the secondary ion yield and background corrected $^{16}OH/^{16}O$ ratios reported relative to bracketing standards from all analyses were examined to identify any anomalous data that should be removed (Wycech et al., 2018). Anomalous results were removed and are not included in any data tables or supplementary materials.

Additional Fram Strait plankton tow shells were oxidatively cleaned, roasted at 375°C *in vacuo* for 35 minutes to remove remnant carbon tape, and then run on an Optima isotope ratio mass spectrometer (IRMS) in the Stable Isotope Lab at UC Davis. In order to obtain masses large enough to be analyzed on the IRMS (8-15 μg), 3-6 individual foraminifera from the same sample were combined and run together. Due to shortage of specimens in some Fram Strait tow depth samples, some samples contain a mix of individuals from adjacent collection depths at the same site to obtain sufficient mass for IRMS analyses. This information is described for each sample in Table 2.

2.5 Electron microprobe analyses

In preparation for analysis on the electron microprobe, SIMS sample mounts containing the Fram Strait samples were gently repolished to remove the gold coat and then recoated with carbon. Mg and Ca elemental maps were generated on the mounted samples with a Cameca SX-100 electron microprobe in the UC Davis Department of Earth and Planetary Sciences. Elemental maps were produced using 15 keV voltage, 15 nA beam current, a 1 μm spot size rasterized over the area of each shell, and a dwell time of 1 second. Mg and Ca counts were collected concurrently, and resultant Mg/Ca (counts/counts) maps were generated in RStudio. Each shell fragment was analyzed, mapped, and then colored using the RStudio color palette "topo.colors". For all mounts, spots with Ca counts below 1000 could not be distinguished from background and were therefore masked. All EPMA maps (Figure 3 and Supplementary Materials) are shown at a 1 pixel/μm resolution with each color scale specific to that respective shell. EPMA counts were not converted to mmol/mol since no internal standardization was done at the time of analysis, and all shells were previously analyzed via LA-ICP-MS, so further quantification was not needed.

3 Results

3.1 Fram Strait lamellar Mg/Ca

All LA-ICP-MS profiles from 40 individual shells from the Fram Strait were combined to determine the lamellar calcite Mg/Ca to temperature relationship. The total range of mean shell lamellar Mg/Ca among the shells is 0.58 to 4.77 (+/- 1.28 2SE) mmol/mol. In addition to large inter-shell variability, the Mg/Ca ratios within single shells (individual profiles through shells) also vary significantly, with intra-shell ranges between 3 and 4 mmol/mol. The inter-spot variability between Mg/Ca profiles within single shells is smaller, with 2SD ranging from 0-2.08

mmol/mol with an average of 1.07 mmol/mol (Table S3). Intra-shell values from here on will refer to the Mg/Ca values through shell walls.

The mean shell Mg/Ca ratios are compared to the average CTD measured temperatures at the water depths from which the samples were collected, which include 21 different water temperatures ranging from -1.81 to 3.80°C (Figure 4, Table S3). While it is possible that shells were advected to the sample location, it is unlikey that any of the individual foraminifera originated from a completely different water mass, and therefore the CTD measured temperatures are interpreted to reflect the conditions in which the shells grew. Figure 4 shows the relationship between average LA-ICP-MS Mg/Ca data from individual shell LC and the ambient temperatures recorded at the plankton tow collection depths assuming *in situ* calcification. From these data, we obtain the exponential relationship (pre-exponential and exponential statistics are $\pm 2\sigma$ standard error):

$$\text{Mg/Ca (mmol/mol)} = 1.95(\pm 0.08) * e^{(0.082(\pm 0.03)*T)} \quad (1)$$

Though a linear model was comparable to the exponential fit, we follow established protocol and adhere to the law of thermodynamics to apply an exponential relationship. The precision of temperature reconstructions ($\pm 2\sigma$) is calculated by inputting the range of measured Mg/Ca into Eq 1 using the upper and lower 95% confidence constraints on the coefficients. The resulting precision using this relationship for the calibrated temperature range is ±0.44 ºC.

Overall, the samples from the Fram Strait plankton tows appeared to lack an outer crust layer, and therefore we interpret that shell wall geochemical analyses were only conducted on lamellar calcite. The presence of low Mg/Ca ratios (1-2 mmol/mol) on the outer portions of some shell walls indicate that some of the shells may display early crusting (Figure 3). These low Mg/Ca domains are evident in both the LA-ICP-MS profiles and the microprobe Mg/Ca maps

and vary in thickness both between chambers and individuals (ex. specimens PT1a and PT20a). The presence of alternating high and low Mg/Ca bands is apparent in the tow-collected shells, with thicker shells revealing a larger number of bands. Broadly, shells display a trend from higher Mg/Ca in the lamellar calcite of the inner shell walls to lower Mg/Ca towards the outer surfaces, with at least one prominent low-Mg/Ca band closer to the inside edge of the shell (Figure 3).

3.2 Mg/Ca and $\delta^{18}O$ from Irminger Sea lamellar and crust calcite

Because the fully crusted *N. pachyderma* samples obtained from the Irminger Sea very likely grew in a well-mixed water column that lacked temperature or salinity variation, the shell geochemistry should not have been affected by variations in these parameters. Individual shells exhibit inter- and intra-shell Mg/Ca variations, with an average range of 0.35 mmol/mol within single ablation profiles (Table S4), which is markedly less variable relative to the Fram Strait samples. Inter-spot variability in these shells was very low as well with an average range of 0.30 mmol/mol (Table S4). The patterns within the laser profiles indicate lower Mg/Ca in the crust calcite of the individual shells supporting the microprobe results of Jonkers et al. (2016), although the crust and LC Mg/Ca differ by <0.5 mmol/mol (Figure 5a and Supplementary Materials). For all the samples, Mg/Ca profiles through the lamellar and crust calcites of Irminger Sea shells reveal a total range of mean Mg/Ca of 0.70 to 1.95 mmol/mol. Overall, the Irminger Sea Mg/Ca results support the observations that Mg incorporation into *N. pachyderma* calcite differs between the crust and lamellar calcites (Hendry et al., 2009; Jonkers et al., 2013; Steinhardt et al., 2015; Davis et al., 2017), but the difference is small, and the lower variability and general agreement of Mg/Ca at a population-scale indicates that temperature is the dominant control over *N. pachyderma* Mg/Ca.

To assess how $\delta^{18}O_{calcite}$ varies between the lamellar and crust calcite in the Irminger Sea samples, 79 SIMS spots were analyzed on 16 of the shells targeted by LA-ICP-MS in the preceding paragraph (Figure 5b). Thirty-six SIMS spots were located within the lamellar calcite region of the shells while the remaining analyses were located within the crust calcite (see SEM images in the Supplementary Materials). The difference between the average measured $\delta^{18}O_{calcite}$ on the crust vs. LC is 0.18 ‰, and a paired t-test reveals that the crust and LC $\delta^{18}O_{calcite}$ values are statistically similar ($p<0.05$), demonstrating that a single temperature vs $\delta^{18}O_{calcite}$ relationship can be used to interpret shell $\delta^{18}O$ geochemistry. Mean spot-to-spot precision (2SD) for these data is +/-0.72‰ for all analyses (Tables S2, S5). Notably, the previously reported IRMS $\delta^{18}O_{calcite}$ values for shells from the same sediment trap samples were 2.31‰ for IRM-3 A-14 and 2.52‰ for IRM-4 A-15 (Figure 5b; Jonkers et al., 2010) suggesting *N. pachyderma* displays an IRMS-SIMS $\delta^{18}O$ offset of ~0.7‰ similar to that previously documented in other planktonic foraminifera species (Wycech et al., 2018b).

3.3 SIMS and IRMS $\delta^{18}O$ from Fram Strait lamellar calcite

For the Fram Strait plankton tow samples, 75 SIMS $\delta^{18}O$ spots were analyzed from the 25 thickest shells (Figure 6, Tables S2, S6). Depending on the surface area of exposed shell wall, individuals were analyzed 1-7 times using a ~3 µm spot diameter. The average $\delta^{18}O$ of the LC for each individual foraminifera was 1.5‰, with the largest $\Delta^{18}O$ range within a single shell of 3.3‰ (Table S6). The average analytical precision for each SIMS analysis was 0.64‰ (2SD) which is considerably lower than the intra-shell $\Delta^{18}O_{calcite}$ range, indicating that the intra-shell range exceeds analytical precision by a factor of 2.5-5. All raw data collected on the SIMS are presented in Table S2. SIMS $\Delta^{18}O_{calcite}$ data are plotted on EPMA Mg/Ca maps with adjacent LA-ICP-MS Mg/Ca profiles in Figure 3. The SEM images in the first column of Figure 3

identify the SIMS pits location on the microprobe maps. The intra-shell $\delta^{18}O$ variability does not correlate with chamber number or distance along the shell wall, indicating that the $\delta^{18}O_{calcite}$ variability is not easily explained by ontogeny (Figure 3). Across the 25 *N. pachyderma* shells analyzed by SIMS, the $\delta^{18}O_{calcite}$ values of individual shells range from -2.7 to +2.4‰, with average shell values between -1.3 and 1.8‰ (Figure 6; Table S6). Compared to the spot-to-spot precision (2SD) the geochemical variability between shells cannot be explained by analytical uncertainty alone.

IRMS analyses conducted on pooled Fram Strait *N. pachyderma* shells yield $\delta^{18}O_{calcite}$ values that are offset from the SIMS $\delta^{18}O_{calcite}$ data collected from the same group of shells (Table 2; Figure 6). The IRMS $\delta^{18}O_{calcite}$ values are 1.84 to 3.44‰ higher than the average SIMS $\delta^{18}O_{calcite}$ in the tows. Figure 6 shows the Fram Strait SIMS and IRMS data plotted with predicted calcite $\delta^{18}O$ values from Kim and O'Neil (1997) based on measured temperature, $\delta^{18}O_{sw}$, and salinity at each site. The SIMS $\delta^{18}O$ spots exclusively show more negative $\delta^{18}O$ compared to both predicted and IRMS-derived $\delta^{18}O$, and do not appear to show any consistent patterns with depth at each station. The IRMS $\delta^{18}O$ results agree well with predicted $\delta^{18}O$ at the same depth, with an average offset of 0.32 ± 0.79‰. Furthermore, the samples that show the largest spread in IRMS $\delta^{18}O$ values coincide with a region of the water column where the hydrology and therefore the predicted $\delta^{18}O$ are complicated.

3.4 Evaluation of calcite microstructure

SEM micrographs of the shells from the Fram Strait plankton tows and the Irminger Sea sediment traps reveal distinct calcite fabrics between the two set of samples (Figure 2). A comparison between crusted and non-crusted *N. pachyderma* shells from the Irminger Sea and the Fram Strait respectively are shown in Figure 2 as whole shells (a,e), cracked fragments (b,f),

and polished cross-sections (c-d,g-h). The bottom SEM micrographs show cross-sections of the two shells, in which the Irminger Sea shell displays a smoother, denser, more homogenous and compact calcite surface compared to the shell from the Fram Strait. Figure 3 also contains photomicrographs of cross-sectioned shells from the Fram Strait revealing irregular surfaces, apparent enhanced porosity, and overall rough or mottled textures.

4 Discussion

4.1. Mg/Ca patterns in *N. pachyderma*

Lamellar calcite (LC) in the Fram Strait plankton tow *N. pachyderma* examined here display distinctive patterns within single shells and between shells. Both LA-ICP-MS and microprobe results reveal that LC shells contain multiple high/low Mg bands with lower Mg/Ca ratios towards the outside surfaces of some of the chambers (Figure 3). These patterns are consistent with Mg/Ca profiles reported from the shell walls in other non-symbiont bearing planktonic foraminifera such as *Globorotalia inflata, G. scitula*, *G. tumida, G. menardii, G. truncatulinoides, Neogloboquadrina incompta,* and *Pulleniatina obliquiloculata* (Hathorne et al., 2003, 2009; Sadekov et al., 2005; Kunioka et al., 2006; Steinhardt et al. 2015; Davis et al., 2017). While the microprobe maps highlight subtle differences in Mg/Ca patterns between chambers in the Fram Strait samples, the LA-ICP-MS results demonstrate that when the closely-spaced Mg bands are averaged, *N. pachyderma* lamellar calcite Mg/Ca is relatively constant between different spots in individual shells (Table S3). This result indicates that while there are still controls on *N. pachyderma* Mg/Ca, the mean LC Mg/Ca of a population of shells can be used to estimate environmental temperature (Figure 4; Eq 1).

The Mg/Ca ratios in crusted single *N. pachyderma* shells from the Irminger Sea ranged between 0.70 to 1.95 (+/-0.54 2SD) mmol/mol with the lowest Mg/Ca in the outer crust region of

the shell walls. These data agree with the EPMA-generated Mg maps on samples from the same sediment traps (Jonkers et al., 2016). Although these *N. pachyderma* shells calcified in an isothermal water column in the Irminger Sea, they exhibit distinctly zoned Mg/Ca ratios (Figure 5a), supporting the conclusions of others (Jonkers et al. 2016; Davis et al., 2017) that Mg/Ca banding and crust/lamellar calcite Mg content in *N. pachyderma* is controlled by foraminifera physiology and is a part of the chamber formation process. The exact mechanism controlling the Mg concentration within *N. pachyderma* (and other species) is not fully understood and requires further investigation. Homogeneous low Mg/Ca calcite was also reported for *Neogloboquadrina incompta* crust relative to LC from NE Pacific specimens grown in the laboratory (Davis et al., 2017). Although a thick crust was not observed in the plankton tow specimens we analyzed from the Fram Strait, a few *N. pachyderma* shells (see PT1a and PT20a in Figure 3) display considerably reduced Mg/Ca ratios in the outer surfaces of some chamber walls which may represent early crust calcite precipitation in these upper water column-collected specimens.

A number of Mg/Ca vs temperature calibrations have been published for *N. pachyderma* from core top and sediment trap samples (Table 3). Although these relationships were generated using whole *N. pachyderma* shells that contained both lamellar and crust calcite, the mass of calcite analyzed was dominated by the low Mg crusts. *N. pachyderma* crust is estimated to range between 50-80% of the total test mass, therefore making a correction based on the relative proportion of LC to crust difficult (Arikawa, 1983; Kohfeld et al., 1996; Stangeew, 2001; Kozdon et al., 2009). Despite averaging high and low Mg bands for each specimen, the Mg/Ca vs. temperature sensitivity of our Fram Strait LC relationship (Eq 1), 7.5% per °C, is similar to published calibrations for whole shells (Figure 7a). However, the pre-exponential constant is

considerably larger because of the lack of low-Mg crusts in these samples (Figure 7a) resulting in Eq 1 plotting well above other published calibrations for this species.

Since Eq 1 was calculated at low temperatures (-1.81 to 3.80°C), the precision on the relationship is below the precision of the instruments and therefore it is necessary to combine our data with similar data from warmer temperatures. Davis et al., (2017) conducted temperature experiments on living *N. pachyderma* collected in the NE Pacific off the coast of California and presented a Mg/Ca vs temperature calibration for *N. pachyderma* lamellar calcite between 6-12ºC (n = 10 shells). Figure 7b compares the Davis et al., (2017) Mg/Ca data with the average shell Mg/Ca from our Fram Strait plankton tow data and Eq 1. We cannot explain why the 6ºC data point (n = 4 shells) from Davis et al., (2017) falls below the LC dataset but note that this sample's ratio agrees with the Mg/Ca of whole *N. pachyderma* shells which contain both crust and lamellar calcite. Because crusting has been proposed to initiate at temperatures below 8-10 ºC in non-spinose foraminifera (Hemleben et al, 1985), we speculate that one or more of the 4 cultured shells analyzed in this sample contained crust calcite which would have reduced the Mg/Ca ratio of the entire sample. If we omit the 6 ºC data point from the combined data set, we obtain:

$$\text{Mg/Ca (mmol/mol)} = 1.93(\pm 0.04) * e^{(0.086(\pm 0.13)*T)} \quad (2)$$

which is nearly indistinguishable from Eq 1. This combined equation has a precision ($\pm 2\sigma$) of ±1.97 ºC at the typically cooler temperatures in the Arctic Ocean.

This suggests that we can potentially use this equation to calculate the temperature of the waters in which the foraminifera were living in from the measurements of the Mg/Ca ratios of *N. pachyderma* lamellar calcite. The consistency between our *N. pachyderma* LC-only Mg/Ca vs. temperature relationship and those for other species of planktonic foraminifera indicate that

while whole shell Mg/Ca vs. temperature reconstructions are not applicable for this species, we can now utilize *N. pachyderma* LC to refine high-latitude paleotemperature records. However, the large spread in Mg/Ca values and the inconsistent patterns within shell walls, it is likely that a larger sample size may be necessary to detect minor changes in temperature. That said, our results suggest that if the crust Mg/Ca vs. temperature relationship can be determined, *N. pachyderma* lamellar and crust calcite can be used to independently compute water column temperature profiles during different phases of shell formation.

4.2. Irminger Sea sediment trap *N. pachyderma* $\delta^{18}O$

Lamellar and crust calcite from single *N. pachyderma* shells from the isothermal and isohaline Irminger Sea yield overlapping SIMS $\delta^{18}O$ values that are indistinguishable from each other (Figure 5b). The distribution of the $\delta^{18}O_{calcite}$ values in these shells indicates that the $^{18}O/^{16}O$ ratio of crust and LC are affected equally by equilibrium fractionation offsets due to vital effects, carbonate ion effects, temperature and $\delta^{18}O_{sw}$ (Pearson, 2012). This result supports the use of a single relationship to reconstruct water column temperature and salinity from intra-shell $\delta^{18}O_{calcite}$ variability in the fossil record (Kozdon et al., 2009), and indicate that the mechanism responsible for the observable shift in Mg/Ca between the LC and the crust does not similarly affect the $\delta^{18}O$. Furthermore, these results support the conclusions of Kozdon et al. (2009) that the distinct crust and lamellar calcite $\delta^{18}O$ values observed in fossil *N. pachyderma* are likely due to calcification in different regions of the water column with different temperature/$\delta^{18}O_{sw}$ properties rather than a change in fractionation with crust formation. Finally, we suggest that the reason different species-specific paleotemperature equations have been proposed for whole shell *N. pachyderma* data is due to the mixing of LC and crust calcite phases that precipitated in water with different temperature and salinity conditions (Duplessy et al., 1981; Kohfeld et al., 1996).

Averaged SIMS measurements of shell $\delta^{18}O_{calcite}$ were significantly lower than previously published measurements on these samples using an IRMS ($\Delta\delta^{18}O_{SIMS\text{-}IRMS}$ = -0.7 ±1.18‰; Jonkers et al., 2010). A comparable $\Delta\delta^{18}O_{SIMS\text{-}IRMS}$ offset to that observed in these *N. pachyderma* data was reported in a study of another planktonic foraminifera, *Orbulina universa*. Wycech et al. (2018) reported an offset of -0.9‰ between SIMS and IRMS $\delta^{18}O_{calcite}$ values based on analyses of chamber wall fragments from multiple shells. The similarity in the $\Delta\delta^{18}O_{SIMS\text{-}IRMS}$ offsets suggests the magnitude of the offset is broadly applicable to SIMS analyses on modern foraminifera shells, and this type of careful species-specific test will improve comparisons of SIMS and IRMS data in future analyses. Potential factors contributing to this $\Delta\delta^{18}O_{SIMS\text{-}IRMS}$ offset are thoroughly explored in Wycech et al., 2018 and references therein.

4.3 Fram Strait plankton tow *N. pachyderma* $\delta^{18}O_{calcite}$

IRMS $\delta^{18}O_{calcite}$ data from pooled tow-collected *N. pachyderma* are evaluated across the Fram Strait using the temperature, salinity and $\delta^{18}O_{seawater}$ measurements made at each station (Table 2; Stangeew, 2001). Figure 6 presents a compilation of the measured $\delta^{18}O_{calcite}$ results for each of the eight stations across the Fram Strait shown with the corresponding temperature and salinity profiles for the upper 200 m of the water column. Predicted $\delta^{18}O_{calcite}$ values for *N. pachyderma* were generated using temperature and measured or salinity-calculated $\delta^{18}O_{seawater}$ with the relationship of Kim and O'Neil (1997). Predicted $\delta^{18}O_{calcite}$ for the six eastern stations (Stations 77-82; Figure 6a-f), utilize measured $\delta^{18}O_{seawater}$ values rather than salinity based $\delta^{18}O_{seawater}$ values because sea ice melt had a significant influence on $\delta^{18}O_{water}$ and salinity at these stations (Stangeew, 2001). Figure 6 includes previously published IRMS-generated $\delta^{18}O_{calcite}$ data from the same *N. pachyderma* tow material analyzed shortly after the cruise

(Stangeew, 2001; Table 2, Figure 6). The IRMS data from Stangeew (2001) are indistinguishable from the IRMS results obtained in this study and the $\delta^{18}O$ data are in good agreement with predicted $\delta^{18}O_{calcite}$ at each station. We observe an average $\Delta\delta^{18}O_{measured\text{-}predicted}$ offset of 0.38 ±0.5‰ for the IRMS data ($\Delta\delta^{18}O$ offset range of 0.02 to 1.03‰). These data demonstrate that *N. pachyderma* lamellar calcite $\delta^{18}O$ does not deviate significantly from predicted $\delta^{18}O_{calcite}$ and confirms our assumption that these tow-collected *N. pachyderma* are recording ambient conditions at each collection site.

Intra-shell and inter-chamber $\delta^{18}O_{calcite}$ was assessed in the lamellar calcite using SIMS (Figures 3, 6). These data reveal significant LC wall $\delta^{18}O_{calcite}$ variations and a clear $\delta^{18}O_{calcite}$ offset compared to the IRMS data. Figure 6 shows that the SIMS $\delta^{18}O_{calcite}$ measurements display an average LC offset of -2.91(±1.9) ‰ from the predicted $\delta^{18}O_{calcite}$ values. This offset and shell wall variability does not correlate with Mg/Ca banding or growth layers (Figure 3) and is not consistent across shells. There is no straight-forward explanation for these data. Kozdon et al. (2009) presented a similar range of SIMS $\delta^{18}O_{calcite}$ data from *N. pachyderma* lamellar calcite in plankton tow collected shells from the Eastern Nordic Seas that show a progressive $\delta^{18}O_{calcite}$ increase towards the lamellar-crust boundary. In their study, average $\delta^{18}O_{calcite}$ was ~3 ‰ higher in the crust relative to the LC. The inter-chamber $\delta^{18}O_{calcite}$ variation in the shells walls of Fram Strait *N. pachyderma* does not appear to correlate with distance from inside of the shell, but rather varies randomly within shells.

SIMS $\delta^{18}O_{calcite}$ data have been collected from the shell walls of other species of planktonic foraminifera using 10 µm spots, which has an analysis area 11x greater than the 3 µm spot used here (Kozdon et al., 2011, 2013; Vetter et al., 2013b; Wycech et al., 2018a, 2018b). These studies show intra-shell variation of < 1‰, with variations exceeding this level explained

by diagenesis or gametogenic calcification. Although increased measurement variance is expected with a smaller SIMS spot size, we did not observe this in 3-µm-spot SIMS analyses of LC and calcite crust on the Irminger Sea *N. pachyderma* shells. Rather, crusted *N. pachyderma* shells from the Irminger Sea display $\delta^{18}O$ variance similar to that reported in other studies (i.e. Kozdon et al., 2009; Valley and Kita, 2009; Vetter et al., 2013b), with an offset of 0.7‰ from IRMS data that was previously reported in other species (Figure 5b; Wycech et al., 2018b). Hence, the variation of SIMS $\delta^{18}O_{calcite}$ in Fram Strait samples and the large $\delta^{18}O$ offset from the IRMS measurements on the same material is not likely due to SIMS spot size. Post-processing of the SIMS $\delta^{18}O$ data does not provide further insight. Simultaneous measurements of $^{16}OH/^{16}O$ – a qualitative indicator of H-bearing inclusions (e.g. water or organic material) – are similar between samples in this study. No abnormalities were noted in the secondary ion count rates or relative yield (Table S2) of Fram Strait sample analyses. Furthermore, measurements of standard calcite are comparable between all of the analytical sessions (Table S2), indicating that the IRMS offset and variable $\delta^{18}O$ of Fram Strait samples must be caused by a characteristic unique to those shells.

4.4. Potential factors contributing to variability in SIMS results on plankton tow *N. pachyderma*

The most obvious difference between the Fram Strait plankton tow *N. pachyderma* and the Irminger Sea sediment trap shells is the texture or fabric of the polished shell walls that were analyzed by SIMS (Figure 2). Polished Fram Strait plankton tow shells display a clear granular texture in the microfabric of the chamber wall whereas the polished surfaces of the Irminger Sea *N. pachyderma* shells are smooth without texture. For precise and accurate SIMS analyses, it is prerequisite that the standard closely matches the sample with respect to mineralogy, crystal

structure, and trace/minor elemental composition (Valley and Kita, 2009). The *N. pachyderma* shells from plankton tows feature an apparent porous texture, in contrast with the smooth and homogenous texture of the marble standard. Though the texture of the plankton tow shells appear porous, the consistency in the count rate on the SIMS indicates that the data cannot be explained by void space. Rather, we postulate that the granular texture negatively affects the precision and accuracy of the SIMS $\delta^{18}O_{calcite}$ measurements of the Fram Strait plankton tow samples. Possible sources of the porous texture observed in the plankton tow samples could be a result of sample treatment/preparation or a shift in calcification causing modification of shell micro-structure with ontogeny. The former includes increased proportion of organics retained within the shell walls resulting in post-collection dissolution of calcite, dissolution caused by storage in ethanol, physical erosion of thin calcite walls during polishing, or a combination of these factors.

5 Conclusions

We have analyzed Mg/Ca and $\delta^{18}O$ in single *Neogloboquadrina pachyderma* shells from plankton tows deployed in the Fram Strait and a sediment trap from the Irminger Sea to investigate the geochemical patterns within and between shells to assess the utility of this species in paleoceanographic reconstructions. We combined Mg/Ca and $\delta^{18}O$ analyses on discrete domains within shells using LA-ICP-MS, EPMA, and SIMS, and were able to directly compare geochemical variability with micron-scale resolution. Hydrographic information that was measured concurrently with the collection of foraminifera allowed us to directly interpret the foraminiferal geochemistry in an environmental context. The plankton tow samples were collected along a transect across the Fram Strait, which exhibits large ranges in temperature, salinity, and $\delta^{18}O_{sw}$ allowing us to compare shell geochemistries across a relatively large environmental gradient. These data were compared and supplemented by sediment trap samples

from the seasonally isothermal and isohaline Irminger Sea in order to disentangle changes in temperature and salinity from biological or physiological factors. Our conclusions are as follows:

- Lamellar calcite in *N. pachyderma* Mg/Ca can potentially be used to calculate paleotemperatures using Equation 2 defined in this study. This relationship is significantly different from published equations using whole shells likely due to the low-Mg crust diluting the signal in whole shell measurements.
- LA-ICP-MS and EPMA results on plankton tow samples indicate that Mg/Ca banding is present in the lamellar calcite of *N. pachyderma*, while the LA-ICP-MS profiles on crusted sediment trap samples support previous observations that *N. pachyderma* crust calcite contains low Mg/Ca even in the absence of temperature variability.
- The agreement in LC and crust SIMS $\delta^{18}O_{calcite}$ data in trap-caught samples from the isothermal/isohaline Irminger Sea reveals that the source of the low Mg/Ca in *N. pachyderma* crust does not similarly influence the $\delta^{18}O$.
- An analytical offset of -0.7‰ is observed between IRMS and SIMS $\delta^{18}O_{calcite}$ data, which is similar to that described in *O. universa,* indicating that this offset is broadly applicable to all species of planktonic foraminifera and should be accounted for in published SIMS $\delta^{18}O$ results.
- The SIMS $\delta^{18}O_{calcite}$ results from the lamellar calcite of the Fram Strait plankton tow samples are quite variable and significantly more negative compared to the IRMS analyses on the same samples. IRMS $\delta^{18}O$ results on these shells agree with predicted $\delta^{18}O_{calcite}$ calculated using the $\delta^{18}O_{seawater}$ and salinity profiles from the sampling location.

- The granular microtexture of the Fram Strait plankton tow samples, in contrast to the Irminger Sea samples and the crystalline standard, could have degraded the precision and accuracy of the SIMS $\delta^{18}O_{calcite}$ results in those shells.

Overall, our results suggest that *N. pachyderma* shells remains a powerful proxy carrier for paleoceanographic reconstructions in the high latitudes, with the acknowledgement of a few outstanding considerations. As such, the LC-specific Mg/Ca to temperature relationship is a definite improvement over previous whole-shell equations as it excludes the low-Mg crust calcite, which has a different relationship between Mg/Ca and temperature. In terms of using the Mg/Ca ratio of *N. pachyderma* crust calcite to reconstruct temperatures at depth, the potential of deriving a Mg/Ca to temperature calibration may prove difficult as the mechanism controlling the homogenously low-Mg crust calcite remains unknown. Regarding the controls on $\delta^{18}O_{calcite}$ in *N. pachyderma*, this study reveals that IRMS-analyzed shells produce $\delta^{18}O$ values consistent with predicted $\delta^{18}O$ based on the temperature and $\delta^{18}O_{sw}$ using the paleotemperature equation of Kim and O'Neil (1997), while SIMS-analyzed shells produce an offset of -0.7‰. Furthermore, SIMS $\delta^{18}O$ analyses on crusted shells from the isothermal/isohaline Irminger Sea reveal that there is no difference between the lamellar and crust calcites, and therefore the crust and LC likely do not require distinct calibration relationships with respect to $\delta^{18}O$. Finally, the variable and imprecise SIMS $\delta^{18}O$ results on highly irregular and granular plankton tow shells indicates that the texture of shells might have a great impact on SIMS $\delta^{18}O$ results and therefore should be carefully examined to avoid inaccurate interpretations.

FIGURES

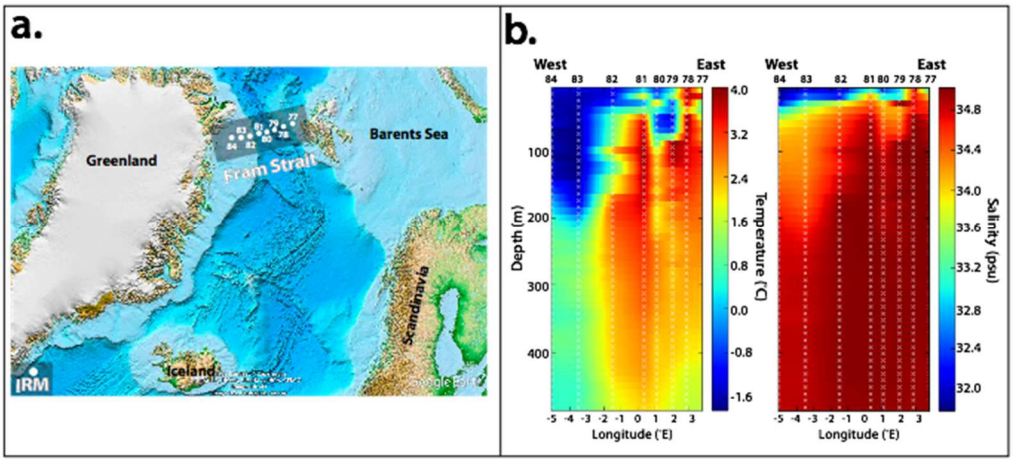

Figure 1.a. Map of the study area with the two study areas outlined by grey rectangles. The 8 stations across the Fram Strait are represented by white dots and labeled with their station number. The sediment traps from the Irminger Sea are denoted by a single white dot. **b.** West-East cross-sections of the Fram Strait study transect colored by temperature (ºC; left), and by salinity (psu; right) to 500 m depth. Temperature and salinity measurements were collected at each of the stations every 10 m in the z-direction (each white x represents a measurement) with interpolated results in between. X-axis is longitude (ºE) on the bottom and station # on the top.

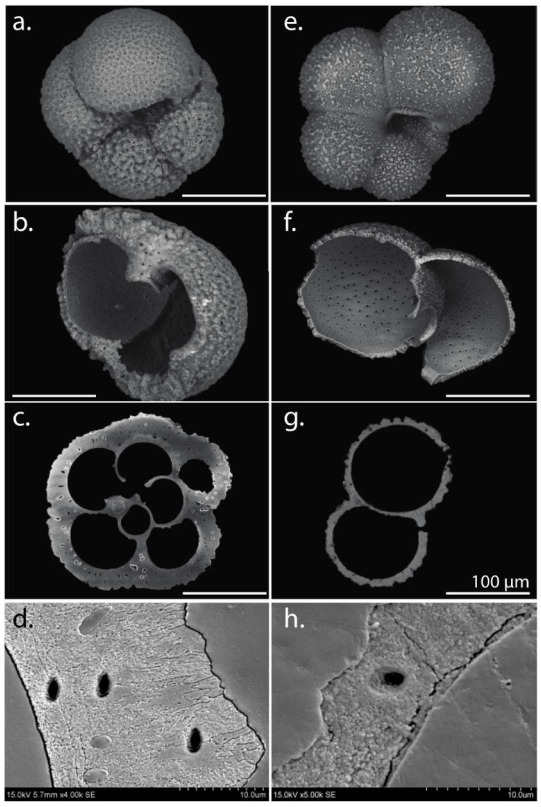

Figure 2. SEM images comparing crusted and uncrusted *N.pachyderma* shells in various stages of analysis to demonstrate differences in morphology and shell wall thickness. Tests in (a-d) are fully crusted shells from an Irminger Sea sediment trap, while those in (e-h) contain uncrusted shells collected across the Fram Strait. Shown are: (a,e) whole cleaned shells, (b,f) amputated shell fragments, and (c-d,g-h) polished cross-sections of shells in an epoxy mount. In b-d, the lamellar calcite can be seen as the thin inner layers that has been surrounded by the crust calcite. The difference in texture of the calcite between the two groups of shells is most apparent in d and h and are consistent across the samples (see SM for all SEMs). The Irminger Sea shells are smoother with evident interlocking calcite crystals and growth layers. The Fram Strait shells calcite appears more granular with higher porosity and less obvious structure to the shell walls. Scale bar is 100 µm in (a-d,e-g) and 10 µm in (d,h).

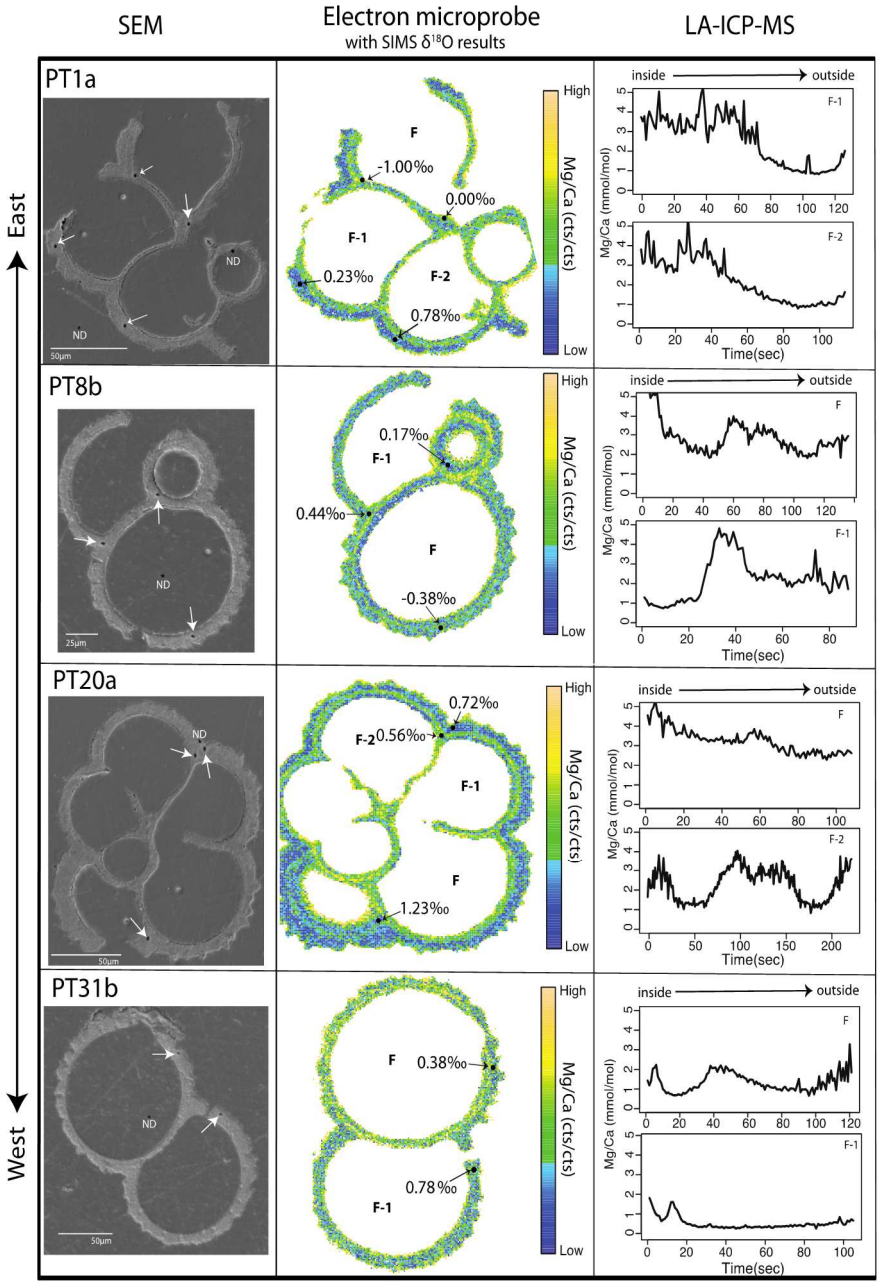

Figure 3. Compilation of geochemical results for four shells (PT1a, PT8b, PT20a, and PT31b) spanning the longitudinal transect in the Fram Strait from East to West (top to bottom). The left column shows SEM BSE images with SIMS pits (white arrows). Spots on the shells or surrounding epoxy that resemble SIMS pits but did not yield any $\delta^{18}O$ data are labeled "ND" for "no data". The middle column contains EPMA- generated Mg/Ca maps with a unique scale (counts/counts) for each shell and measured SIMS $\delta^{18}O$ values (‰VPDB; black arrows). Chambers are labeled by their relationship to the final (F) chamber. On the right are measured

LA-ICP-MS Mg/Ca (mmol/mol) profiles for two spots through the shell fragments. All profiles were taken from the inside of a shell to the outside.

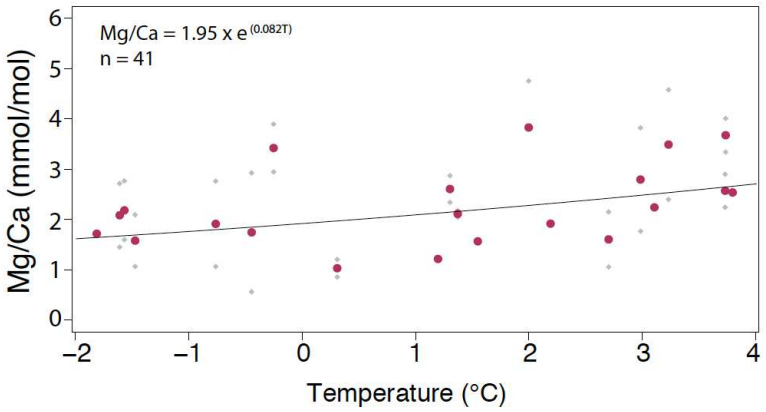

Figure 4. LA-ICP-MS Mg/Ca (mmol/mol) vs. temperature (°C) results from the lamellar calcite in individual Fram Strait *N. pachyderma* shells (small grey diamonds) with the average Mg/Ca value at each recorded temperature (solid circles). Each diamond is the average Mg/Ca ratio for all ablation profiles through an individual shell. The solid circles represent the arithmetic mean Mg/Ca from all profiles that were analyzed at that temperature. Exponential regression (equation 1) is through the individual shell values (small grey diamonds).

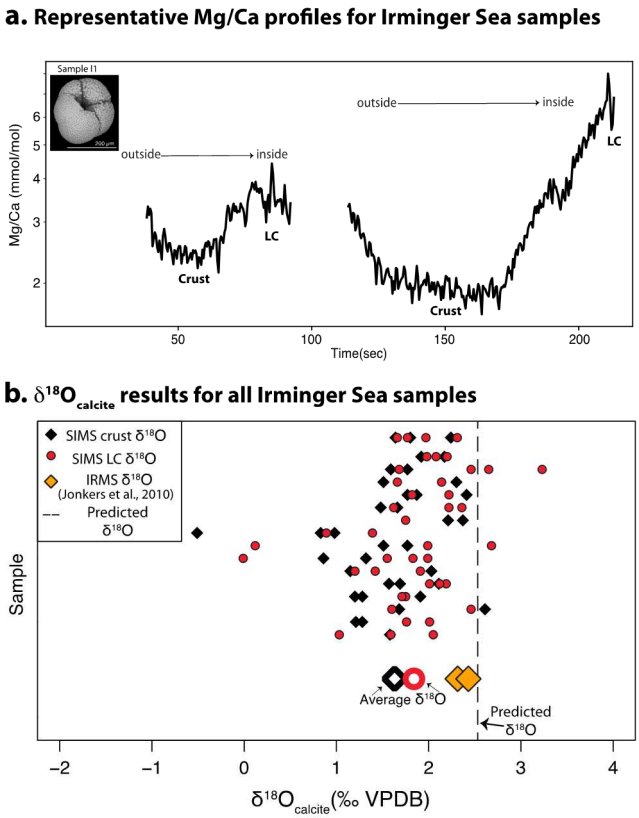

Figure 5. a. Two representative LA-ICP-MS Mg/Ca (mmol/mol) profiles through a single *N. pachyderma* shell fragment from the Irminger Sea with the crust and lamellar calcite domains labeled (Sample I1). b. Plot of Irminger Sea sediment trap collected *N. pachyderma* $\delta^{18}O_{calcite}$ results. SIMS $\delta^{18}O_{calcite}$ (‰VPDB) data shown in red circles (lamellar calcite) and black diamonds (crust calcite). Average $\delta^{18}O_{calcite}$ (‰VPDB) for all spots within the lamellar and crust calcites respectively are shown in larger hollow symbols below the individual results. Published IRMS results on pooled shells shown in orange diamonds (Jonkers et al., 2010), and predicted $\delta^{18}O_{calcite}$ (‰VPDB) for the water column is denoted by a vertical line.

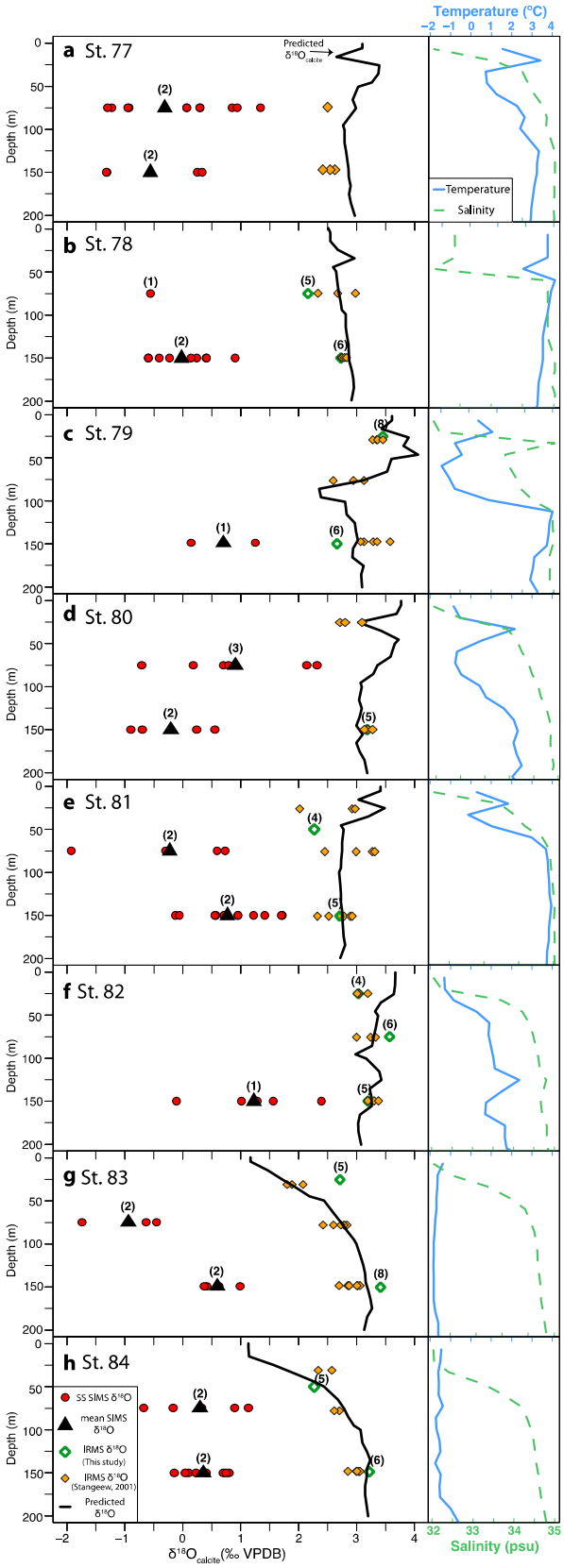
Temperature (°C)
−2 −1 0 1 2 3 4
a St. 77
b St. 78
c St. 79
d St. 80
e St. 81
f St. 82
g St. 83
h St. 84
Predicted δ18Ocalcite
Temperature
Salinity
Depth (m)
0
50
100
150
200
(1)
(2)
(3)
(4)
(5)
(6)
(8)
SS SIMS δ18O
mean SIMS δ18O
IRMS δ18O (This study)
IRMS δ18O (Stangeew, 2001)
Predicted δ18O
−2 −1 0 1 2 3 4
δ18Ocalcite (‰ VPDB)
32 33 34 35
Salinity (psu)

Figure 6. Composite of plankton tow collected *N. pachyderma* $\delta^{18}O_{calcite}$ (‰VPDB) results (left) alongside the CTD measured temperature and salinity (right) for the upper 200 m for the eight stations (77-84) from East to West across the Fram Strait. $\delta^{18}O_{calcite}$ (‰VPDB) results from SIMS analysis are shown as individual spots (SS) in red circles and the average of all shells from given station/depth in black triangles. The "n" indicated is the total number of shells included in the averaged value. IRMS $\delta^{18}O_{calcite}$ (‰VPDB) results on pooled shells are shown in green hollow diamonds with published IRMS $\delta^{18}O_{calcite}$ results from the same tows shown in orange solid diamonds (Stangeew, 2001). All $\delta^{18}O_{calcite}$ data are plotted at the average depths of their respective tows (more details in Table 2). The predicted $\delta^{18}O_{calcite}$ (‰) for each station (solid black line) was calculated using the paleotemperature equation from Kim and O'Neil (1997) with the CTD measured temperature and $\delta^{18}O_w$ from 0-200 m.

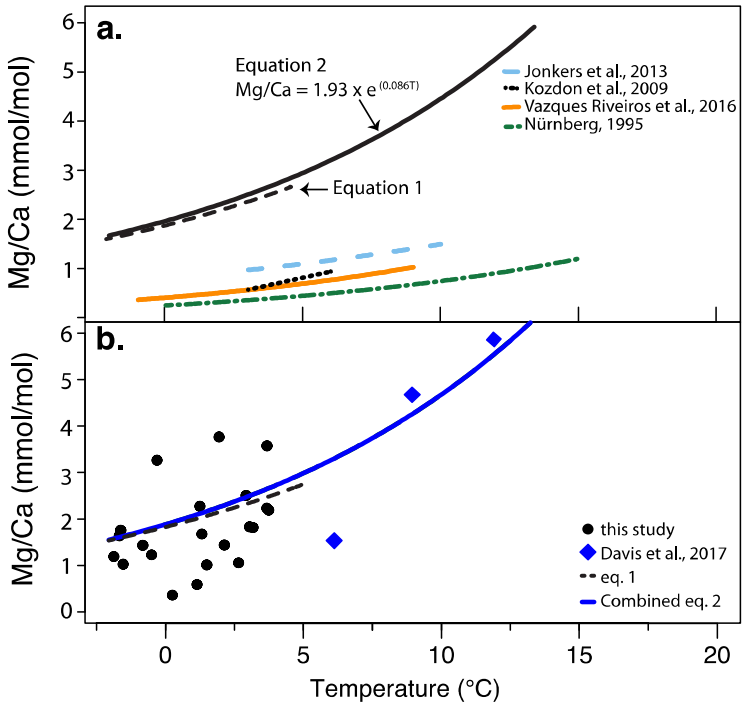

Figure 7.a. Plot of published *N.pachyderma* Mg/Ca (mmol/mol) vs. temperature (°C) relationships labeled with their corresponding references (Table 3) alongside the relationship generated from data collected in this study (equation 1) and the combined relationship with the 9 and 12°C data from Davis et al., 2017 (equation 2;

see discussion for details). All relationships extend throughout the temperature range in which they were calibrated. **b.** Average Mg/Ca values at each recorded temperature from the Fram Strait (black spots; same data as the solid circles in Figure 4) with equation 1 (dashed line). Blue diamonds are data from cultured *N. pachyderma* at 6, 9 and 12°C from Davis et al., 2017 with combined equation 2 (solid blue line). The large difference between eqs. 1 and 2 and the published equations is due to the low-Mg crust calcite dominating the signal in the latter equations.

Table 1. LA-ICP-MS operating procedures and data reduction parameters.

ICPMS: Agilent 7700x	**Data reduction: LAtools**
RF Power: 1350 W	Despiking data: exponential decay and signal smoothing
Argon (carrier) gas flow: 0.95 – 1.0 L/min	
Ar coolant gas flow: 15 L/min	Background correction: 1D interpolation
Ar auxiliary gas flow: 1 L/min	Calibration: NIST 610-612-614
Dwell time per mass: 20-40 ms	Internal standard: ^{43}Ca
Total sweep time: 240 s	Filters: Mn/Ca and Al/Ca < 0.5 nmol/mol
Laser-ablation system: UV Excimer Laser	
Energy density (fluence): 0.87-1.44 J/cm^2	
He gas flow: 1.05 L/min	
Laser repetition rate: 5 Hz	
Laser spot size: 40 µm square spot	
ThO+/Th+: <0.4%	

Table 2. Summary of measured $\delta^{18}O_{calcite}$ (‰ VPDB) of plankton tow collected *N. pachyderma* lamellar calcite at various depths at each of the eight stations across the Fram Strait. Stations 77 and 78 did not have significant shells in the shallowest tows (0-50 m) and therefore do not have any $\delta^{18}O_{calcite}$ results from those depths. The average $\delta^{18}O_{calcite}$ (‰ VPDB) measured on the SIMS and the IRMS are shown with the difference between the two averaged measurements to demonstrate the offset between the two analytical techniques. Also shown is the $\delta^{18}O_{water}$ (‰VSMOW) measured on water samples collected concurrent with the plankton tows.

Station	Collection depth (m)	Average SIMS $\delta^{18}O_{calcite}$ (‰VPDB +/- 2SE)	# shells (# of spots)	IRMS $\delta^{18}O_{calcite}$ (‰VPDB)	# shells	Δ $\delta^{18}O_{calcite}$ SIMS-IRMS (‰VPDB)	IRMS $\delta^{18}O_{calcite}$ (‰VPDB +/- 2SE) from Stangeew, 2001	# samples	Measured $\delta^{18}O_{water}$ (‰VSMOW)
77	50-100	-0.36 (+/- 0.73)	2 (12)	-	-	-	2.39	1	0.25
77	100-200	-0.57 (+/- 0.93)	2 (4)	-	-	-	2.42 (+/- 0.15)	3	0.2
78	50-100	-0.6	1 (1)	2.16	5	-2.76	2.67 (+/- 0.44)	3	0.27
78	100-200	0.06 (+/- 0.37)	2 (9)	2.73	6	-2.67	2.8 (+/- 0.05)	4	0.28
79	0-50	-	-	3.45	8	-	3.33 (+/- 0.06)	3	0.86
79	50-100	-	-	-	-	-	2.8 (+/- 0.38)	3	0.07
79	100-200	-0.5 (+/-3.33	1 (2)	2.66	6	-3.16	2.83 (+/- 0.22)	5	0.29
80	0-50	-	-	-	-	-	3.15 (+/- 0.40)	3	0.14
80	50-100	0.96 (+/- 0.96)	2 (6)	-	-	-	-	-	0.15
80	100-200	-0.17 (+/- 0.72)	2 (4)	3.27	5	-3.44	3.29 (+/- 0.08)	3	0.25
81	0-50	-	-	-	-	-	2.54 (+/- 0.73)	3	0.15
81	50-100	-0.21 (+/- 1.22)	2 (4)	-	-	-	2.98 (+/- 0.47)	4	0.29
81	100-200	0.78 (+/- 0.42)	2 (9)	2.62	5	-1.84	2.60 (+/- 0.22)	6	0.23
82	0-50	-		3.03	4	-	3.07 (+/- 0.14)	3	-0.07
82	50-100	-	-	3.57	6	-	3.14 (+/- 0.23)	3	0.06
82	100-200	0.99 (+/- 0.81)	1 (5)	3.2	5	-2.21	3.26 (+/- 0.13)	3	0.17
83	0-50	-	-	2.71	5	-	1.68 (+/- 0.19)	3	-1.67
83	50-100	-1.03 (+/- 0.84)	2 (3)	-	-	-	2.58 (+/- 0.15)	6	-0.79
83	100-200	0.58 (+/- 0.30)	2 (4)	3.41	8	-2.83	2.84 (+/- 0.1)	8	-0.23
84	0-50	-	-	-	-	-	2.33 (+/- 0.27)	2	-1.97
84	50-100	0.27 (+/- 0.69)	2 (5)	-	-	-	2.56 (+/- 0.1)	2	-0.85
84	100-200	0.33 (+/- 0.26)	2 (8)	3.22	6	-2.89	2.95 (+/- 0.07)	6	-0.2

Table 3. Published Mg/Ca vs. temperature relationships for *Neogloboquadrina pachyderma*.

Reference	Equation	Temperature range (ºC)	Sample type	Sample location
Jonkers et al., 2013	Mg/Ca=0.60∗e^(0.09∗T)	5-10	sediment trap	Irminger Sea
Kozdon et al., 2009	Mg/Ca=0.13*T + 0.35	3-6	core-top	Norwegian Sea
Nürnberg, 1995	Mg/Ca=0.41* e^(0.083*T)	0-15	core-top	Norwegian Sea
Vazques Riveiros et al., 2016	Mg/Ca= 0.58* e^(0.084*T)	-1-9	core-top	Southern Ocean
This study (eq. 2)	Mg/Ca= 0.93* e^(0.086*T)	-2-12	plankton tow and cultured specimens	Fram Strait and Bodega Bay, CA

REFERENCES

Allen, K. A., & Hönisch, B. (2012). The planktic foraminiferal B/Ca proxy for seawater carbonate chemistry: A critical evaluation. *Earth and Planetary Science Letters, 345*, 203–211.

Arikawa, R. (1983). Distribution and taxonomy of *Globigerina pachyderma* (Ehrenberg) off the Sanriku coast, Northeast Honshu, Japan (*Globoquadrina dutertrei*). *Science Reports - Tohoku University, Second Series: Geology, 53*(2), 103–157.

Bauch, D., Carstens, J., & Wefer, G. (1997). Oxygen isotope composition of living *Neogloboquadrina pachyderma* (sin.) in the Arctic Ocean. *Earth and Planetary Science Letters, 146*(1–2), 47–58.

Bolton, A., & Marr, J. P. (2013). Trace element variability in crust-bearing and non crust-bearing *Neogloboquadrina incompta*, P-D intergrade and *Globoconella inflata* from the Southwest Pacific Ocean: Potential paleoceanographic implications. *Marine Micropaleontology, 100*, 21–33.

Branson, O., Fehrenbacher, J. S., Vetter, L., Sadekov, A. Y., Eggins, S. M., & Spero, H. J. (2019). LAtools: A data analysis package for the reproducible reduction of LA-ICPMS data. *Chemical Geology, 504*, 83–95.

Bryan, F. (1986). High-latitude salinity effects and interhemispheric thermohaline circulations. *Nature, 323*, 301.

Carstens, J., & Wefer, G. (1992). Recent distribution of planktonic foraminifera in the Nansen Basin, Arctic Ocean. *Deep Sea Research Part A. Oceanographic Research Papers, 39*(2), S507–S524.

Cavosie, A. J., Valley, J. W., & Wilde, S. A. (2005). Magmatic $\delta^{18}O$ in 4400–3900 Ma detrital zircons: A record of the alteration and recycling of crust in the Early Archean. *Earth and Planetary Science Letters, 235*(3–4), 663–681.

Cokelet, E. D., Tervalon, N., & Bellingham, J. G. (2008). Hydrography of the West Spitsbergen Current, Svalbard Branch: Autumn 2001. *Journal of Geophysical Research: Oceans, 113*(1), 1–16.

Consolaro, C., Rasmussen, T. L., & Panieri, G. (2018). Palaeoceanographic and environmental changes in the eastern Fram Strait during the last 14,000 years based on benthic and planktonic foraminifera. *Marine Micropaleontology, 139*(December 2016), 84–101.

Coplen, T. B., Kendall, C., & Hopple, J. (1983). Comparison of stable isotope reference samples. *Nature, 302*(5905), 236.

Davis, C. V., Fehrenbacher, J. S., Hill, T. M., Russell, A. D., & Spero, H. J. (2017). Relationships Between Temperature, pH, and Crusting on Mg/Ca Ratios in Laboratory-Grown Neogloboquadrina Foraminifera. *Paleoceanography, 32*(11), 1137–1152.

de Jong, M. F., van Aken, H. M., Våge, K., & Pickart, R. S. (2012). Convective mixing in the central Irminger Sea: 2002–2010. *Deep Sea Research Part I: Oceanographic Research Papers*, *63*, 36–51.

Duckworth, D. (1977). Magnesium concentration in the tests of the planktonic foraminifer *Globorotalia truncatulinoides. Journal of Foraminiferal Research, 7*(4), 304-312.

Duplessy, J. C., Bé, A. W. H., & Blanc, P. L. (1981). Oxygen and carbon isotopic composition and biogeographic distribution of planktonic foraminifera in the Indian Ocean. *Palaeogeography, Palaeoclimatology, Palaeoecology, 33*(1), 9–46.

Eggins, S., De Deckker, P., & Marshall, J. (2003). Mg/Ca variation in planktonic foraminifera tests: Implications for reconstructing -palaeo-seawater temperature and habitat migration. *Earth and Planetary Science Letters, 212*(3–4), 291–306.

Eggins, S. M., Sadekov, A., & De Deckker, P. (2004). Modulation and daily banding of Mg/Ca in *Orbulina universa* tests by symbiont photosynthesis and respiration: A complication for seawater thermometry? *Earth and Planetary Science Letters, 225*(3–4), 411–419.

Emiliani, C. (1955). Pleistocene temperature variations in the Mediterranean. *The Journal of Geology 63*(6), 538-578.

Emiliani, C., Mayeda, T., & Selli, R. (1961). Paleotemperature analysis of the Plio-Pleistocene section at Le Castella, Calabria, southern Italy. *Geological Society of America Bulletin, 72*(5), 679–688.

Epstein, S., Buchsbaum, R., Lowenstam, H. A., & Urey, H. C. (1953). Revised carbonate-water isotopic temperature scale. *GSA Bulletin, 64*(11), 1315–1326.

Erez, J. (2003). The source of ions for biomineralization in foraminifera and their implications for paleoceanographic proxies. *Reviews in Mineralogy and Geochemistry 54*(1), 115-149.

Fehrenbacher, J., & Martin, P. (2010). Mg/Ca variability of the planktonic foraminifera *G. ruber s.s.* and *N. dutertrei* from shallow and deep cores determined by electron microprobe image mapping. *IOP Conference Series: Earth and Environmental Science, 9*, 012018.

Fehrenbacher, J. S., Spero, H. J., Russell, A. D., Vetter, L., & Eggins, S. (2015). Optimizing LA-ICP-MS analytical procedures for elemental depth profiling of foraminifera shells. *Chemical Geology, 407–408*, 2–9.

Fehrenbacher, J. S., Russell, A. D., Davis, C. V., Gagnon, A. C., Spero, H. J., Cliff, J. B., et al. (2017). Link between light-triggered Mg-banding and chamber formation in the planktic foraminifera *Neogloboquadrina dutertrei*. *Nature Communications, 8*(May), 1-10.

Greco, M., Jonkers, L., Kretschmer, K., Bijma, J., & Kucera, M. (2019). Depth habitat of the planktonic foraminifera *Neogloboquadrina pachyderma* in the northern high latitudes explained by sea-ice and chlorophyll concentrations. *Biogeosciences*, *16*(17), 3425–3437.

Hathorne, E. C., Alard, O., James, R. H., & Rogers, N. W. (2003). Determination of intratest variability of trace elements in foraminifera by laser ablation inductively coupled plasma-mass spectrometry. *Geochemistry, Geophysics, Geosystems, 4*(12), 1-14.

Hathorne, Ed C, James, R. H., & Lampitt, R. S. (2009). Environmental versus biomineralization controls on the intratest variation in the trace element composition of the planktonic foraminifera *G. inflata* and *G. scitula*. *Paleoceanography, 24*(4), 1-14.

Hemleben, C., Spindler, M., Breitinger, I., & Deuser, W. G. (1985). Field and laboratory studies on the ontogeny and ecology of some globorotaliid species from the Sargasso Sea off Bermuda. *Journal of Foraminiferal Research, 15*(4), 254–272.

Hendry, K. R., Rickaby, R. E. M., Meredith, M. P., & Elderfield, H. (2009). Controls on stable isotope and trace metal uptake in *Neogloboquadrina pachyderma* (sinistral) from an Antarctic sea-ice environment. *Earth and Planetary Science Letters*, *278*(1–2), 67–77.

Hönisch, B., Allen, K. A., Russell, A. D., Eggins, S. M., Bijma, J., Spero, H. J., et al. (2011). Planktic foraminifers as recorders of seawater Ba/Ca. *Marine Micropaleontology, 79*(1–2), 52–57.

Hönisch, B., Allen, K. A., Lea, D. W., Spero, H. J., Eggins, S. M., Arbuszewski, J., et al. (2013). The influence of salinity on Mg/Ca in planktic foraminifers - Evidence from cultures, core-top sediments and complementary $\delta^{18}O$. *Geochimica et Cosmochimica Acta, 121*, 196–213.

Jonkers, L., Brummer, G. J. A., Peeters, F. J. C., Van Aken, H. M., & De Jong, M. F. (2010). Seasonal stratification, shell flux, and oxygen isotope dynamics of leftcoiling *N. pachyderma* and *T. quinqueloba* in the western subpolar North Atlantic. *Paleoceanography, 25*(2), 1–13.

Jonkers, L., De Nooijer, L. J., Reichart, G. J., Zahn, R., & Brummer, G. J. A. (2012). Encrustation and trace element composition of *Neogloboquadrina dutertrei* assessed from single chamber analyses- implications for paleotemperature estimates. *Biogeosciences, 9*(11), 4851-4860.

Jonkers, L., Jiménez-Amat, P., Mortyn, P. G., & Brummer, G. J. A. (2013). Seasonal Mg/Ca variability of *N. pachyderma* (s) and *G. bulloides*: Implications for seawater temperature reconstruction. *Earth and Planetary Science Letters, 376*, 137–144.

Jonkers, L., Buse, B., Brummer, G. J. A., & Hall, I. R. (2016). Chamber formation leads to Mg/Ca banding in the planktonic foraminifer *Neogloboquadrina pachyderma*. *Earth and Planetary Science Letters, 451*, 177–184.

Jonkers, L., & Kučera, M. (2017). Quantifying the effect of seasonal and vertical habitat tracking on planktonic foraminifera proxies. *Climate of the Past*, *13*(6), 573–586.

Kohfeld, K. E., Fairbanks, R. G., Smith, S. L., & Walsh, I. D. (1996). *Neogloboquadrina pachyderma* (sinistral coiling) as paleoceanographic tracers in polar oceans: Evidence from Northeast Water Polynya plankton tows, sediment traps, and surface sediments. *Paleoceanography, 11*(6), 679–699.

Kozdon, R., Ushikubo, T., Kita, N. T., Spicuzza, M., & Valley, J. W. (2009). Intratest oxygen isotope variability in the planktonic foraminifer *N. pachyderma*: Real vs. apparent vital effects by ion microprobe. *Chemical Geology, 258*(3–4), 327–337.

Kozdon, Reinhard, Kelly, D. C., Kita, N. T., Fournelle, J. H., & Valley, J. W. (2011). Planktonic foraminiferal oxygen isotope analysis by ion microprobe technique suggests warm tropical sea surface temperatures during the Early Paleogene. *Paleoceanography, 26*(3), 1–17.

Kozdon, Reinhard, Kelly, D. C., Kitajima, K., Strickland, A., Fournelle, J. H., & Valley, J. W. (2013). In situ $\delta^{18}O$ and Mg/Ca analyses of diagenetic and planktic foraminiferal calcite preserved in a deep□sea record of the Paleocene□Eocene thermal maximum. *Paleoceanography, 28*(3), 517–528.

Kucera, M. (2007). Chapter Six Planktonic Foraminifera as Tracers of Past Oceanic Environments. *Developments in Marine Geology, 1*(07), 213–262.

Kunioka, D., Shirai, K., Takahata, N., Sano, Y., Toyofuku, T., & Ujiie, Y. (2006). Microdistribution of Mg/Ca, Sr/Ca, and Ba/Ca ratios in *Pulleniatina obliquiloculata* test by using a NanoSIMS: Implication for the vital effect mechanism. *Geochemistry, Geophysics, Geosystems, 7*(12), 1-11.

Lea, D. W., Mashiotta, T. A., & Spero, H. J. (1999). Controls on magnesium and strontium uptake in planktonic foraminifera determined by live culturing. *Geochimica et Cosmochimica Acta, 63*(16), 2369–2379.

Linzmeier, B. J., Kozdon, R., Peters, S. E., & Valley, J. W. (2016). Oxygen Isotope Variability within Nautilus Shell Growth Bands. *PLOS ONE, 11*(4), 1-31.

Mashiotta, T., Lea, D. W., & Spero, H. J. (1999). Glacial-interglacial changes in subantarctic sea surface temperature and $\delta^{18}O$-water using foraminiferal Mg. *Earth and Planetary Science Letters, 170*(May), 417–432.

Nürnberg, D. (1995). Magnesium in tests of *Neogloboquadrina pachyderma* sinistral from high northern and southern latitudes. *Journal of Foraminiferal Research 25*, 350-368.

Nürnberg, D., Bijma, J., & Hemleben, C. (1996). Assessing the reliability of magnesium in foraminiferal calcite as a proxy for water mass temperatures. *Geochimica et Cosmochimica Acta, 60*(5), 803–814.

O'Neil, J., & Kim, S.-T. (1997). Equilibrium and nonequilibrium oxygen isotope effects in synthetic carbonates. *Geochimica et Cosmochimica Acta, 61*(16), 3461–3475.

Pearson, P. N. (2012). Oxygen Isotopes in Foraminifera : Overview and Historical Review. *The Paleontological Society Papers, 18*, 1–38.

Pena, L. D., Cacho, I., Calvo, E., Pelejero, C., Eggins, S., & Sadekov, A. (2008). Characterization of contaminant phases in foraminifera carbonates by electron microprobe mapping. *Geochemistry, Geophysics, Geosystems*, *9*(7), 1-12.

Ravelo, A. C., & Hillaire-Marcel, C. (2007). Chapter Eighteen The Use of Oxygen and Carbon Isotopes of Foraminifera in Paleoceanography. *Developments in Marine Geology, 1*(07), 735–764.

Reiss, Z. (1957). The Bilamellidea, nov. superfam. and remarks on Cretaceous Globorotaliids. *Contributions to Cushman Foundation Foraminiferal Research 8*(1), 127-145.

Sadekov, A. Y., Eggins, S. M., & De Deckker, P. (2005). Characterization of Mg/Ca distributions in planktonic foraminifera species by electron microprobe mapping. *Geochemistry, Geophysics, Geosystems, 6*(12), 411-419.

Sadekov, A. Y., Eggins, S. M., Klinkhammer, G. P., & Rosenthal, Y. (2010). Effects of seafloor and laboratory dissolution on the Mg/Ca composition of *Globigerinoides sacculifer* and *Orbulina universa* tests - A laser ablation ICPMS microanalysis perspective. *Earth and Planetary Science Letters, 292*(3–4), 312–324.

Simstich, J., Sarnthein, M., & Erlenkeuser, H. (2003). Paired $\delta^{18}O$ signals of *Neogloboquadrina pachyderma* (s) and *Turborotalita quinqueloba* show thermal stratification structure in Nordic Seas. *Marine Micropaleontology, 48*(1–2), 107–125.

Spero, H. J., Eggins, S. M., Russell, A. D., Vetter, L., Kilburn, M. R., & Hönisch, B. (2015). Timing and mechanism for intratest Mg/Ca variability in a living planktic foraminifer. *Earth and Planetary Science Letters, 409*, 32–42.

Stangeew, E. (2001). Distribution and Isotopic Composition of Living Planktonic Foraminifera *N. pachyderma* (sinistral) and *T. quinqueloba* in the High Latitude North Atlantic. Doctoral dissertation, Christian-Albrechts Universität Kiel, Germany, 1-98.

Steinhardt, J., Cléroux, C., De Nooijer, L. J., Brummer, G. J., Zahn, R., Ganssen, G., & Reichart, G. J. (2015). Reconciling single-chamber Mg / Ca with whole-shell $\delta^{18}O$ in surface to deep-dwelling planktonic foraminifera from the Mozambique Channel. *Biogeosciences, 12*(8), 2411–2429.

Urey, H. C. (1948). Oxygen Isotopes in Nature and in the Laboratory. *Science, 108*(2810), 489 – 496.

Valley, J. W., & Kita, N. T. (2009). In situ oxygen isotope geochemistry by ion microprobe. *MAC Short Course: Secondary Ion Mass Spectrometry in the Earth Sciences, 41*, 19–63.

Vàzquez Riveiros, N., Govin, A., Waelbroeck, C., Mackensen, A., Michel, E., Moreira, S., Bouinot, T., Caillon, N., Orgun, A., Brandon, M. (2016). Mg/Ca thermometry in planktic

foraminifera: Improving paleotemperature estimations for *G. bulloides* and *N. pachyderma* left. *Geochemistry, Geophysics, Geosystems, 17*(4), 1247-1566.

Vetter, L., Spero, H. J., Russell, A. D., & Fehrenbacher, J. S. (2013a). LA□ICP□MS depth profiling perspective on cleaning protocols for elemental analyses in planktic foraminifers. *Geochemistry, Geophysics, Geosystems, 14*(8), 2916–2931.

Vetter, L., Kozdon, R., Mora, C. I., Eggins, S. M., Valley, J. W., Hönisch, B., & Spero, H. J. (2013b). Micron-scale intrashell oxygen isotope variation in cultured planktic foraminifers. *Geochimica et Cosmochimica Acta, 107*, 267–278.

Vetter, L., Spero, H. J., Eggins, S. M., Williams, C., & Flower, B. P. (2017). Oxygen isotope geochemistry of Laurentide ice-sheet meltwater across Termination I. *Quaternary Science Reviews, 178*, 102–117.

Wu, G., & Hillaire-Marcel, C. (1994). Oxygen isotope compositions of sinistral *Neogloboquadrina pachyderma* tests in surface sediments: North Atlantic Ocean. *Geochimica et Cosmochimica Acta, 58*(4), 1303–1312.

Wycech, J. B., Kelly, D. C., Kitajima, K., Kozdon, R., Orland, I. J., & Valley, J. W. (2018). Combined effects of gametogenic calcification and dissolution on $\delta^{18}O$ measurements of the planktic foraminifer *Trilobatus sacculifer*. *Geochemistry, Geophysics, Geosystems, 19*(11), 4487–4501.

Wycech, J. B., Kelly, D. C., Kozdon, R., Orland, I. J., Spero, H. J., & Valley, J. W. (2018). Comparison of $\delta^{18}O$ analyses on individual planktic foraminifer (*Orbulina universa*) shells by SIMS and gas-source mass spectrometry. *Chemical Geology, 483*, 119–130.

Zeebe, R. E., Zachos, J. C., Caldeira, K., & Tyrrell, T. (2008). Carbon emissions and acidification. *Science, 321*(5885), 51–52.

Zweng, M. M., Boyer, T. P., Baranova, O. K., Reagan, J. R., Seidov, D., & Smolyar, I. V. (2018). An inventory of Arctic Ocean data in the World Ocean Database. *Earth System Science Data, 10*(1), 677–687.

SUPPLEMENTARY MATERIALS

Table S1. Fram Strait multinet samples sampling locations. Shading denotes all shells from each station. PT = plankton tow. S= shells from the surface (0-50 m) tows.

Sample	Station	Latitude	Longitude	Water depth (m)
PT1	77	80°10.1'N	03°48.3'E	1441
PT2	77			
PT2S	77			
PT3	77			
PT4	77			

PT5	78	80°08.7'N	02°53.2'E	1992
PT6	78			
PT7	78			
PT8	78			
PT9	79	80°09.6'N	02°00.8'E	2016
PT10	79			
PT11	79			
PT11S	79			
PT12S	79			
PT13	80	80°08.5'N	01°05.7'E	2854
PT14	80			
PT15	80			
PT15S	80			
PT16	80			
PT17	81	80°11.9'N	00°19.6'E	3000
PT18	81			
PT19	81			
PT20	81			
PT20S	81			
PT21	82	80°06.4'N	01°28.8'W	2848
PT22	82			
PT23	82			
PT24	82			
PT25S	82			
PT26S	82			
PT25	83	79°59.5'N	03°31.3'W	2290
PT26	83			
PT27	83			
PT28	83			
PT30S	83			
PT31S	83			
PT29	84	79°56.0'N	05°06.1'W	1150
PT30	84			
PT31	84			
PT32	84			

Table S2. *in situ* oxygen isotope ($\delta^{18}O$) measurements, in the order of analysis, for the Fram Strait plankton tow samples (PT) and the Irminger Sea samples with the bracketing UWC-3 calcite standards. Any spots with <1.5 Mcps/pA or $^{16}OH/^{16}O$ ratios >3.00e^{-2} were excluded from results.

Analysis #	Sample	$\delta^{18}O$ ‰ VSMOW [a]	2SD (ext.) [b]	$\delta^{18}O$ ‰ VPDB [c]	$\delta^{18}O$ ‰ measured [d]	^{16}O (Mcps) [e]	$^{16}OH/^{16}O$ [f]	Yield (Mcps/ pA)
Sample Mount Fram Strait PT3								
9	PT3 UWC3 G1				-7.93	29.91	3.66E-03	1.99
10	PT3 UWC3 G1				-7.81	28.99	3.71E-03	1.93
11	PT3 UWC3 G1				-7.81	29.14	3.42E-03	1.94

12	PT3 UWC3 G1				-7.85	29.16	3.72E-03	2.08
	average and ±2SD				**-7.85 ± 0.11**			
14	PT3 16a_02	30.22	0.65	-0.67	9.60	26.44	1.74E-02	1.89
15	PT3 16a_03	31.20	0.65	0.28	10.56	26.09	1.98E-02	1.86
16	PT3 17b_01	28.94	0.65	-1.91	8.35	26.60	1.99E-02	1.90
17	PT3 17b_02	31.54	0.65	0.61	10.90	26.17	1.71E-02	1.87
18	PT3 3a_01	29.50	0.65	-1.37	8.90	26.27	2.02E-02	2.02
19	PT3 3a_02	31.11	0.65	0.19	10.48	25.61	1.84E-02	1.97
20	PT3 3a_03	31.19	0.65	0.27	10.56	25.29	1.88E-02	1.95
21	PT3 UWC3 G1				-7.65	26.75	3.87E-03	2.06
22	PT3 UWC3 G1				-8.30	26.63	3.99E-03	2.05
23	PT3 UWC3 G1				-7.14	27.56	4.40E-03	1.97
24	PT3 UWC3 G1;				-7.64	27.77	4.25E-03	1.98
	Bracket (analyses 9-12, 21-24): average and ±2SD				**-7.77 ± 0.65**			
25	PT3 2a_01	31.34	1.21	0.42	10.39	26.71	1.52E-02	1.91
26	PT3 2a_02	29.75	1.21	-1.12	8.83	26.12	1.84E-02	1.87
27	PT32a_03	29.65	1.21	-1.22	8.73	25.98	1.77E-02	1.86
28	PT3 1a_01	31.27	1.21	0.35	10.31	26.67	1.50E-02	2.05
29	PT3 1a_02	29.96	1.21	-0.92	9.04	25.91	2.89E-02	1.99
30	PT3 1a_03	31.76	1.21	0.83	10.80	26.64	1.55E-02	2.05
31	PT3 1a_04	30.92	1.21	0.01	9.97	25.99	1.73E-02	2.00
32	PT3 8a_01	31.84	1.21	0.91	10.88	26.49	1.30E-02	2.04
33	PT3 8a_02	30.63	1.21	-0.27	9.69	25.45	1.92E-02	1.96
34	PT3 8a_03	30.21	1.21	-0.68	9.28	25.61	2.32E-02	1.97
35	PT3 UWC3 G1				-8.57	27.00	3.66E-03	2.08
36	PT3 UWC3 G1				-7.65	26.48	4.17E-03	2.04
37	PT3 UWC3 G1				-8.08	27.48	5.58E-03	1.96
38	PT3 UWC3 G1				-8.87	28.88	3.31E-03	2.06
39	PT3 UWC3 G1				-8.84	29.31	3.62E-03	2.09

	Bracket (analyses 21-24, 35-39): average and ±2SD				**-8.08 ± 1.21**			
40	PT3 20a_01	31.96	1.43	1.02	10.09	28.13	1.75E-02	2.01
41	PT3 20a_02	32.06	1.43	1.12	10.19	28.37	1.47E-02	2.03
42	PT3 20a_03	32.53	1.43	1.57	10.65	28.40	1.47E-02	2.03
43	PT3 19a_01	31.78	1.43	0.85	9.92	28.03	1.58E-02	2.00
44	PT3 19a_02	32.59	1.43	1.63	10.70	27.52	1.31E-02	1.97
45	PT3 14a_01	31.91	1.43	0.97	10.04	26.66	2.31E-02	1.90
46	PT3 14a_02	33.24	1.43	2.26	11.35	26.76	1.57E-02	1.91
47	PT3 14a_03	33.36	1.43	2.37	11.46	27.51	1.34E-02	1.97
48	PT3 7a_01	31.08	1.43	0.17	9.23	28.61	1.80E-02	2.04
49	PT3 7a_02	30.13	1.43	-0.75	8.30	27.56	1.67E-02	1.97
51	PT3 5b_02	29.93	1.43	-0.95	8.11	27.60	1.77E-02	1.44
52	PT3 UWC3 G1				-9.65	28.95	3.62E-03	2.07
53	PT3 UWC3 G1				-9.46	28.45	3.54E-03	2.03
54	PT3 UWC3 G1				-9.67	28.60	3.72E-03	2.04
55	PT3 UWC3 G1				-9.77	28.05	3.89E-03	2.00
56	PT3 UWC3 G1				-9.11	28.19	4.06E-03	2.01
	Bracket (analyses 35-39,52-56): average and ±2SD				**-8.97 ± 1.43**			
Sample Mount Fram Strait PT4								
59	PT4 UWC3 G1				-8.70	27.64	3.42E-03	1.97
60	PT4 UWC3 G1				-8.90	27.68	3.25E-03	1.98
61	PT4 UWC3 G1				-8.82	28.00	3.07E-03	2.00
62	PT4 UWC3 G1				-9.24	28.13	3.11E-03	2.01
	average and ±2SD				**-8.91 ± 0.46**			
63	PT4 18a_01	31.68	0.90	0.75	10.18	26.55	1.74E-02	1.90
65	PT4 13b_01	31.68	0.90	0.75	10.19	26.81	1.82E-02	1.92
66	PT4 13b_02	31.14	0.90	0.22	9.66	26.92	1.76E-02	1.92
67	PT4 23b_01	30.55	0.90	-0.35	9.08	26.15	2.52E-02	1.87
68	PT4 23b_02	33.13	0.90	2.15	11.61	25.10	1.35E-02	1.79

69	PT4 23b_03	31.98	0.90	1.04	10.48	26.56	1.33E-02	1.90
70	PT4 8b_01	30.52	0.90	-0.38	9.05	26.71	1.20E-02	2.05
71	PT4 8b_02	31.36	0.90	0.44	9.88	26.77	1.33E-02	2.06
72	PT4 8b_03	31.08	0.90	0.17	9.60	25.91	1.96E-02	1.99
73	PT4 25b_01	30.37	0.90	-0.52	8.91	26.48	1.58E-02	2.04
74	PT4 UWC3 G1				-8.81	26.93	3.37E-03	2.07
75	PT4 UWC3 G1				-7.97	26.33	3.35E-03	2.03
76	PT4 UWC3 G1				-7.99	27.88	3.30E-03	1.99
77	PT4 UWC3 G1				-8.42	27.82	3.21E-03	1.99
	Bracket (analyses 59-62, 74-77): average and ±2SD				**-8.60 ± 0.90**			
78	PT4 23a_01	31.71	1.22	0.77	10.21	27.11	1.81E-02	1.94
79	PT4 23a_02	32.27	1.22	1.32	10.76	26.55	1.41E-02	1.90
80	PT4 UWC3 G1				-8.05	27.24	3.31E-03	1.95
81	PT4 UWC3 G1				-7.03	27.46	3.27E-03	1.96
82	PT4 UWC3 G1				-7.57	27.65	3.24E-03	1.98
83	PT4 UWC3 G1				-7.12	27.67	3.37E-03	1.98
	Bracket (analyses 74-77, 80-83): average and ±2SD				**-7.87 ± 1.22**			
164	PT4 UWC3 G1				-8.53	29.20	3.03E-03	1.95
165	PT4 UWC3 G1				-8.51	29.56	3.18E-03	1.97
166	PT4 UWC3 G1				-8.81	29.47	3.16E-03	1.96
167	PT4 UWC3 G1				-8.87	29.64	3.42E-03	1.98
	average and ±2SD				**-8.68 ± 0.37**			
168	PT4 2b_01	31.81	0.67	0.87	10.25	28.38	1.56E-02	1.89
169	PT4 2b_02	32.22	0.67	1.27	10.65	29.08	1.76E-02	1.94
171	PT4 4b_02	29.49	0.67	-1.38	7.97	28.19	1.56E-02	1.88
172	PT4 27b_01	31.54	0.67	0.61	9.99	28.07	1.62E-02	1.87
173	PT4 27b_02	31.93	0.67	0.99	10.37	28.49	1.41E-02	1.90
174	PT4 7b_01	31.35	0.67	0.43	9.80	28.01	1.57E-02	1.87

175	PT4 30b_01	31.22	0.67	0.30	9.67	28.27	1.61E-02	2.02
176	PT4 30b_02	30.14	0.67	-0.75	8.61	26.61	3.37E-02	1.90
178	PT4 15a_02	30.01	0.67	-0.87	8.49	28.24	1.93E-02	2.02
179	PT4 UWC3 G1				-9.06	29.52	3.25E-03	2.11
180	PT4 UWC3 G1				-8.17	28.75	3.16E-03	2.05
181	PT4 UWC3 G1				-8.33	28.83	3.64E-03	2.06
182	PT4 UWC3 G1				-9.07	28.91	3.02E-03	2.07
	Bracket (analyses 164-167, 179-182): average and ±2SD				**-8.24 ± 0.67**			
183	PT4 30a_01	30.71	0.83	-0.20	9.41	28.62	1.45E-02	2.04
184	PT4 31b_01	31.71	0.83	0.78	10.40	28.41	1.26E-02	2.03
185	PT4 31b_02	31.30	0.83	0.38	10.00	28.39	1.41E-02	2.03
186	PT4 18b_01	30.62	0.83	-0.28	9.33	27.07	1.55E-02	1.93
187	PT4 19b_01	30.79	0.83	-0.12	9.50	27.44	1.44E-02	1.96
188	PT4 19b_02	30.86	0.83	-0.05	9.56	27.19	1.47E-02	1.94
189	PT4 20c_01	32.67	0.83	1.71	11.34	26.97	1.50E-02	1.93
190	PT4 UWC3 G1				-8.32	28.16	2.77E-03	2.01
191	PT4 UWC3 G1				-8.08	28.31	2.84E-03	2.02
192	PT4 UWC3 G1				-8.01	27.71	2.86E-03	1.98
193	PT4 UWC3 G1				-8.36	28.06	3.46E-03	2.00
	Bracket (analyses 179-182, 190-193): average and ±2SD				**-8.19 ± 0.83**			
Sample Mount Fram Strait PT2								
196	PT2 UWC3 G2				-9.26	28.56	9.60E-03	2.04
197	PT2 UWC3 G2				-9.15	28.14	1.07E-02	2.01
198	PT2 UWC3 G2				-8.85	28.21	9.39E-03	2.01
199	PT2 UWC3 G2				-8.96	28.02	1.02E-02	2.00
	average and ±2SD				**-9.05 ± 0.36**			
200	PT2 32a_01	31.61	0.73	0.68	9.87	27.01	2.04E-02	1.93
201	PT2 32a_02	31.66	0.73	0.73	9.92	27.69	2.06E-02	1.98

202	PT2 32a_03	31.12	0.73	0.20	9.39	27.10	1.99E-02	1.94
203	PT2 28a_01	31.31	0.73	0.39	9.57	26.39	2.07E-02	1.89
204	PT2 28a_02	31.26	0.73	0.34	9.53	26.19	2.16E-02	1.87
205	PT2 31a_01	30.98	0.73	0.07	9.25	26.54	2.64E-02	1.90
206	PT2 31a_02	30.92	0.73	0.01	9.19	27.05	1.87E-02	1.93
207	PT2 31a_03	30.72	0.73	-0.18	9.00	25.57	2.56E-02	1.83
208	PT2 UWC3 G2				-8.66	27.47	9.45E-03	1.96
209	PT2 UWC3 G2				-8.97	28.10	9.19E-03	2.01
210	PT2 UWC3 G2				-8.06	27.55	9.18E-03	1.97
211	PT2 UWC3 G2				-8.90	27.73	9.16E-03	1.98
	Bracket (analyses 196-199, 208-211): average and ±2SD				**-8.8505 ± 0.73**			
Sample Mount Fram Strait PT2								
212	PT5 UWC3 G1				-8.84	27.49	4.40E-03	1.96
213	PT5 UWC3 G1				-8.78	27.86	4.24E-03	1.99
214	PT5 UWC3 G1				-9.07	27.65	4.34E-03	1.97
215	PT5 UWC3 G1				-9.10	28.21	4.13E-03	2.01
	average and ±2SD				**-8.95 ± 0.32**			
216	PT5 26b_01	30.18	0.69	-0.71	8.37	24.00	2.26E-02	1.71
217	PT5 26b_02	28.98	0.69	-1.87	7.20	26.12	2.77E-02	1.87
218	PT5 29b_01	32.06	0.69	1.12	10.21	26.52	1.67E-02	2.04
219	PT5 29b_02	31.81	0.69	0.88	9.97	26.23	1.84E-02	2.02
220	PT5 1c_01	31.17	0.69	0.25	9.34	23.38	2.44E-02	1.80
221	PT5 1c_02	29.85	0.69	-1.02	8.05	26.43	1.79E-02	2.03
222	PT5 1b_01	28.14	0.69	-2.69	6.37	26.70	1.33E-02	2.05
223	PT5 1b_02	27.91	0.69	-2.91	6.15	26.32	1.30E-02	2.02
224	PT5 1b_03	28.36	0.69	-2.47	6.59	26.62	1.36E-02	2.05
226	PT5 11a_02	32.12	0.69	1.17	10.26	24.99	1.80E-02	1.92
227	PT5 UWC3 G1				-8.66	26.84	3.68E-03	2.06
228	PT5 UWC3 G1				-8.62	26.64	3.86E-03	2.05

229	PT5 UWC3 G1				-8.81	27.85	3.68E-03	1.99
230	PT5 UWC3 G1				-9.69	28.31	3.78E-03	2.02
	Bracket (analyses 212-215, 227-230): average and ±2SD				**-8.95 ± 0.69**			
231	PT5 13c_01	30.21	0.78	-0.68	8.52	26.96	2.18E-02	1.93
232	PT5 20b_01	31.90	0.78	0.96	10.17	26.68	1.53E-02	1.91
233	PT5 16b_01	31.53	0.78	0.60	9.81	26.38	1.89E-02	1.88
234	PT5UWC3 G1				-8.72	28.22	3.59E-03	2.02
235	PT5UWC3 G1				-8.51	28.10	3.66E-03	2.01
236	PT5UWC3 G1				-8.53	27.93	3.85E-03	2.00
237	PT5UWC3 G1				-9.09	27.99	3.45E-03	2.00
	Bracket (analyses 227-230, 234-237): average and ±2SD				**-8.83 ± 0.78**			
Sample Mount Irminger Sea 1								
9	IRM UWC3 STD1				-7.18	32.76	1.66E-03	1.72
10	IRM UWC3 STD1				-6.69	32.95	1.95E-03	1.73
11	IRM UWC3 STD2				-8.05	32.84	1.61E-03	1.82
12	IRM UWC3 STD2				-7.24	32.54	1.84E-03	1.81
	average and ±2SD				**-7.29 ± 1.13**			
14	IRM14-02	32.60	0.96	1.64	12.29	30.67	1.03E-02	1.70
15	IRM14-03	32.77	0.96	1.80	12.45	30.48	1.16E-02	1.69
16	IRM14-04	32.74	0.96	1.77	12.42	30.56	1.14E-02	1.70
17	IRM14-05	33.29	0.96	2.31	12.97	31.88	1.09E-02	1.68
18	IRM14-06	32.62	0.96	1.66	12.31	32.79	1.03E-02	1.93
19	IRM14-07	32.94	0.96	1.97	12.63	30.16	1.01E-02	1.77
20	IRM14-08	33.22	0.96	2.24	12.90	28.92	1.13E-02	1.70
21	IRM UWC3 STD1				-7.28	30.16	1.90E-03	1.77
22	IRM UWC3 STD1				-8.10	29.99	2.12E-03	1.76
23	IRM UWC3 STD1				-7.66	31.30	2.04E-03	1.74

24	IRM UWC3 STD1				-7.21	32.98	2.13E-03	1.74
	Bracket (analyses 9-12, 21-24): average and ±2SD				**-7.43 ± 0.96**			
25	IRM15-01	33.14	0.73	2.17	12.77	33.21	1.04E-02	1.75
26	IRM15-02	32.89	0.73	1.92	12.52	31.22	1.08E-02	1.64
27	IRM15-03	32.96	0.73	1.98	12.58	31.61	9.75E-03	1.66
28	IRM15-04	33.05	0.73	2.08	12.68	31.67	9.65E-03	1.67
29	IRM15-05	33.18	0.73	2.20	12.80	30.38	9.23E-03	1.69
30	IRM8-01	32.73	0.73	1.77	12.36	30.39	1.17E-02	1.69
31	IRM8-02	34.23	0.73	3.23	13.84	30.86	1.07E-02	1.71
32	IRM8-03	32.64	0.73	1.68	12.28	30.25	1.18E-02	1.68
33	IRM8-04	33.65	0.73	2.65	13.26	30.14	9.16E-03	1.67
34	IRM8-05	33.45	0.73	2.46	13.06	29.82	9.12E-03	1.66
35	IRM UWC3 STD1				-7.32	31.50	2.12E-03	1.75
36	IRM UWC3 STD1				-6.96	33.40	1.98E-03	1.76
37	IRM UWC3 STD1				-7.80	33.58	1.91E-03	1.77
38	IRM UWC3 STD1				-7.51	32.21	2.16E-03	1.79
	Bracket (analyses 21-24, 35-38): average and ±2SD				**-7.48 ± 0.73**			
39	IRM8-06	32.55	0.48	1.59	12.28	33.76	1.16E-02	1.69
40	IRM1-01	32.47	0.48	1.51	12.21	34.53	1.27E-02	1.64
42	IRM1-03	33.28	0.48	2.30	13.00	34.53	1.51E-02	1.73
43	IRM1-04	33.11	0.48	2.14	12.84	33.47	8.40E-03	1.67
44	IRM1-05	32.63	0.48	1.66	12.36	33.87	9.91E-03	1.69
45	IRM10-01	32.84	0.48	1.87	12.57	33.73	9.80E-03	1.78
46	IRM10-02	33.20	0.48	2.22	12.92	33.48	9.25E-03	1.76
47	IRM10-03	32.79	0.48	1.82	12.52	33.23	9.61E-03	1.75
48	IRM10-04	33.39	0.48	2.41	13.11	31.96	9.46E-03	1.68
49	IRM10-05	32.74	0.48	1.77	12.47	32.34	9.48E-03	1.70
50	IRM UWC3 STD1				-7.47	33.46	1.75E-03	1.76

51	IRM UWC3 STD1				-7.38	33.59	1.86E-03	1.77
52	IRM UWC3 STD1				-7.39	33.16	1.84E-03	1.75
53	IRM UWC3 STD1				-7.25	33.78	1.89E-03	1.78
	Bracket (analyses 35-38,50-53): average and ±2SD				**-7.38 ± 0.48**			
54	IRM2-01	32.64	0.77	1.68	12.40	31.37	1.12E-02	1.65
55	IRM2-02	33.44	0.77	2.46	13.18	31.55	9.74E-03	1.66
56	IRM2-03	32.56	0.77	1.60	12.31	30.93	9.70E-03	1.63
58	IRM2-05	33.60	0.77	2.61	13.34	31.48	1.06E-02	1.66
59	IRM16-01	32.23	0.77	1.28	11.99	31.50	1.06E-02	1.75
60	IRM16-02	32.72	0.77	1.76	12.47	31.01	9.96E-03	1.72
61	IRM16-03	32.15	0.77	1.21	11.92	26.24	1.04E-02	1.75
62	IRM UWC3 STD1				-7.77	27.09	2.12E-03	1.81
63	IRM UWC3 STD1				-7.83	27.65	2.32E-03	1.73
64	IRM UWC3 STD1				-7.24	33.67	2.07E-03	1.68
65	IRM UWC3 STD1				-6.58	35.72	1.96E-03	1.70
	Bracket (analyses 50-53, 62-65): average and ±2SD				**-7.36 ± 0.77**			
66	IRM16-04;	32.98	0.85	2.01	12.67	34.32	1.11E-02	1.72
67	IRM9-01;	32.55	0.85	1.59	12.24	34.53	1.23E-02	1.73
68	IRM9-02;	31.97	0.85	1.03	11.68	34.54	9.66E-03	1.73
69	IRM9-03;	33.03	0.85	2.05	12.71	33.68	6.53E-03	1.68
70	IRM9-04;	32.54	0.85	1.58	12.23	32.72	1.02E-02	1.72
72	IRM18b-02;	33.01	0.85	2.03	12.69	31.56	1.46E-02	1.58
75	IRM UWC3 STD1				-7.80	33.40	1.94E-03	1.76
76	IRM UWC3 STD1				-7.35	33.00	2.09E-03	1.83
77	IRM UWC3 STD1				-7.59	29.20	2.18E-03	1.82
78	IRM UWC3 STD1				-7.21	30.42	2.28E-03	1.79
	Bracket (analyses 62-65, 75-78): average and ±2SD				**-7.42 ± 0.85**			

79	IRM18k-01	32.37	0.75	1.42	12.16	30.01	1.14E-02	1.77
80	IRM18k-02	32.15	0.75	1.20	11.94	28.63	1.25E-02	1.68
81	IRM6-01	32.62	0.75	1.66	12.41	28.80	1.12E-02	1.69
82	IRM6-02	33.34	0.75	2.36	13.12	29.11	1.01E-02	1.71
83	IRM6-03	33.20	0.75	2.22	12.98	30.19	1.07E-02	1.78
84	IRM6-04	32.58	0.75	1.62	12.36	30.54	9.22E-03	1.80
85	IRM6-05	32.44	0.75	1.48	12.23	29.90	1.03E-02	1.76
86	IRM4-01	33.35	0.75	2.37	13.12	28.94	1.19E-02	1.70
87	IRM4-02	33.18	0.75	2.21	12.96	28.30	1.17E-02	1.66
88	IRM4-03	32.72	0.75	1.75	12.50	32.01	9.39E-03	1.68
90	IRM UWC3 STD1				-7.69	34.50	1.82E-03	1.82
91	IRM UWC3 STD1				-6.71	33.62	2.09E-03	1.77
92	IRM UWC3 STD1				-7.34	33.51	2.19E-03	1.76
93	IRM UWC3 STD1				-6.94	33.75	2.19E-03	1.78
	Bracket (analyses 75-78, 90-93): average and ±2SD				**-7.33 ± 0.75**			
95	IRM UWC3 STD1				-7.38	33.77	1.99E-03	1.69
96	IRM UWC3 STD1				-7.02	33.65	1.91E-03	1.77
97	IRM UWC3 STD1				-7.07	33.54	1.93E-03	1.77
98	IRM UWC3 STD1				-7.43	33.23	1.88E-03	1.75
	average and ±2SD				**-7.23 ± 0.42**			
99	IRM7-01	31.77	0.37	0.83	11.65	32.26	1.04E-02	1.79
100	IRM7-02	31.83	0.37	0.89	11.71	32.02	1.16E-02	1.78
101	IRM7-03	32.34	0.37	1.39	12.22	32.77	7.85E-03	1.82
102	IRM7-04*	30.38	0.37	-0.51	10.30	31.17	1.10E-02	1.73
103	IRM7-05	31.92	0.37	0.98	11.80	31.86	1.07E-02	1.77
104	IRM19-01	31.80	0.37	0.86	11.68	31.26	1.01E-02	1.74
105	IRM19-02	32.96	0.37	1.99	12.82	30.72	1.23E-02	1.71
106	IRM19-03	32.51	0.37	1.55	12.38	29.95	8.57E-03	1.66
107	IRM19-04	30.90	0.37	-0.01	10.80	30.36	1.15E-02	1.69
108	IRM19-05	32.80	0.37	1.83	12.66	30.80	8.03E-03	1.71

109	IRM19-06	32.28	0.37	1.32	12.15	30.01	1.07E-02	1.67
110	IRM UWC3 STD1				-7.35	31.28	2.15E-03	1.74
111	IRM UWC3 STD1				-7.46	33.77	2.01E-03	1.78
112	IRM UWC3 STD1				-7.03	33.80	1.99E-03	1.88
113	IRM UWC3 STD1				-7.26	30.70	2.12E-03	1.81
	Bracket (analyses 95-98, 110-113): average and ±2SD				**-7.25 ± 0.37**			
115	IRM18e-02	32.09	0.52	1.15	11.87	27.12	2.26E-02	1.51
116	IRM18e-03	32.88	0.52	1.91	12.64	30.45	7.83E-03	1.69
117	IRM5-01	32.47	0.52	1.51	12.24	30.45	9.92E-03	1.69
118	IRM5-02	31.04	0.52	0.12	10.83	30.33	1.41E-02	1.69
119	IRM5-03	32.96	0.52	1.99	12.72	30.26	1.07E-02	1.68
120	IRM5-04	32.74	0.52	1.77	12.50	30.01	1.07E-02	1.67
121	IRM5-05	33.67	0.52	2.68	13.42	28.63	1.10E-02	1.59
122	IRM17-01	33.09	0.52	2.11	12.84	29.51	1.22E-02	1.74
123	IRM17-02	33.17	0.52	2.19	12.92	30.11	1.03E-02	1.77
124	IRM17-03	32.98	0.52	2.01	12.73	28.93	9.77E-03	1.70
125	IRM UWC3 STD1				-7.28	30.90	1.99E-03	1.82
126	IRM UWC3 STD1				-7.90	31.89	2.06E-03	1.77
127	IRM UWC3 STD1				-7.13	32.81	1.99E-03	1.73
128	IRM UWC3 STD1				-7.40	33.16	1.91E-03	1.75
	Bracket (analyses 110-113, 125-128): average and ±2SD				**-7.35 ± 0.52**			
129	IRM17-04	32.65	0.48	1.69	12.31	30.88	1.12E-02	1.63
130	IRM17-05	32.53	0.48	1.57	12.19	31.39	1.15E-02	1.65
131	IRM17-06	33.10	0.48	2.12	12.75	31.56	1.02E-02	1.66
132	IRM13-01	32.88	0.48	1.91	12.54	30.20	1.10E-02	1.68
133	IRM13-02	32.71	0.48	1.75	12.37	30.62	8.93E-03	1.70
134	IRM13-03	32.14	0.48	1.20	11.82	30.47	1.15E-02	1.69
135	IRM13-04	32.67	0.48	1.71	12.33	31.46	9.70E-03	1.75

136	IRM13-04-5	32.23	0.48	1.28	11.90	30.00	1.07E-02	1.67
137	IRM UWC3 STD1				-7.26	32.20	1.97E-03	1.79
138	IRM UWC3 STD1				-7.55	31.90	1.91E-03	1.77
140	IRM UWC3 STD1				-7.59	31.96	2.22E-03	1.78
141	IRM UWC3 STD1				-7.51	32.24	1.78E-03	1.79
	Bracket (analyses 125-128, 137-141): average and ±2SD				**-7.45 ± 0.48**			

[a] Oxygen isotope ratios in PDB scale, converted by the equation of Coplen et al., 1983

[b] ±2 SD of the bracketing standard analyses

[c] Oxygen isotope ratios in SMOW scale, corrected for instrumental bias. The UWC-3 calcite standard has a calibrated $\delta^{18}O$ of 12.49 ‰ VSMOW [Kozdon et al., 2009]

[d] Raw measured ($^{18}O/^{16}O$) ratios, converted to the delta notation by normalizing to Standard Mean Ocean Water ($^{18}O/^{16}O$) SMOW = 0.00200520

[e] Secondary ion intensity of ^{16}O- ions in gigacounts per second (Gcps)

[f] Background - corrected $^{16}OH/^{16}O$ - ratios that may provide an indication of water, organic matter content, and/or other H-bearing phases in the SIMS pit [Wycech et al., 2018].

Table S3. Summary of Mg/Ca (mmol/mol) results collected on the F and F-1 chambers of plankton-tow collected *N. pachyderma* from the Fram Strait with the CTD measured temperatures averaged for the depths of the tows. Shading denotes all profiles from single shells. (*) - only one profile was generated on the shell. This value is presented rather than an average.

Sample	Fragment	Laser pit	Mg/Ca (mmol/mol)	Shell average Mg/Ca (mmol/mol)	2SD	Measured temperature (°C)
PT1	a	1	2.57			
	a	2	2.12			
	c	1	1.82	2.17	0.62	2.7
PT2	a	1	0.98			
	b	1	1.16	1.07	1.32	2.7
PT3	a	1	3.64			
	a	2	4.04	3.84	0.57	3.0
PT4	a	1	1.59			
	a	2	2.04			
	b	1	1.71	1.78	0.47	3.0
PT2S	a	1	1.58	1.58*	-	1.6
PT5b	b	1	3.36	3.36*	-	3.7
PT6a	a	1	4.03	4.03*	-	3.7

PT7	a	1	7.13			
	b	1	2.07	4.60	4.38	3.2
PT8	a	1	2.72			
	b	1	2.11	2.42	0.73	3.2
PT9	a	1	1.59			
	a	2	2.80	2.19	1.70	1.4
PT10	a	1	2.06	2.06*	-	1.4
PT11	a	1	2.26	2.26*	-	3.1
PT11S	a	1	1.73			
	a	2	2.50			
	b	1	3.60			
	c	1	4.02	2.96	2.08	-0.3
PT12S	a	1	5.34			
	b	1	4.61			
	c	1	1.79	3.91	1.35	-0.3
PT13	a	1	1.54			
	b	1	0.43			
	c	1	0.64	0.87	1.17	0.3
PT14	a	1	1.22	1.22*	-	0.3
PT15	a	1	1.92	1.92*	-	2.2
PT16	a	1	2.12			
	b	1	1.79	1.95	0.33	2.2
PT15S	a	1	1.43			0.3
	b	1	1.43	1.43	0.0	0.3
PT17	a	1	2.59			
	a	2	2.12			
	b	1	2.80			
	b	2	2.83	2.58	0.66	3.8
PT18	a	1	2.76			
	b	1	2.29	2.52	0.59	3.8
PT19	b	1	2.92	2.92*	-	3.7
PT20	a	1	2.23			
	a	2	3.14			
	c	1	1.41	2.52	1.56	3.7
PT20S	a	1	2.37			
	b	1	1.01			
	c	1	0.87			
	d	1	0.68	1.23	1.54	1.2
PT21	a	1	2.89	2.89*	-	1.3
PT22	a	1	1.60			
	a	2	2.12			
	b	1	3.35	2.62	1.56	1.3
PT23	a	1	4.52			
	b	1	5.03	4.77	0.72	2.0
PT24	a	1	2.92	2.92*	-	2.0
PT25S	b	1	0.58	0.58*	-	-0.5
PT26S	a	1	2.94	2.94*	-	-0.5
PT25	a	1	1.70	1.70*	-	-1.8
PT26	a	1	1.44			
	b	1	2.09	1.76	0.65	-1.8
PT27	a	1	1.96			

	b	1	2.26	2.11	0.42	-1.5
PT28	a	1	1.08	2.08*	-	-1.5
PT30S	a	1	2.39			
	a	2	3.07	2.73	0.96	-1.6
PT31S	a	1	1.47			
	a	2	5.47	1.47	0.71	-1.6
PT29	a	1	2.81			
	b	1	2.76	2.78	0.08	-1.6
PT30	a	1	1.04			
	b	1	2.09			
	b	2	1.71	1.61	1.49	-1.6
PT31	a	1	1.33			
	b	1	1.32			
	b	2	0.60	1.08	0.83	-0.8
PT32	a	1	2.93			
	a	2	3.26			
	b	1	2.14	2.78	1.15	-0.8
PT35S	a	1	0.61			
	a	2	1.73			
	b	1	1.11	1.1.5	1.12	-1.6

Table S4. Summary of average Mg/Ca (mmol/mol) results collected on the F and F-1 chambers of sediment trap collected *N. pachyderma* from the Irminger Sea.

Sample	Laser pit	Mg/Ca (mmol/mol)	Shell average Mg/Ca (mmol/mol)	2SD
I1	a	1.14		
	b	0.99	1.07	0.22
I2	a	0.95		
	b	1.12	1.04	0.24
I3	a	1.60		
	b	1.13	1.36	0.67
I4	a	1.01		
	b	0.83	0.92	0.27
I5	a	1.40		
	b	1.73	1.57	0.47
I6	a	1.05		
	b	0.91	0.98	0.20
I7	a	1.03		
	b	1.14	1.08	0.17
I8	a	0.82		
	b	1.14	0.98	0.45
I9	a	1.56		
	b	1.33	1.44	0.33
I10	a	0.82		
	b	0.70	0.76	0.17
I11	a	0.76	0.76*	-

I12	a	1.31		
	b	1.21	1.26	0.14
I13	a	1.35		
	b	0.98	1.16	0.53
I14	a	1.16		
	b	1.39	1.27	0.34
I15	a	1.15		
	b	1.12	1.13	0.04
I16	a	1.09		
	b	0.98	1.03	0.15
I17	a	1.38		
	b	1.49	1.44	0.16
I18_1	a	1.68		
	b	1.23		
I18_2	a	1.95		
	b	1.15		
	c	1.22		
I18_3	a	1.55		
	b	1.50		
I18_4	a	1.19		
	b	1.22		
I18_5	a	1.56		
	b	1.68	1.40	0.54
I19	a	1.45		
	b	1.10	1.27	0.50
I20	a	1.08		
	b	1.05	1.06	0.04

Table S5. Summary of $\delta^{18}O_{calcite}$ (‰ VPDB) results collected on the SIMS at the wiscSIMS lab at the University of Wisconsin, Madison on sediment trap collected *N. pachyderma* from the Irminger Sea. Shaded groups identify SIMS spots from the same specimen.

Specimen	**SIMS spot**	**Type of calcite**	**$\delta^{18}O_{calcite}$ (‰ VPDB)**	**±2SD (external)**	**average shell $\delta^{18}O_{calcite}$ (‰ VPDB +/- 2SE)**
1	1	lamellar	1.51	0.48	
1	3	lamellar	2.30	0.48	
1	4	crust	2.14	0.48	
1	5	crust	1.66	0.48	1.9 +/- 0.37
2	1	lamellar	1.87	0.48	
2	2	crust	2.22	0.48	
2	3	crust	1.82	0.48	
2	4	lamellar	2.41	0.48	
2	5	lamellar	1.77	0.48	2.02 +/- 0.25
4	1	lamellar	2.37	0.75	

4	2	lamellar	2.21	0.75	
4	3	crust	1.75	0.75	2.11 +/- 0.37
5	1	lamellar	1.51	0.52	
5	2	crust	0.12	0.52	
5	3	crust	1.99	0.52	
5	4	lamellar	1.77	0.52	
5	5	crust	2.68	0.52	1.62 +/- 0.84
6	1	lamellar	1.66	0.75	
6	2	crust	2.36	0.75	
6	3	crust	2.22	0.75	
6	4	crust	1.62	0.75	
6	5	lamellar	1.48	0.75	1.87 +/- 0.35
7	1	lamellar	0.83	0.37	
7	2	crust	0.89	0.37	
7	3	crust	1.39	0.37	
7	4	lamellar	-0.51	0.37	
7	5	lamellar	0.98	0.37	1.02 +/- 0.23
8	2	lamellar	1.64	0.96	
8	3	lamellar	1.80	0.96	
8	4	crust	1.77	0.96	
8	5	crust	2.31	0.96	
8	6	crust	1.66	0.96	
8	7	crust	1.97	0.96	
8	8	lamellar	2.24	0.96	1.91 +/- 0.20
9	1	lamellar	2.17	0.73	
9	2	lamellar	1.92	0.73	
9	3	crust	1.98	0.73	
9	4	crust	2.08	0.73	
9	5	crust	2.20	0.73	2.07 +/- 0.10
10	1	lamellar	1.77	0.73	
10	2	crust	3.23	0.73	
10	3	crust	1.68	0.73	
10	4	crust	2.65	0.73	
10	5	crust	2.46	0.73	
10	6	lamellar	1.59	0.73	2.23 +/- 0.54
13	1	lamellar	1.91	0.48	
13	2	crust	1.75	0.48	
13	3	lamellar	1.20	0.48	
13	4	crust	1.71	0.48	

13	5	lamellar	1.28	0.48	1.57 +/- 0.28
14	1	lamellar	1.68	0.77	
14	2	crust	2.46	0.77	
14	3	crust	1.60	0.77	
14	5	lamellar	2.61	0.77	2.09 +/- 0.52
15	1	crust	1.59	0.85	
15	2	crust	1.03	0.85	
15	3	crust	2.05	0.85	
15	4	lamellar	1.58	0.85	1.56 +/- 0.42
16	1	lamellar	1.28	0.77	
16	2	crust	1.76	0.77	
16	3	lamellar	1.21	0.77	
16	4	crust	2.01	0.77	1.56 +/- 0.39
17	1	lamellar	2.11	0.52	
17	2	crust	2.19	0.52	
17	3	crust	2.01	0.52	
17	4	lamellar	1.69	0.48	
17	5	lamellar	1.57	0.48	
17	6	crust	2.12	0.48	1.95 +/- 0.21
18	b_2	lamellar	2.03	0.85	
18	e_2	lamellar	1.15	0.52	
18	e_3	crust	1.91	0.52	
18	k_1	crust	1.42	0.75	
18	k_2	crust	1.20	0.75	1.54 +/- 0.36
19	1	lamellar	0.86	0.37	
19	2	crust	1.99	0.37	
19	3	crust	1.55	0.37	
19	4	crust	-0.01	0.37	
19	5	crust	1.83	0.37	
19	6	lamellar	1.32	0.37	1.26 +/- 0.60

Table S6. Summary of $\delta^{18}O_{calcite\text{-}water}$ (‰ VPDB) results collected on the SIMS at the WiscSIMS lab at the University of Wisconsin, Madison on plankton tow collected *N. pachyderma* from the Fram Strait. Shaded groups identify SIMS spots from the same specimen. Complete sample list and station information are outlined in Table S1.

Specimen	Fragment	SIMS spot	Station	Collection depth (m)	$\delta^{18}O_{calcite}$ (‰ VPDB)	±2SD (external)	average shell $\delta^{18}O_{calcite}$ (‰ VPDB +/- 2SE)
1	a	1	77	50-100	0.23	1.21	
1	a	2	77	50-100	-1	1.21	
1	a	3	77	50-100	0.78	1.21	
1	a	4	77	50-100	0	1.21	
1	c	2	77	50-100	-1.02	0.69	
1	b	1	77	50-100	-2.69	0.69	-0.62 +/- 1.01
2	a	1	77	50-100	0.22	1.21	
2	a	2	77	50-100	-1.3	1.21	
2	a	3	77	50-100	-1.37	1.21	
2	b	1	77	50-100	0.87	0.67	
2	b	2	77	50-100	1.27	0.67	-0.06 +/- 1.09
3	a	1	77	100-200	-1.37	0.65	
3	a	2	77	100-200	0.19	0.65	
3	a	3	77	100-200	0.27	0.65	-0.30 +/- 1.07
4	b	2	77	100-200	-1.38	0.67	-1.38
5	b	2	78	50-100	-0.6	1.43	-0.6
7	a	1	78	100-200	0.27	1.43	
7	a	2	78	100-200	-0.57	1.43	
7	b	1	78	100-200	0.43	0.67	0.04 +/- 0.62
8	a	1	78	100-200	0.93	1.21	
8	a	2	78	100-200	-0.2	1.21	
8	a	3	78	100-200	-0.57	1.21	
8	b	1	78	100-200	-0.38	0.9	
8	b	2	78	100-200	0.44	0.9	
8	b	3	78	100-200	0.17	0.9	0.07 +/- 0.46
11	a	2	79	100-200	1.17	0.69	1.17
13	b	1	80	50-100	0.75	0.9	
13	b	2	80	50-100	0.22	0.9	
13	c	1	80	50-100	-0.68	0.78	0.1 +/- 0.83
14	a	1	80	50-100	0.84	1.43	
14	a	2	80	50-100	2.21	1.43	
14	a	3	80	50-100	2.39	1.43	1.81 +/-0.98
15	a	2	80	100-200	-0.87	0.67	-0.87
16	a	16a_02	80	100-200	-0.67	0.65	
16	a	16a_03	80	100-200	0.28	0.65	
16	b	16b_01	80	100-200	0.6	0.78	0.07 +/- 0.76
17	b	1	81	50-100	-1.91	0.65	

17	b	2	81	50-100	0.61	0.65	-0.65 +/- 2.53
18	a	1	81	50-100	0.75	0.9	
18	b	1	81	50-100	-0.28	0.83	0.23 +/- 1.03
19	a	1	81	100-200	0.58	1.43	
19	a	2	81	100-200	1.42	1.43	
19	b	1	81	100-200	-0.12	0.83	
19	b	2	81	100-200	-0.05	0.83	0.46 +/- 0.72
20	a	1	81	100-200	0.56	1.43	
20	a	2	81	100-200	0.72	1.43	
20	a	3	81	100-200	1.23	1.43	
20	c	1	81	100-200	1.71	0.83	
20	b	1	81	100-200	0.96	0.78	1.03 +/- 0.41
23	b	1	82	100-200	-0.35	0.9	
23	b	2	82	100-200	2.15	0.9	
23	b	3	82	100-200	1.04	0.9	
23	a	1	82	100-200	0.77	1.22	
23	a	2	82	100-200	1.32	1.22	0.99 +/- 0.81
25	b	1	83	50-100	-0.52	0.9	-0.52
26	b	1	83	50-100	-0.71	0.69	
26	b	2	83	50-100	-1.87	0.69	-1.29 +/- 0.84
27	b	1	83	100-200	0.61	0.67	
27	b	2	83	100-200	0.99	0.67	0.8 +/- 0.38
28	a	1	83	100-200	0.39	0.73	
28	a	2	83	100-200	0.34	0.73	0.36 +/- 0.04
29	b	1	84	50-100	1.12	0.69	
29	b	2	84	50-100	0.88	0.69	1.0 +/- 0.24
30	a	1	84	50-100	-0.2	0.83	
30	b	1	84	50-100	0.3	0.67	
30	b	2	84	50-100	-0.75	0.67	-0.22 +/- 0.61
31	a	1	84	100-200	0.07	0.73	
31	a	2	84	100-200	0.01	0.73	
31	a	3	84	100-200	-0.18	0.73	
31	b	1	84	100-200	0.78	0.83	
31	b	2	84	100-200	0.38	0.83	0.21 +/- 0.34
32	a	1	84	100-200	0.68	0.73	
32	a	2	84	100-200	0.73	0.73	
32	a	3	84	100-200	0.2	0.73	0.54 +/- 0.33

Ch. 2: Trace element patterns through cultured lamellar and crust calcite of non-spinose planktic foraminifera

Caitlin M. Livsey[1], Catherine V. Davis[2,3], Jennifer S. Fehrenbacher[4], Claudia Benitez-Nelson[2], Tessa M. Hill[1]

[1]*Department of Earth and Planetary Sciences, University of California Davis, Davis, CA 95616, USA.*

[2]*Department of Earth Ocean and Environment, University of South Carolina, Columbia, SC 29208, USA.*

[3]*Department of Marine, Earth, and Atmospheric Sciences, North Carolina State University, Raleigh, NC 27695, USA*

[4]*College of Earth, Ocean, and Atmospheric Sciences, Oregon State University, Corvallis, OR 97331, USA.*

Abstract

The calcification of many species of planktic foraminifera is complicated by the production of two distinct layers of calcite- the inner lamellar calcite (LC), and an outer crust. The crust calcite is distinctive from the LC in both texture and composition. Here we present intrashell trace element (TE)/Ca data from *Neogloboquadrina pachyderma* shells that were grown and subsequently produced a crust in culture at various temperatures. We observe marked changes in the B/Ca, Mg/Ca, Ba/Ca, Zn/Ca, Al/Ca, and Mn/Ca between the LC and crust calcites grown with no associated changes in either the environmental conditions or the trace element concentrations of the seawater. The measured $TE/Ca_{calcite}$ results were compared to the temperature and $[TE]_{sw}$, to better understand the relationships between the crust and LC geochemistry, and the environment in which the shells calcified. Our results demonstrate that the Mg/Ca in the LC agrees with the calibration relationship previously described in Livsey et al. (2020), while our study reveals that Mg/Ca in the crust calcite is not primarily controlled by temperature. Though these results cannot definitively resolve what is controlling the transition in geochemistry between the LC and crust, they do reveal that neither changes in the environmental conditions, $[Te]_{sw}$, nor a change in the calcification rate are the dominant factors. Discerning the geochemical changes that occur between the lamellar and crust calcites will inform studies utilizing fossil foraminifera to better understand past temperature, salinity, and meltwater influences.

Introduction

Paleoceanography relies heavily on microfossils and their geochemistry to understand past oceanographic conditions and how they have changed throughout geologic history. Planktic foraminifera are commonly used in paleoceanographic studies due to their high abundance in

oceanic sediments globally (Kucera, 2007). Many trace elements in seawater become incorporated into the foraminiferal calcium carbonate lattice (TE/Ca) in a predictable manner in response to environmental parameters (e.g., Brown and Elderfield, 1996; Katz et al., 2010; Sadekov et al., 2010; Hönisch et al., 2013; Jonkers et al., 2013; Regenberg et al., 2014; Fehrenbacher et al., 2018; Schiebel et al., 2018). Understanding the empirical relationship between foraminiferal geochemistry and the environment in which they calcified allows specific TE/Ca ratios to be utilized as paleoceanographic proxies for environmental conditions.

With the expansion of high-resolution analytical techniques utilizing individual foraminifera and increasingly small sample sizes, geochemical proxies are being implemented to reconstruct many different environmental parameters. The most widely utilized trace element proxy in planktic foraminifera shells is the ratio of magnesium to calcium (Mg/Ca), which has been linked to changes in temperature (e.g., Nürnberg, 1995; Nürnberg et al., 1995; Lea et al., 1999; Elderfield and Ganssen, 2000; Russell et al., 2004; Eggins et al., 2004; Sadekov et al., 2008; Friedrich et al., 2012). Further, Ba/Ca has been used to calculate salinity in regions where freshwater/riverine flux is the dominant control on the hydrography (Hall and Chan, 2004; Weldeab et al., 2007, 2014; Bergami et al., 2008; Hönisch et al., 2011; Evans et al., 2015; Vetter et al., 2017), and Mn/Ca was recently established as an upwelling indicator (e.g., Davis et al., 2020). Additionally, Zn/Ca has been proposed as a proxy for dissolved silica in seawater (e.g., Katz et al., 2010) and alternatively used to reconstruct the deep ocean carbonate saturation state (Marchitto et al., 2005). Finally, B/Ca has been shown to correlate with the pH of seawater (e.g., Yu and Elderfield, 2007). While geochemical proxies in foraminifera rely on empirical relationships between the environmental parameters and the geochemistry, not all of the geochemical variability in foraminifera shells is fully understood.

Foraminifera do not calcify their shells in chemical equilibrium with seawater due to offsets caused by biological/physiological factors, typically referred to as "vital effects" (e.g., Urey et al., 1951; Weiner and Dove, 2003). Many of the geochemical offsets have linked to photosymbiotic activity (Spero et al., 1987; Spero and Lea, 1996), ontogenetic growth (Berger, 1978; Lohmann et al., 1990; Uhle et al., 1997; Ezard et al., 2015), carbonate ion concentration (Lea and Spero, 1994; Spero et al., 1997; Bemis et al., 1998; Russell and Spero, 2000; Bijma et al., 2002; Holland et al., 2017), depth migration through ontogeny (Bemis et al., 2002), differences between morphotypes or ecophenotypes (Boyle, 1995; Kucera and Darling, 2002; Numberger et al., 2009; Morard et al., 2016; Sadekov et al., 2016), and addition of gametogenic calcite (Duplessy et al., 1981; Spero and Lea, 1996). However, there remain offsets from equilibrium whose sources have yet to be determined. For example, high-resolution analytical tools reveal that the distribution of trace elements in planktonic foraminiferal shells demonstrate large variations both within single shells and between individuals in the same population (Elderfield et al., 2002; Erez, 2003; Sadekov et al., 2005; Hathorne et al., 2009; Marr et al., 2013; Branson et al., 2015; Jonkers et al., 2016; Fehrenbacher et al., 2017; Hori et al., 2018; Livsey et al., 2020). While current calibrations work when using large sample sizes and bulk analyses (Spero et al., 2015), better understanding the sources and controls of geochemical variability in planktic foraminifera is critical to interpreting geochemical proxies from individual shells and improving the accuracy of reconstructions.

Identifying what is controlling the intra-shell geochemical variability can also provide additional insights into the conditions in which the foraminifera calcified. Interpreting the total range of geochemistry from a given population of individual foraminifera analyses (IFA) can be used to identify deviations from mean-state conditions (Groeneveld et al., 2019). At least some species of planktic foraminifera have a lifespan of ~1 month, after which their shells sink to the

seafloor and accumulate in the sediments (Spero, 1998). Therefore, the geochemistry within an individual foraminifera shell can represent conditions at a weekly or monthly resolution and can provide insights on the range in environmental conditions that a given site experiences. However, it is necessary to understand controls on foraminiferal calcite formation in order to produce robust interpretations.

Planktic foraminifera crust formation

Numerous species of non-spinose planktic foraminifera calcify their shells in two stages- first growing their inner, chamber-forming, lamellar calcite (LC), and subsequently adding a thick calcite crust before completing their lifecycles (Bé and Ericson, 1963; Hemleben et al., 1985; Carstens and Wefer, 1992; Lohmann, 1995; Kohfeld et al., 1996; Steinhardt et al., 2015). Species that have been observed forming a crust as part of their lifecycle include *Globorotalia hirsuta*, *Globorotalia inflata, Globorotalia menardii, Globorotalia scitula, Globorotalia tumida, Neogloboquadrina dutertrei, Neogloboquadrina incompta,* and *Neogloboquadrina pachyderma*. Distinct from gametogenic calcite, crust calcite is not linked to reproduction, and is characterized by blocky euhedral calcite crystals, low porosity, and a thicker shell (Bé and Ericson, 1963; Hemleben et al., 1985; Hathorne et al., 2009; Steinhardt et al., 2015). Previous high-resolution geochemical analyses on crusted species of planktic foraminifera document changes in both trace elements and stable isotopes between the LC and crust calcite (Lohmann, 1995; Nürnberg, 1995; Nürnberg et al., 1996; Sadekov et al., 2005; Hendry et al., 2009; Kozdon et al., 2009; Bolton and Marr, 2013; Jonkers et al., 2016; Vázquez Riveiros et al., 2016; Livsey et al., 2020). While the formation of a crust was originally believed to be linked to migration to deeper depths near the end of the lifecycle (Bauch et al., 1997; Lončarić et al., 2006; Mortyn

and Charles, 2003), crusting has been observed in individuals collected in surface waters (Jonkers et al., 2021), isothermal water columns (Jonkers et al., 2016), and those grown in culture at constant conditions (Davis et al., 2017). Provoking the migration to deeper depths may be the ecological reason for crust formation (by increasing the density of the shells), but the exact biogenic calcifying mechanisms of crust formation remain unknown. As non-spinose and deeper dwelling species typically inhabit higher latitudes and cooler waters, their shells are important proxies for the high-latitude climate system. Therefore, understanding what crust calcite represents in terms of environmental or physiological changes is critical to expanding paleo-reconstructions to high latitude waters.

Understanding how the high-latitudes respond to climate changes in the past is urgently important because the poles are currently experiencing temperatures increasing twice as fast as regions at lower latitudes. The acceleration of warming, termed polar amplification, is primarily driven by positive feedback processes as a result of the loss of Arctic ice cover (Serreze et al., 2009). The resulting changes in air and surface water temperatures are projected to have impacts on global climate. Paleoclimate reconstructions from this region are critically needed to understand the contribution and global implications of cold, dense water circulating into the North Atlantic (e.g. Serreze et al., 2000; Venegas and Mysak, 2000; Johannessen et al., 2004). *Neogloboquadrina pachyderma* is a species of planktic foraminifera that dominates high-latitude assemblages (>90% of assemblages) and is the principal species used for polar paleoceanography (e.g., Reynolds and Thunell, 1986; Bauch et al., 1997; Hendry et al., 2009; Pados et al., 2014). Previous studies using fossil *N. pachyderma* have measured bulk whole shells for Mg/Ca, therefore combining both the crust and LC signatures (i.e. Kohfeld et al., 1996; Mulitza et al., 2003; Kozdon et al., 2009). A Mg/Ca:temperature calibration for entire shells may not produce temperatures that reflect the

calcification environment *N. pachyderma* inhabited, since the degree of encrustation varies between individuals (Bé and Ericson, 1963; Orr, 1967; Hemleben et al., 1985). To accurately use *N. pachyderma* to reconstruct past conditions, it is necessary to quantify the geochemical proxy calibrations for the LC and crust calcite independently.

The impact of crust formation on $\delta^{18}O$ incorporation was revealed by secondary ion mass spectrometry (SIMS) $\delta^{18}O$ analyses on modern *N. pachyderma* shells that grew in iso-thermal/haline seawater. Domain-specific results reveal constant $\delta^{18}O$ through the LC and crust, indicating that hydrology ($\delta^{18}O_{sw}$ and temperature) is the primary control on $\delta^{18}O$ in all portions of *N. pachyderma* calcite (Livsey et al., 2020). In contrast, LA-ICPMS Mg/Ca results on the same shells demonstrate significant differences between the LC and crust (Jonkers et al., 2016,) revealing that there is an additional mechanism that impacts trace element incorporation between the LC and crust that does not similarly impact the $\delta^{18}O$.

Calibrating geochemical proxies

The calibrations of calcite geochemistry to hydrographic properties are relatively well constrained in a suite a species abundant in shallow tropical/temperate environments, but fewer studies have focused on the high latitudes and species that inhabit deeper waters, and specifically species that form a crust during their lifecycles. Crust-forming species occupy integral habitats in the ocean, and therefore their inclusion in paleoceanographic studies is fundamental to fully understand past oceans. Here we explore TE/Ca patterns within the LC and crust calcite of *N. pachyderma* that were grown in a controlled laboratory environment. Our results reveal that *N. pachyderma* crust calcite contains lower and more homogenous B/Ca, Al/Ca, Mg/Ca, Ba/Ca, Mn/Ca, and Zn/Ca compared to the LC with no change in the environmental conditions. Notably,

crust and LC Sr/Ca are not statistically different, demonstrating that the mechanism regulating the alteration of TE/Ca in the crust does not affect Sr/Ca. Further, these results reveal that the concentrations of TE/Ca in ocean-grown calcite demonstrate large variability when compared to both LC and crust TE/Ca. Finally, the Mg/Ca of *N. pachyderma* grown at three different culture temperatures indicate that 1) Mg/Ca of the LC agree with previous LC-only Mg/Ca relationships (Livsey et al., 2020), and further extends the temperature range at which it can be utilized, 2) the crust Mg/Ca is not primarily driven by temperature, and therefore should not be used in temperature reconstructions, and 3) bulk analyses that combine both crust and LC cannot be used to reconstruct seawater temperatures since the two domains of calcite do not incorporate Mg with the same sensitivity to temperature.

Methods

Live collection of foraminifera

Plankton tows were deployed during the summer (July-August) of 2019 near the shelf break off of Bodega Bay, CA (38º26'20", -123º27'01"). Samples were obtained on a total of six collection days spanning ~30 days across the study period in the same approximate location. Samples were collected from between 0-100 m depth using a 150-μm mesh net. Material collected in the tow was gently rinsed from the net into plastic Nalgene© bottles, and then stored in the dark (at near surface water temperatures ~12 ºC) while being transported to the Bodega Marine Laboratory. Upon return to the laboratory, individual foraminifera were picked from the plankton tow material based on suitability for culture, assessed by the presence of colored cytoplasm and absence of obvious crust formation. Selected specimens were rinsed twice in 0.6-μm filtered seawater, transferred via pipette into individual 75 mL polystyrene Falcon© flasks of filtered

seawater, and allowed to recover for ~12 hours at treatment temperature. Recovery of foraminifera was indicated by the extension of a rhizopodial network and visible movement or streaming of rhizopodia.

Specimens that recovered were transferred into filtered seawater that had been labeled with an aliquot of a concentrated single-spike solution. These solutions were prepared by adding a concentrated chemical "spike" to a volume of filtered seawater to achieve an elemental enrichment that labels the calcite grown in the culture conditions. Individual Falcon© flasks containing a single foraminifer were held at constant temperature (±0.15°C) in recirculating baths under full-spectrum CREE XP-E 72-Watt LED reef lights on a 12-hour light-dark cycle (55 $\pm$15 μmol photons/m^2s^2. Specimens were photographed, measured, and observed daily to track the health and growth of each individual. Every other day, healthy specimens (determined by color of cytoplasm and presence of rhizopodia) were fed a 1 day old, freeze-killed Artemia nauplius until gametogenesis or death. Any treatment water displaced during feeding was refreshed from a reservoir of the same batch of seawater in which the foraminifera was originally placed to prevent any variability in the elemental composition of treatment water. After completion of their life cycle, specimens were rinsed in deionized water and archived for subsequent analyses.

Experimental seawater spiking and sampling

All filtered seawater used for experiments contained an ^{86}Sr spike to increase the $^{86}Sr/^{88}Sr$ ratio of the seawater by 2x natural abundance (0.7395 mg/L) in order to distinguish between calcite grown in the laboratory conditions and ocean-grown calcite. Further, in addition to the ^{86}Sr spike, treatments of enriched Ba and Mn seawater were generated. Prior to use in experiments, the salinity and pH of the filtered seawater were measured by Sonde to ensure ambient ocean conditions

(salinity: 33.5-33.58 psu, pH: 7.74-8.1). For each batch of filtered and labeled seawater, aliquots of seawater were filtered at 0.2 μm, acidified by the addition of nitric acid, and stored for following analyses. Elemental analysis of seawater samples were carried out at Yale University, where all samples were diluted 50x in a 1 ppb In solution and analyzed on an Thermo Element 2. Counts were blank corrected, normalized to In, and converted to concentration using regressions from multiple dilutions of a multi-element standard solution.

Sample cleaning and preparation for geochemical analyses

Daily photographs and observation notes for each foraminifer were used to determine which specimens: (1) grew new chamber(s), (2) produced crust calcite, (3) produced gametogenic calcite, (4) lived more than 5 days in culture, and (5) did not obviously grow in culture. Crusting and thickening was assessed using images taken daily at 10x magnification and subsequent measurements of shell growth obtained using the ImageJ software. Evidence of gametogenesis was noted in daily observations by a paling of the cytoplasm, reduction of rhizopodial activity, and an increase in the opacity of the shell. Specimens from levels 1-3 were prepared for LA-ICPMS analyses. Individual *N. pachyderma* were cleaned to remove remnant organics using an oxidative 1:1 solution of 30% H_2O_2:0.1N NaOH in a water bath at ~65°C for 40 minutes in conjunction with 4 rinses in methanol preceding and following the oxidative step (Mashiotta et al., 1999). No sonication was used in the cleaning process to avoid physical breakage of shells. This cleaning procedure is sufficiently rigorous to remove organic contamination, while avoiding dissolution of the fragile calcite layers. After cleaning, *N. pachyderma* shells were mounted on carbon tape and imaged in variable pressure mode using a Hitachi TM300 scanning electron microscope (SEM) in

the UC Davis Department of Earth and Planetary Sciences. The resultant images were reviewed to assess shell microstructure and to note the orientation of the shells for subsequent analyses.

LA-ICPMS analytical method

Between three and four LA-ICPMS spots from 151 shells were analyzed to quantify domain-specific TE/Ca profiles through shell walls. *Neogloboquadrina pachyderma* shells were analyzed for TE/Ca trace elements (^{11}B, ^{24}Mg, ^{25}Mg, ^{27}Al, ^{43}Ca, ^{44}Ca, ^{55}Mn, ^{66}Zn, ^{86}Sr, ^{87}Sr, ^{88}Sr, and ^{138}Ba,) by ablating from the exterior of the shell to the interior using a Photon Machines pulsed 193 nm ArF UV excimer laser with a HelEx dual-volume sample chamber coupled to a Thermo Scientific X-series II quadrupole ICPMS at Oregon State University. Square 40x40 μm spots were ablated using a repetition rate of 5 Hz and a fluence of 1.27 J/cm^2 to generate replicate profiles from each shell, while acquiring enough material to measure multiple elements simultaneously. Spot locations were chosen preferentially on areas of the most recent/final (F) or second most recent chambers (F-1) on the shell surface oriented perpendicular to the laser beam. Occasionally earlier chambers were analyzed on individuals that were oriented askew, or if the F and F-1 chambers were too thin for a sufficient signal, as previous results indicate no statistically significant difference in Mg/Ca between adult chambers in individual *N. pachyderma* (Davis et al., 2017). Complete analytical settings are summarized in Table S1.

We reduced and analyzed LA-ICPMS data using the LAtools software package (specific settings shown in Table S1; Branson et al., 2019). Data reduction included a despiking routine, identifying and excluding the background counts, and applying a background correction to the data. Counts on NIST glass standards 610 and 612 during each analytical session were used to generate and subsequently apply a time-sensitive calibration calculation and standardization in

LAtools. Elemental counts were normalized to ^{43}Ca counts. For each LA-ICPMS spot, TE/Ca profiles through the shell wall (outside to the inside) are plotted against ablation time (seconds) to reveal the internal pattern of trace element variability.

Post-analysis

The reduced and calibrated TE/Ca results were further standardized using a filter of 2x the natural abundance of $^{86}Sr/^{43}Ca$ to extract data from the portions of the shell grown in the laboratory conditions from the ocean-grown calcite (Figure 1). Many shells contained a transitional zone of calcite that contained both ocean and culture-grown calcite (Figure 1), but only portions of shell regions with a >2x ambient $^{86}Sr/^{87}Sr$ signature are presented as culture-grown calcite. Further, the initial ~5 seconds of each spot analysis was removed due to the presence of a high TE/Ca shell surface (as discussed in Hathorne et al., 2003; Sadekov et al., 2010). The resultant traces were evaluated in concert with the SEM photos to assess whether each individual produced crust calcite, which is indicated by presence of a more rigid shell, less distinct chambers, blockier calcite, and a shift in the geochemistry (Figure S1). Since the density of $CaCO_3$ varies throughout *N. pachyderma* shell walls in tandem with differences in micro-texture (Livsey et al., 2020), the ablation time was not converted to depth in the shell wall. In shells that appeared to have crusting as indicated by SEM (Figure S1), the Mg/Ca profiles were scrutinized to manually determine where the crust and LC transition occurs based upon homogenous and lower Mg/Ca concentrations in the crust (Figure 1). The culture-grown crust and LC data for all trace elements were then averaged for each ablation profile. Averages were only calculated on domains that consisted of at least 10 seconds of ablation time. Additionally, whole shell values were calculated by averaging all culture-grown calcite for each LA-ICPMS profile, therefore including both LC and crust calcite. Only the calcite that is enriched in ^{86}Sr is included, unless explicitly stated.

Statistical treatment of data

To test correlations between crust and LC trace elemental data, a Kruskal-Wallis (K-W) one-way analysis of variance was performed on average spot values for each trace element. Kruskal-Wallis tests were performed using the stats package in R Studio (R Core Team, 2018) and the resulting p-values of ≤ 0.05 indicate that there is a statistically significant difference between the mean values of the LC, crust, and whole values. For all trace elements that have statistically different mean values for the different domains of calcite, a Dunn's Test (within the dunn.test package; Dinno, 2017) was implemented to determine stochastic dominance among multiple pair-wise comparisons. To compare the statistical correlation between measured TE/Ca and the independent variables (water temperature and TE/Ca_{sw}), linear models were implemented using the stats package (R Core Team, 2018). Analysis of covariance for each regression was completed using a Pearson's product moment correlation coefficient, and the outputs included p-values, correlation coefficients, and adjusted R^2 values.

Results and interpretation

Outcomes of culturing

From the 294 individuals that completed their lifecycle (either died or reproduced) in culture, 151 were analyzed for trace elements via LA-ICPMS. Of these, 121 individuals either grew additional chambers (n=32) or thickened their shells while in culture conditions (n=89), and these shells were analyzed for trace elements via LA-ICPMS. Based on the presence of blocky euhedral calcite assessed by SEM coupled with a distinct geochemical shift in the LA-ICPMS ablation profiles, approximately 70 individual *N. pachyderma* were determined to have produced

a crust in culture (see Figure S1 for representative crusted textures). However, we observed that the shells used in this study are only lightly crusted resulting in a lower crust:LC ratio than typically observed in fossil *N. pachyderma* assemblages (with crust ~75-80% of total shell mass, Kohfeld et al., 1996). The degree of crusting can be approximated by comparing the relative ablation time in LA-ICPMS traces for the identified crust and LC components. In the cultured shells, the percent of crust calcite ranged between 8-80%, with a mean of 42% (Table S2). The number of shells that displayed both LC and crust grown while in culture conditions was low, likely due to the mixing/fragmentation of the thinner more fragile LC during LA-ICPMS analyses.

Each profile was individually assessed to discern between the various domains and to avoid mixing of multiple domains in subsequent analyses, we primarily chose LC calcite on shells that did not produce a crust in culture, and the crust data from specimens that formed either only crust or a small amount of LC in culture. For example, for Foram 803 in Figure 1, the first two spots on the F chamber were deemed to only contain LC as assessed by the lack of crust on the SEM, while the spots on the F-1 and F-3 chambers exhibit initial crusting. For Foram 881, both LA-ICPMS spots are located on the F-1 chamber, which appears moderately crusted, however, close inspection of the ablation profiles reveal that the first spot is longer than the second, and displays a distinct step in Mg/Ca, Mn/Ca, and Ba/Ca values. The first spot is interpreted to be oriented exactly perpendicular to the laser beam, and therefore both the crust and LC can be resolved, while the second is oriented slightly askew and therefore proportionally more crust calcite is analyzed (Figure 1).

Trace element patterns in LC and crust

TE/Ca from single ablation profiles were averaged for the crust (n=80 profiles on 30 shells) and LC domains (n=48 profiles on 20 shells) in foraminifera that grew ample calcite in culture. In individual foraminifera, concurrent increases in Mg/Ca, Ba/Ca, and Mn/Ca occur in each profile across the crust:LC boundary, as well as a shift to more variable concentrations in the LC. Further, a striking shift in both the TE/Ca concentrations and the variability occurs between laboratory grown and ocean-grown calcite (Figure 1). Notably, there is lower Zn/Ca in most foraminifera in the ocean-grown calcite. There is a larger amount of variability in Al/Ca, B/Ca, Ba/Ca, and Zn/Ca within ocean-grown calcite compared to both the LC and crust formed in culture conditions. For Mg/Ca and Mn/Ca, the ocean-grown calcite is less variable compared to the LC (Figure 2). The mean ocean-grown Al/Ca and B/Ca is higher than the mean concentrations within the cultured calcite, but is comparable to the median culture-grown crust values for Mn/Ca, Mg/Ca, and Zn/Ca. The mean Ba/Ca concentrations in ocean-grown calcite is comparable to the mean culture-grown LC Ba/Ca. The larger variability in the ocean-grown TE/Ca is likely driven by the variability in ocean conditions across the two months when sampling occurred.

In many specimens, the Ba/Ca and Mn/Ca increases when first transferred to culture (denoted as transition calcite) but decreases again when fully labeled (Figure 1). We hypothesize that this increase in Ba and Mn in the transitionary calcite may be caused by the amalgamation of material in the plankton tow nets, resulting in the foraminifera becoming incorporated in marine snow. As marine snow is typically enriched in trace elements compared to the open ocean (Hebel et al., 1986), it is possible that the foraminifera picked up elevated trace elements during their few hours in the marine snow microenvironment (Fehrenbacher et al., 2018).

For Mg/Ca, Mn/Ca, B/Ca, Al/Ca, Zn/Ca and Ba/Ca, LA-ICPMS profiles reveal a consistent pattern characterized by low and relatively homogeneous TE/Ca in the crust, with higher overall

and larger variations in the LC. These patterns are consistent across all of the culture treatments (3 temperatures, 3 [Ba], and 3 [Mn] concentrations). The proportion of crust to LC varies across specimen and chamber analyzed, resulting in high variability in the amount of calcite evaluated in each ablation profile, even within single shells. At the population level, there are marked increase in the concentration of Mg/Ca, Ba/Ca, Mn/Ca, and Zn/Ca transitioning from the crust to the lamellar calcite, with a more subdued difference in the Sr/Ca concentration, and variable changes in the B/Ca (Figure 2). For all TE/Ca ratios besides Sr/Ca, the LC exhibits the largest ranges in TE/Ca, while the range of values in the crust calcites is much more homogenous (Table 1).

In terms of average concentration shifts between the LC and crust, Mg/Ca decreases from 6.02 to 3.16 mmol/mol, Al/Ca from 0.154 to 0.015 mmol/mol, Ba/Ca from 2.44 to 1.22 μmol/mol, Zn/Ca from 0.045 to 0.02 mmol/mol, Mn/Ca from 0.034 to 0.01 mmol/mol, and finally B/Ca from 0.051 to 0.027 mmol/mol. While the LC and crust calcites are statistically different Ba, Mg, Mn, and Zn (Kruskal-Wallis p-values <0.05; individual p-values shown in Table S3), the TE/Ca of the two domains do overlap (Figure 2). In individual foraminifera, the lower Al/Ca, B/Ca, and Zn/Ca, values measured in the LC are comparable to the mean concentrations in the crust. However, across all TE/Ca besides Zn/Ca, the lowest crust concentrations are below any measured values within the LC.

The variability of TE/Ca within the LC is larger than in the crust, as illustrated in individual ablation profiles (Figure 1), and in the overall range of concentrations (Figure 2, Table 1). Mg/Ca displays the largest difference in variability between the crust and LC, followed by Al/Ca, Ba/Ca, Zn/Ca, and B/Ca. The amount of variability in TE/Ca between spots within the LC and crust of single foraminifera from specific treatments can be described by the standard deviation relative to the mean (RSD%). The RSD% for trace elements within *N. pachyderma* reveals the amount of

geochemical variability that occurs in the LC and crust in the absence of any environmental changes. All TE/Ca besides Sr/Ca illustrate larger ranges in RSD% in the LC relative to the crust, and higher overall RSD% in the LC (Table S4).

Domain-specific TE/Ca

Unfortunately, an issue occurred with the seawater trace element analyses, resulting in anomalous and unreasonable results. Therefore we refrain from directly comparing the measured seawater values to the calcite concentrations. Trace element concentrations in the LC, crust, and whole shells were compared to the temperatures in which the shells grew to determine if there was any correlation (Figure S3 and Table S5). Besides Mg/Ca, no trace elements showed robust correlations between temperature and concentration. For Al/Ca, Mn/Ca, Sr/Ca, and Ba/Ca, the crust calcite significantly correlated with seawater temperature, but the adjusted R^2 values range from 0.008 to 0.041 (Table S5).

Demonstration and quantification of the offsets in TE/Ca between the LC and crust calcite in *N. pachyderma* in the absence of any change in environmental conditions provides critical insights into the use of foraminiferal geochemistry as paleo-proxies. Sr was the only element of the trace elements that were measured that was not statistically distinct in LC compared to crust calcite (Figure 2). We interpret that the lower variability in Sr/Ca within shells may arise because foraminifera have a tighter biological control on the incorporation of Sr compared to other trace elements, an observation that has been previously documented (Davis et al., 2020).

While crusting has been shown to have an impact on Mg/Ca, Ba/Ca, and Mn/Ca in other culture and sediment trap studies (Hathorne et al., 2009; Steinhardt et al., 2015; Jonkers et al., 2016; Davis et al., 2017; Fehrenbacher et al., 2017; 2018; Reynolds et al., 2018), this study is the

first to reveal similar patterns in Zn/Ca, Al/Ca, and B/Ca. As new geochemical proxies are developed and the use of high-resolution analytical tools is more accessible, untangling the controls on TE/Ca variability is critical.

Further, while it is demonstrated that elements such as Ba and Mn are incorporated into foraminiferal calcite in proportion to their concentration in the surrounding seawater (Munsel et al., 2010; Hönisch et al., 2011; Barras et al., 2018; van Dijk et al., 2019; Fehrenbacher et al., 2018), our data suggest that the crust and LC do not incorporate trace elements following the same relationship. A domain-specific partition coefficient (K_D) is the likeliest explanation for the difference in trace elements through *N. pachyderma* shells since it is not reasonable to expect a shift in the concentration of trace elements in the ambient cultured seawater. However, due to the anomalous seawater chemistry measurements, we are unable to calculate the domain-specific K_D. The high range of measured TE/Ca in ocean-grown calcite suggests that the range of TE/Ca in cultured seawater was lower than what populations experience over a ~2 month period in a restricted geographical location.

The relationship between Ba/Ca has previously been calculated for non-spinose planktic foraminifera, which produce a D_{Ba} of 0.11-0.22 (Hall et al., 2004; Fehrenbacher et al., 2019). Applying this D_{Ba} (0.11±0.008; Fehrenbacher et al., 2018) to our measured $Ba/Ca_{calcite}$ from combined LC and crust domains in individual shells produce Ba/Ca_{sw} values between 5.32 to 33.4 μmol/mol (mean±2SD = 11.9±12.7 μmol/mol; Table S6). Further, the individual shell LC data produce a Ba/Ca_{sw} range from 6.85 to 33.4 μmol/mol (mean of 13.58±14.4 μmol/mol), and the crust generates Ba/Ca_{sw} between 5.32 and 23.6 μmol/mol (mean±2SD = 10.5±10.4 μmol/mol). While these values are much higher than ambient (open-ocean) Ba/Ca_{sw}, published values of Ba/Ca_{sw} from Bodega Marine Laboratory intake seawater are ~17 ($\pm$2) μmol/mol (Wheeler et al.,

2016), indicating that our calculated values range from 0.25x ambient seawater to ~2x the expected concentrations. Comparatively, the ocean-grown portions of the shells produce higher and a larger range of Ba/Ca_{sw}, from 8.08 to 46.26 μmol/mol (mean of 20.4±19.9 μmol/mol). These results support those previously documented in *Neogloboquadrina dutertrei,* another non-spinose deep-dwelling foraminifera (Fehrenbacher et al., 2018). As these Ba/Ca_{sw} values exceed those observed in the environment in which *N. pachyderma* inhabits, this suggests that the higher and more variable Ba/Ca may be a function of the individuals living within marine snow in the water column, and therefore calcifying within a Ba-enriched microenvironment (Fehrenbacher et al., 2018).

Mg/Ca as a paleotemperature proxy

Across the 8, 12, and 16ºC temperatures, individual foraminifera LC and crust calcites both show significant differences in Mg/Ca (Figure S2). However, the regression produced using the crust calcite Mg/Ca values has notably lower sensitivity to temperature compared to the other portions of calcite. The crust Mg/Ca:temperature regression is not significant ($p = 0.054$, $R^2 = 0.04$), demonstrating a weak or absent relationship between crust Mg/Ca and temperature. A Shapiro-Wilk's pairwise comparison on the data demonstrate that the crust is statistically distinct from both the LC and whole shell data ($p<3e^{-07}$, and $p<3e^{-05}$ respectively). However, the LC and whole shell groups are not distinct from one another ($p=0.01$), likely due to the high proportion of LC relative to the whole shell (Table S3), and therefore we assume the LC are dominating the whole shell calculations. Additionally, the amount of Mg/Ca variation within the LC and crust domains of shells grown at the three different temperatures reveal opposite patterns as indicated

by the RSD% (Table S7). The crust has the largest range in and overall RSD% at lower temperatures, whereas the LC RSD% range and overall values increases with temperatures.

We compare previously published Mg/Ca results and the calculated regression from *N. pachyderma* LC that grew in known temperatures with our results (Livsey et al., 2020). These Mg/Ca data align with the LC data from this study, and the respective regression coefficients are within 2σ error of one another. Combining the LC Mg/Ca data from Livsey et al. (2020) with the data collected in this study, the resulting exponential relationship is (with preexponential and exponential statistics of $\pm$ 2σ standard error; Figure 3):

$$\text{Mg/Ca (mmol/mol)} = 2.03(\pm 0.09) * e^{(0.08(\pm 0.012)*T)} \quad (1)$$

Equation 1 has a p-value of $2e^{-09}$, an adjusted R^2 of 0.32, and can be used between the temperatures of -1.8 to 16ºC.

Average Mg/Ca in the LC, crust, and whole shells can be compared to the temperature at which the calcite was grown in order to evaluate Mg incorporation as a function of temperature. As shown in Figure S2, the relatively low Mg/Ca found in *N. pachyderma* crust calcite results in a weak exponential relationship between Mg/Ca_{crust} and temperature. This supports Jonkers et al. (2021) indicating that Mg/Ca in both the crust and LC of *G. inflata* decrease with increasing depth (and therefore decreasing temperatures), suggesting that temperature does influence crust Mg/Ca, but the low sensitivity results in large errors in temperature reconstructions. The low R^2 value on our crust relationship (0.04) suggests that crust Mg/Ca from individual foraminifera is not sufficient to calculate temperatures.

However, the average Mg/Ca from the LC are correlated with temperatures, and our results improve the established relationship between LC-Mg/Ca and temperature. Since we only had three temperature treatments in the study, we included LC-only Mg/Ca results from additional *N.*

pachyderma (Davis et al., 2017; Livsey et al., 2020). The resulting relationship (Eq. 1) extends the temperature calibration range to between -2 and 16ºC, encompassing the full range of *N. pachyderma* habitat. This equation not only extends the range of environments where this calibration can be used, but the agreement between populations of *N. pachyderma* from disparate geographic regions and populations (temperate Pacific to subpolar Atlantic), and different sources (field collected vs. culture grown), suggests that a single relationship may be used globally. Further, both the pre-exponential and exponential coefficients 2σ errors have improved, indicating that this updated relationship is stronger with a smaller error envelope.

Large differences in Mg/Ca between the LC and crust calcite in fossil *N. pachyderma* have been attributed to the sinking of *N. pachyderma* to deeper and colder waters where they calcify the crust (i.e. Carstens and Wefer, 1992; Kohfeld et al., 1996). However, high-resolution Mg/Ca mapping studies on *N. pachyderma* grown in an isothermal water column reveal that the shift in Mg/Ca occurs in the absence of temperature variation (Jonkers et al., 2016). Our results on cultured *N. pachyderma* that produced crust calcite in the laboratory at constant conditions provide further evidence that the shift in Mg/Ca between the LC and crust is not controlled by a change in the temperature of the seawater due to a change in depth habitat.

Non-environmental controls on trace element incorporation

A number of recent studies have hypothesized that the difference in geochemistry between the crust and LC of crust-forming planktic foraminifera is due to a change in calcification rate (Jonkers et al., 2012; Steinhardt et al., 2015). However, the consistent pattern of both compatible and incompatible trace elements in *N. pachyderma* crust provides insights into the mechanism responsible for the variation. Empirical studies have shown that faster calcification rates result in

larger partition coefficients in incompatible trace elements, while the partition coefficients in compatible elements decrease (Dromgoole and Walter, 1990; Lorens, 1981; Nielsen et al., 2012; Tesoriero and Pankow, 1996; Tang et al., 2008; Gabitov and Watson, 2006; DePaolo, 2011). This is because with faster precipitation rates, trace element behavior is closer to kinetic fractionation, whereas at slower precipitation rates, equilibrium partitioning is dominant (DePaolo, 2011). While these empirical studies were on inorganic precipitation, there has also been evidence from cultured foraminifera that indicate that calcification rate follows the same pattern (Allen et al., 2016). The coincident decrease in both large and small ions in *N. pachyderma* crust calcite argues against the hypothesis that a decrease in the calcification rates is the mechanism causing low TE/Ca in crust calcite.

While the crust and LC are distinct in terms of both patterns and concentrations of TE/Ca, the concentrations of TE/Ca in the crust are equivalent to the low end of the LC TE/Ca ranges (Figure 2). These results support the findings of previous work on Mg/Ca in *N. pachyderma* (Jonkers et al., 2016), and *Globorotalia inflata* (Jonkers et al., 2021), which postulate that the presence of Mg/Ca banding in the LC are what drive the higher average concentrations and variability relative to the crust. In those studies, the authors imply that the trace metal incorporation does not change between the crust and LC, but rather that the crust lacks banding. However, our results indicate that while Al/Ca, Ba/Ca, B/Ca, Zn/Ca, and Mn/Ca also exhibit higher concentrations in the LC compared to the crust, the lowest values of trace elements in the crust calcite fall below even the lowest TE/Ca in the LC. This pattern reveals that even in the absence of high concentration TE banding in the LC, there would still be an offset from average crust values. Additionally, Sr/Ca concentrations should coincide with Mg/Ca (Kisakürek et al., 2008), however there is no discernable difference between Sr/Ca in the crust and LC. This suggests the

mechanism causing the shift in the incorporation of trace elements between the LC and crust, may also be involved in the formation of TE/Ca banding in the LC.

The consistent direction and range of trace element changes between the crust and LC indicates that it is likely that there is a single mechanism impacting all of the trace elements, with the exception of Sr/Ca, similarly. Further, our data demonstrates that changes in the hydrology (i.e. temperature, salinity, depth, water mass) is not the dominant control on *N. pachyderma* crust TE/Ca. Since *N. pachyderma* found in the fossil record contain a large proportion of crust to lamellar calcite (Bauch et al., 1997), the use of whole shell geochemical reconstructions yields results that are confounded by mixing calcite types with domain-specific exchange coefficient and that are present in unknown and variable proportions.

While our data does not answer the question of what is happening to cause the shift in geochemistry between the calcite domains, it does suggest that crust and LC domains in *N. pachyderma* should be treated separately in paleo-reconstructions, with Mg/Ca:temperature relationships likely only robust within lamellar calcite.

Conclusions

The trace element concentrations of the lamellar and crust calcite in *Neogloboquadrina pachyderma* that were grown in controlled laboratory settings reveal distinct differences in TE composition. In individuals that produced crust calcite, there are distinct differences in B/Ca, Ba/Ca, Al/Ca, Mn/Ca, Zn/Ca, and Mg/Ca between the lamellar and crust calcite. Since all individuals were grown in constant conditions in culture (temperature, salinity, pH, and $[TE]_{sw}$), these data suggest that a different mechanism controls trace element incorporation during crust formation. Further, we show that the formation of crust calcite in *N. pachyderma* is not always triggered by a change in seawater temperature. Evaluation of lamellar and crust calcite grown at

multiple temperatures reveals 1) the sensitivity of crust calcite Mg/Ca to temperature is too low to accurately use it to calculate temperatures in the fossil record, and 2) the LC Mg/Ca results support the LC-specific Mg/Ca to temperature relationship proposed by Livsey et al. (2020), and together extend the calibration to a wider temperature range (-2 to 16ºC). These results indicate that the geochemical changes associated with crust formation in *N. pachyderma* are not reflective of a different environment (see also Jonkers et al., 2021), or a function of a shift in calcification rate. Additional research needs to be performed to fully understand the physiological changes associated with crust formation in *N. pachyderma* and the mechanism responsible for the distinct TE geochemistry.

FIGURES AND TABLES

Table 1. Average, 2 SD, and range of TE/Ca values for the LC, crust, and whole shells. *12□ treatments.

	Sr^{87}/Ca (mmol/mol)			Ba/Ca (μmol/mol)			Zn/Ca (mmol/mol)			Mn/Ca (mmol/mol)			Al/Ca (mmol/mol)			Mg/Ca (mmol/mol)*			B/Ca (mmol/mol)		
	range	2SD	ave	range	2SD	ave	range	2SD	ave	range	2SD	ave	range	2SD	ave	range	2SD	ave	range	2SD	ave
lamellar calcite (LC)	0.46	0.17	0.36	3.11	2.14	2.44	0.175	0.060	0.045	0.085	0.052	0.034	5.30	1.65	0.154	16.08	8.56	6.02	0.071	0.029	0.051

crust	whole shells
0.027	0.024
0.014	0.014
0.029	0.060
3.16	4.87
3.55	4.84
7.33	9.37
0.015	0.020
0.038	0.066
0.128	0.219
0.010	0.012
0.007	0.011
0.024	0.019
0.020	0.026
0.022	0.026
0.048	0.061
1.22	1.30
1.39	1.20
2.22	2.05
0.32	0.32
0.05	0.05
0.11	0.12

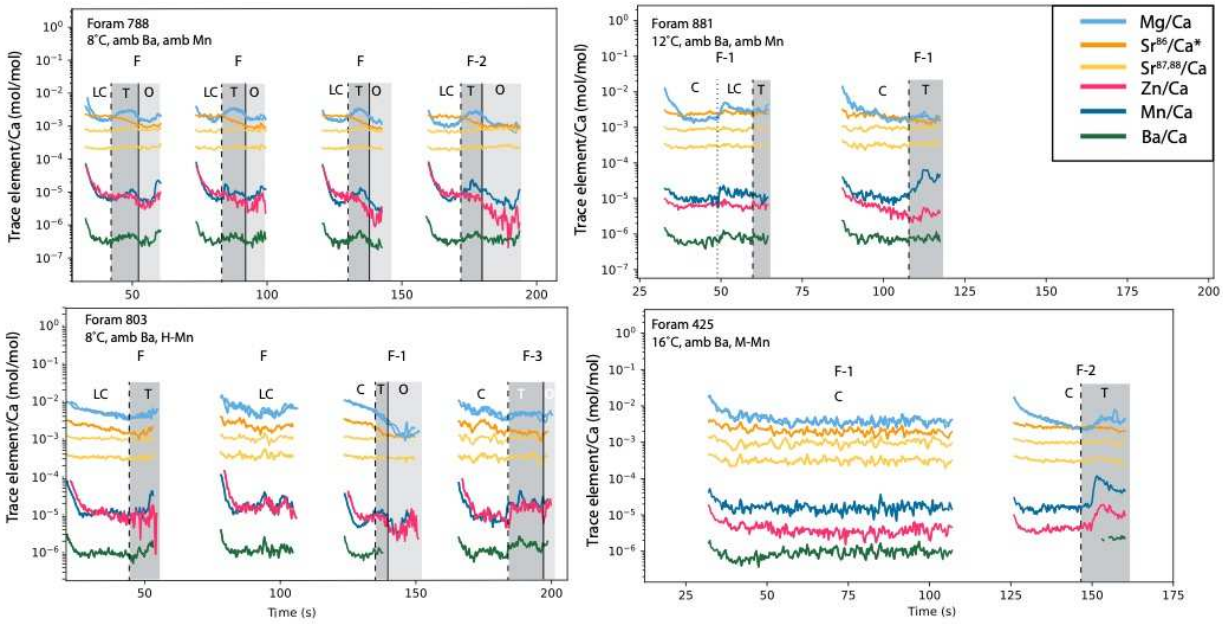

Figure 1. Representative LA-ICPMS depth profiles from spots on four foraminifera specimens that contain various amounts of ocean-grown (O), transitionary (T), crust (C), and lamellar calcite (LC). The colored traces represent different trace element/Ca ratios in mol/mol and are plotted against ablation time (s). Each ablation profile was analyzed from the outside of the shell to the inside and the chamber analyzed is noted directly above each profile. Sr^{86}/Ca* is the seawater spike and was used to determine the portions of calcite that were grown in laboratory conditions. The solid black line and light grey regions of each profile indicate where the calcite is not enriched in Sr^{86}/Ca relative to Sr^{88}/Ca, and therefore represent ocean-grown calcite (determined by 1.5x Sr^{86}/Sr^{88}). The darker grey boxes denote the transitionary calcite, which contains calcite that represents both oceanic conditions and culture conditions, and regions that were not included in any further data

interpretation (determined where Sr^{86} continues to increase). Finally, the dashed lines indicate where the fully culture-grown calcite is located and is labeled by the type of calcite that dominates the signal. The dotted line indicates the transition between the crust and LC within a single ablation profile.

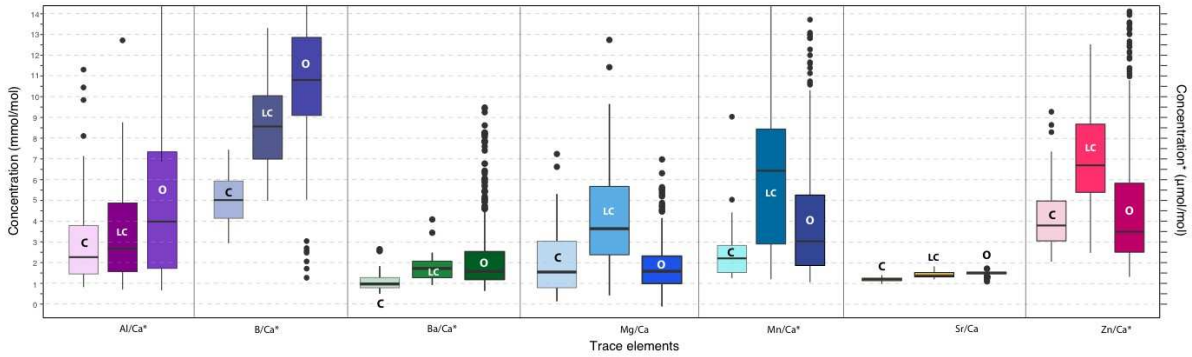

Figure 2. Box and whisker plots of average TE/Ca from cultured *N. pachyderma* crust calcite (C), lamellar calcite (LC), and ocean-grown calcite (O). The trace elements with * have a y-axis of μmol/mol rather than mmol/mol to allow all elements to be included in one plot. The solid black line represents the mean value for all calcite grown in culture from all shells. The upper portion of the boxes represent the 75% quantile, while the lower bound is the 25% quantile. The whiskers extend to-2 times the largest/smallest value no further than 1.5 times the inter-quartile range (distance between the first and third quartiles). All black points are outliers that represent single ablation spots. All trace elements demonstrate a significant difference between the LC and crust domains as indicated by a Kruskal- Wallis test of similarity.

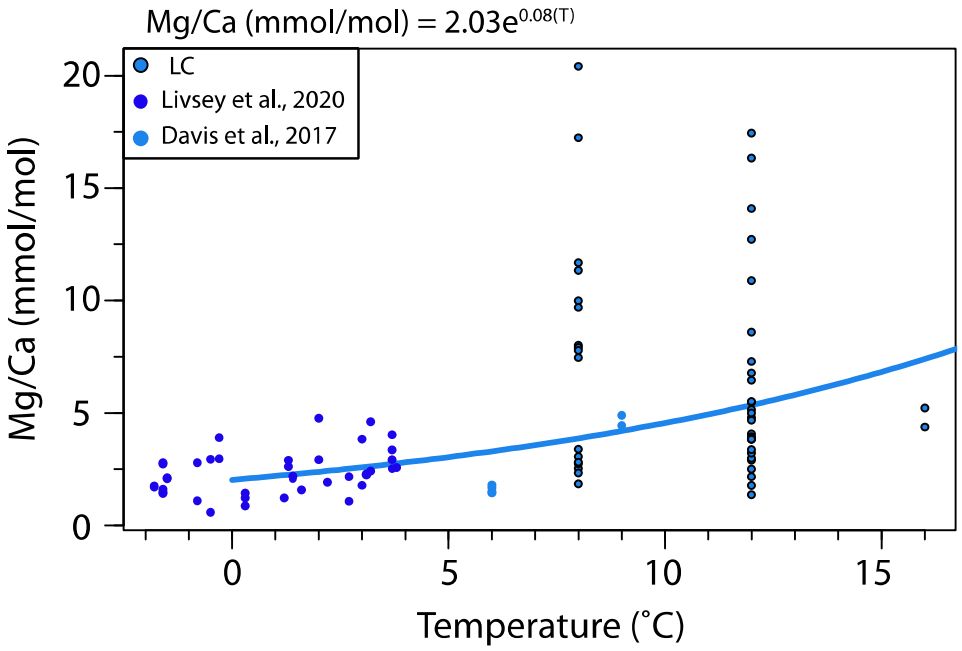

Figure 3. Plot of Mg/Ca (mmol/mol) versus temperature (ºC) from LA-ICPMS analyses on *N. pachyderma* lamellar calcite. Points (n=40) are average Mg/Ca for individual depth profiles from calcite grown at various temperatures. Additional plankton tow-collected LC data from the Fram Strait (n=36; Livsey et al., 2020) plotted in dark blue points lacking a black outline, as well additional cultured *N. pachyderma* from Bodega Bay, CA (n= 4; Davis et al., 2017) with associated temperature information. Regression adjusted R^2= 0.32, p-value= $2e^{-09.}$

REFERENCES

Allen, K. A., Hönisch, B., Eggins, S. M., Haynes, L. L., Rosenthal, Y., & Yu, J. (2016). Trace element proxies for surface ocean conditions: A synthesis of culture calibrations with planktic foraminifera. *Geochimica et Cosmochimica Acta*, *193*, 197–221.

Barras, C., Mouret, A., Nardelli, M. P., Metzger, E., Petersen, J., La, C., et al. (2018). Experimental calibration of manganese incorporation in foraminiferal calcite. *Geochimica et Cosmochimica Acta*, *237*, 49–64.

Bauch, D., Carstens, J., & Wefer, G. (1997). Oxygen isotope composition of living *Neogloboquadrina pachyderma* (sin.) in the Arctic Ocean. *Earth and Planetary Science Letters*, *146*(1–2), 47–58. https://doi.org/10.1016/S0012-821X(96)00211-7

Bé, A. W., & Ericson, D. B. (1963). Aspects of calcification in planktonic Foraminifera (Sarcodina). *Annals of the New York Academy of Sciences*, *109*, 65–81. https://doi.org/10.1111/j.1749-6632.1963.tb13462.x

Bemis, B. E., Spero, H. J., & Lea, D. W. (1998). Reevaluation of the oxygen isotopic composition of planktonic foraminifera : Experimental results and revised paleotemperature equations for both species can be described by The O . relationships accurate with photosynthetic. *Paleoceanography*, *13*(2), 150–160.

Bemis, B. E., Spero, H. J., & Thunell, R. C. (2002). Using species-specific paleotemperature equations with foraminifera: a case study in the Southern California Bight. *Marine Micropaleontology*, *46*(3–4), 405–430.

Bergami, C., Capotondi, L., Sprovieri, M., Tiepolo, M., Langone, L., Giglio, F., & Ravaioli, M. (2008). Mg/Ca ratios in the planktonic foraminifer *Neogloboquadrina pachyderma* (sinistral) from plankton tows in the Ross Sea and the Pacific sector of the Southern Ocean (Antarctica): Comparison of different methodological approaches. *Chemistry and Ecology*, *24*(SUPPL. 1), 39–46. https://doi.org/10.1080/02757540801963303

Berger, W. H. (1978). Deep-sea carbonate: pteropod distribution and the aragonite compensation depth. *Deep-Sea Research*, *25*(5), 447–452. https://doi.org/10.1016/0146-6291(78)90552-0

Bijma, J., Hönisch, B., & Zeebe, R. E. (2002). Impact of the ocean carbonate chemistry on living foraminiferal shell weight: Comment on "Carbonate ion concentration in glacial□age deep waters of the Caribbean Sea" by WS Broecker and E. Clark. *Geochemistry, Geophysics, Geosystems*, *3*(11), 1–7.

Bolton, A., & Marr, J. P. (2013). Trace element variability in crust-bearing and non crust-bearing *Neogloboquadrina incompta*, P-D intergrade and *Globoconella inflata* from the Southwest Pacific Ocean: Potential paleoceanographic implications. *Marine Micropaleontology*, *100*(May), 21–33. https://doi.org/10.1016/j.marmicro.2013.03.008

Boyle, E. A. (1995). Limits on benthic foraminiferal chemical analyses as precise measures of environmental properties. *The Journal of Foraminiferal Research*, *25*(1), 4–13.

Branson, O., Kaczmarek, K., Redfern, S. A. T., Misra, S., Langer, G., Tyliszczak, T., et al. (2015). The coordination and distribution of B in foraminiferal calcite. *Earth and Planetary Science Letters*, *416*, 67–72. https://doi.org/10.1016/j.epsl.2015.02.006

Branson, O., Fehrenbacher, J. S., Vetter, L., Sadekov, A. Y., Eggins, S. M., & Spero, H. J. (2019). LAtools: A data analysis package for the reproducible reduction of LA-ICPMS data. *Chemical Geology*, *504*, 83–95.

Brown, S. J., & Elderfield, H. (1996). Variations in Mg/Ca and Sr/Ca ratios of planktonic foraminifera caused by postdepositional dissolution: Evidence of shallow Mg-dependent dissolution. *Paleoceanography*, *11*(5), 543–551. https://doi.org/10.1029/96PA01491

Carstens, Jö., & Wefer, G. (1992). Recent distribution of planktonic foraminifera in the Nansen Basin, Arctic Ocean. *Deep Sea Research Part A. Oceanographic Research Papers*, *39*(2), S507–S524.

Davis, C. V., Fehrenbacher, J. S., Hill, T. M., Russell, A. D., & Spero, H. J. (2017). Relationships Between Temperature, pH, and Crusting on Mg/Ca Ratios in Laboratory-Grown Neogloboquadrina Foraminifera. *Paleoceanography*, *32*(11), 1137–1152. https://doi.org/10.1002/2017PA003111

Davis, C. V, Fehrenbacher, J. S., Benitez-Nelson, C., & Thunell, R. C. (2020). Trace Element Heterogeneity Across Individual Planktic Foraminifera from the Modern Cariaco Basin. *Journal of Foraminiferal Research*, *50*(2), 204–218.

DePaolo, D. J. (2011). Surface kinetic model for isotopic and trace element fractionation during precipitation of calcite from aqueous solutions. *Geochimica et Cosmochimica Acta*, *75*(4), 1039–1056.

Dinno, A. (2017). dunn.test: Dunn's Test of Multiple Comparisons Using Rank Sums. R package version 1.3.5. https://CRAN.R-project.org/package=dunn.test

Dromgoole, E. L., & Walter, L. M. (1990). Iron and manganese incorporation into calcite: Effects of growth kinetics, temperature and solution chemistry. *Chemical Geology*, *81*(4), 311–336. https://doi.org/https://doi.org/10.1016/0009-2541(90)90053-A

Duplessy, J. C., Bé, A. W. H., & Blanc, P. L. (1981). Oxygen and carbon isotopic composition and biogeographic distribution of planktonic foraminifera in the Indian Ocean. *Palaeogeography, Palaeoclimatology, Palaeoecology*, *33*(1), 9–46. https://doi.org/https://doi.org/10.1016/0031-0182(81)90031-6

Eggins, S. M., Sadekov, A., & De Deckker, P. (2004). Modulation and daily banding of Mg/Ca in *Orbulina universa* tests by symbiont photosynthesis and respiration: A complication for seawater thermometry? *Earth and Planetary Science Letters*, *225*(3–4), 411–419. https://doi.org/10.1016/j.epsl.2004.06.019

Elderfield, H., & Ganssen, G. (2000). Past temperature and $\delta^{18}O$ of surface ocean waters inferred from foraminiferal Mg/Ca ratios. *Nature*, *405*(6785), 442–445. https://doi.org/10.1038/35013033

Elderfield, H., Vautravers, M., & Cooper, M. (2002). The relationship between shell size and Mg/Ca, Sr/Ca, $\delta^{18}O$, and $\delta^{13}C$ of species of planktonic foraminifera. *Geochemistry, Geophysics, Geosystems*, *3*(8), 1–13.

Erez, J. (2003). The source of ions for biomineralization in foraminifera and their implications for paleoceanographic proxies. *Reviews in Mineralogy and Geochemistry*, *54*(1), 115–149.

Evans, D., Bhatia, R., Stoll, H., & Müller, W. (2015). LA□ICPMS Ba/Ca analyses of planktic foraminifera from the Bay of Bengal: Implications for late Pleistocene orbital control on monsoon freshwater flux. *Geochemistry, Geophysics, Geosystems*, *16*(8), 2598–2618.

Ezard, T. H. G., Edgar, K. M., & Hull, P. M. (2015). Environmental and biological controls on size□specific $\delta^{13}C$ and $\delta^{18}O$ in recent planktonic foraminifera. *Paleoceanography*, *30*(3), 151–173.

Fehrenbacher, J. S., Russell, A. D., Davis, C. V., Gagnon, A. C., Spero, H. J., Cliff, J. B., et al. (2017). Link between light-triggered Mg-banding and chamber formation in the planktic foraminifera *Neogloboquadrina dutertrei*. *Nature Communications*, *8*(May). https://doi.org/10.1038/ncomms15441

Fehrenbacher, J. S., Russell, A. D., Davis, C. V., Spero, H. J., Chu, E., & Hönisch, B. (2018). Ba/Ca ratios in the non-spinose planktic foraminifer *Neogloboquadrina dutertrei*: Evidence for an organic aggregate microhabitat. *Geochimica et Cosmochimica Acta*, *236*, 361–372. https://doi.org/10.1016/j.gca.2018.03.008

Friedrich, O., Schiebel, R., Wilson, P. A., Weldeab, S., Beer, C. J., Cooper, M. J., & Fiebig, J. (2012). Influence of test size, water depth, and ecology on Mg/Ca, Sr/Ca, $\delta^{18}O$ and $\delta^{13}C$ in nine modern species of planktic foraminifers. *Earth and Planetary Science Letters*, *319*, 133–145.

Gabitov, R. I., & Watson, E. B. (2006). Partitioning of strontium between calcite and fluid. *Geochemistry, Geophysics, Geosystems*, *7*(11).

Groeneveld, J., Ho, S. L., Mackensen, A., Mohtadi, M., & Laepple, T. (2019). Deciphering the variability in Mg/Ca and stable oxygen isotopes of individual foraminifera. *Paleoceanography and Paleoclimatology*, *34*(5), 755–773.

Hall, J. M., & Chan, L. H. (2004). Ba/Ca in *Neogloboquadrina pachyderma* as an indicator of deglacial meltwater discharge into the western Arctic Ocean. *Paleoceanography*, *19*(1), 1–9. https://doi.org/10.1029/2003PA000910

Hathorne, E. C., Alard, O., James, R. H., & Rogers, N. W. (2003). Determination of intratest variability of trace elements in foraminifera by laser ablation inductively coupled plasma-mass spectrometry. *Geochemistry, Geophysics, Geosystems*, *4*(12). https://doi.org/10.1029/2003GC000539

Hathorne, E. C., James, R. H., & Lampitt, R. S. (2009). Environmental versus biomineralization controls on the intratest variation in the trace element composition of the planktonic foraminifera *G. inflata* and *G. scitula*. *Paleoceanography*, *24*(4). https://doi.org/10.1029/2009PA001742

Hemleben, C., Spindler, M., Breitinger, I., & Deuser, W. G. (1985). Field and laboratory studies on the ontogeny and ecology of some globorotaliid species from the Sargasso Sea off Bermuda. *Journal of Foraminiferal Research*, *15*(4), 254–272.

Hendry, K. R., Rickaby, R. E. M., Meredith, M. P., & Elderfield, H. (2009). Controls on stable isotope and trace metal uptake in *Neogloboquadrina pachyderma* (sinistral) from an Antarctic sea-ice environment. *Earth and Planetary Science Letters*, *278*(1–2), 67–77. https://doi.org/10.1016/j.epsl.2008.11.026

Holland, K., Eggins, S. M., Hönisch, B., Haynes, L. L., & Branson, O. (2017). Calcification rate and shell chemistry response of the planktic foraminifer *Orbulina universa* to changes in microenvironment seawater carbonate chemistry. *Earth and Planetary Science Letters*, *464*, 124–134.

Hönisch, B., Allen, K. A., Russell, A. D., Eggins, S. M., Bijma, J., Spero, H. J., et al. (2011). Planktic foraminifers as recorders of seawater Ba/Ca. *Marine Micropaleontology*, *79*(1–2), 52–57. https://doi.org/10.1016/j.marmicro.2011.01.003

Hönisch, B., Allen, K. A., Lea, D. W., Spero, H. J., Eggins, S. M., Arbuszewski, J., et al. (2013). The influence of salinity on Mg/Ca in planktic foraminifers - Evidence from cultures, core-top sediments and complementary $\delta^{18}O$. *Geochimica et Cosmochimica Acta*, *121*, 196–213. https://doi.org/10.1016/j.gca.2013.07.028

Hori, M., Shirai, K., Kimoto, K., Kurasawa, A., Takagi, H., Ishida, A., et al. (2018). Chamber formation and trace element distribution in the calcite walls of laboratory cultured planktonic foraminifera (*Globigerina bulloides* and *Globigerinoides ruber*). *Marine Micropaleontology*, *140*(December 2017), 46–55. https://doi.org/10.1016/j.marmicro.2017.12.004

Johannessen, O. M., Bengtsson, L., Miles, M. W., Kuzmina, S. I., Semenov, V. A., Alekseev, G. V, et al. (2004). Arctic climate change: observed and modelled temperature and sea-ice variability. *Tellus A: Dynamic Meteorology and Oceanography*, *56*(4), 328–341.

Jonkers, L., Jiménez-Amat, P., Mortyn, P. G., & Brummer, G. J. A. (2013). Seasonal Mg/Ca variability of *N. pachyderma* (s) and *G. bulloides*: Implications for seawater temperature reconstruction. *Earth and Planetary Science Letters*, *376*, 137–144. https://doi.org/10.1016/j.epsl.2013.06.019

Jonkers, L., Buse, B., Brummer, G. J. A., & Hall, I. R. (2016). Chamber formation leads to Mg/Ca banding in the planktonic foraminifer *Neogloboquadrina pachyderma*. *Earth and Planetary Science Letters*, *451*, 177–184. https://doi.org/10.1016/j.epsl.2016.07.030

Jonkers, L., Gopalakrishnan, A., Weßel, L., Chiessi, C. M., Groeneveld, J., Monien, P., et al. (2021). Morphotype and crust effects on the geochemistry of *Globorotalia inflata*. *Paleoceanography and Paleoclimatology*, *36*(4), e2021PA004224.

Katz, M. E., Cramer, B. S., Franzese, a., Honisch, B., Miller, K. G., Rosenthal, Y., & Wright, J. D. (2010). Traditional and Emerging Geochemical Proxies in Foraminifera. *The Journal of Foraminiferal Research*, *40*(2), 165–192. https://doi.org/10.2113/gsjfr.40.2.165

Kısakürek, B., Eisenhauer, A., Böhm, F., Garbe-Schönberg, D., & Erez, J. (2008). Controls on shell Mg/Ca and Sr/Ca in cultured planktonic foraminiferan, *Globigerinoides ruber* (white). *Earth and Planetary Science Letters*, *273*(3), 260–269. https://doi.org/https://doi.org/10.1016/j.epsl.2008.06.026

Kohfeld, K. E., Fairbanks, R. G., Smith, S. L., & Walsh, I. D. (1996). *Neogloboquadrina pachyderma* (sinistral coiling) as paleoceanographic tracers in polar oceans: Evidence from Northeast Water Polynya plankton tows, sediment traps, and surface sediments. *Paleoceanography*, *11*(6), 679–699. https://doi.org/10.1029/96PA02617

Kozdon, R., Ushikubo, T., Kita, N. T., Spicuzza, M., & Valley, J. W. (2009). Intratest oxygen isotope variability in the planktonic foraminifer *N. pachyderma*: Real vs. apparent vital effects by ion microprobe. *Chemical Geology*, *258*(3–4), 327–337. https://doi.org/10.1016/j.chemgeo.2008.10.032

Kucera, M., & Darling, K. (2002). Cryptic species of planktonic foraminifera: Their effect on palaeoceanographic reconstructions. *Philosophical Transactions. Series A, Mathematical, Physical, and Engineering Sciences*, *360*, 695–718. https://doi.org/10.1098/rsta.2001.0962

Kucera, M. (2007). Chapter Six Planktonic Foraminifera as Tracers of Past Oceanic Environments. *Developments in Marine Geology*, *1*(07), 213–262. https://doi.org/10.1016/S1572-5480(07)01011-1

Lea, D. W., & Spero, H. J. (1994). Assessing the reliability of paleochemical tracers: Barium uptake in the shells of planktonic foraminifera. *Paleoceanography*, *9*(3), 445–452. https://doi.org/10.1029/94PA00151

Lea, D. W., Mashiotta, T. A., & Spero, H. J. (1999). Controls on magnesium and strontium uptake in planktonic foraminifera determined by live culturing. *Geochimica et Cosmochimica Acta*, *63*(16), 2369–2379. https://doi.org/10.1016/S0016-7037(99)00197-0

Livsey, C. M., Kozdon, R., Bauch, D., Brummer, G. J. A., Jonkers, L., Orland, I., et al. (2020). High-Resolution Mg/Ca and $\delta^{18}O$ Patterns in Modern *Neogloboquadrina pachyderma* From the Fram Strait and Irminger Sea. *Paleoceanography and Paleoclimatology*, *35*(9). https://doi.org/10.1029/2020PA003969

Lohmann, G. P., & Schweitzer, P. N. (1990). *Globorotalia truncatulinoides'* Growth and chemistry as probes of the past thermocline: 1. Shell size. *Paleoceanography*, *5*(1), 55–75. https://doi.org/10.1029/PA005i001p00055

Lohmann, G. P. (1995). A model for variation in the chemistry of planktonic foraminifera due to secondary calcification and selective dissolution. *Paleoceanography*, *10*(3), 445–457. https://doi.org/https://doi.org/10.1029/95PA00059

Lončarić, N., Peeters, F. J. C., Kroon, D., & Brummer, G. A. (2006). Oxygen isotope ecology of recent planktic foraminifera at the central Walvis Ridge (SE Atlantic). *Paleoceanography*, *21*(3).

Lorens, R. B. (1981). Sr, Cd, Mn and Co distribution coefficients in calcite as a function of calcite precipitation rate. *Geochimica et Cosmochimica Acta*, *45*(4), 553–561.

Marchitto, T. M., Lynch-Stieglitz, J., & Hemming, S. R. (2005). Deep Pacific $CaCO_3$ compensation and glacial–interglacial atmospheric CO_2. *Earth and Planetary Science Letters*, *231*(3–4), 317–336.

Marr, J. P., Carter, L., Bostock, H. C., Bolton, A., & Smith, E. (2013). Southwest Pacific Ocean response to a warming world: Using Mg/Ca, Zn/Ca, and Mn/Ca in foraminifera to track surface ocean water masses during the last deglaciation. *Paleoceanography*, *28*(2), 347–362.

Mashiotta, T., Lea, D. W., & Spero, H. J. (1999). Glacial-interglacial changes in subantarctic sea surface temperature and $\delta^{18}O$-water using foraminiferal Mg. *Earth and Planetary Science Letters*, *170*(April), 417–432.

Morard, R., Reinelt, M., Chiessi, C. M., Groeneveld, J., & Kucera, M. (2016). Tracing shifts of oceanic fronts using the cryptic diversity of the planktonic foraminifera *Globorotalia inflata*. *Paleoceanography*, *31*(9), 1193–1205.

Mortyn, P. G., & Charles, C. D. (2003). Planktonic foraminiferal depth habitat and $\delta^{18}O$ calibrations: Plankton tow results from the Atlantic sector of the Southern Ocean. *Paleoceanography*, *18*(2).

Mulitza, S., Boltovskoy, D., Donner, B., Meggers, H., Paul, A., & Wefer, G. (2003). Temperature: $\delta^{18}O$ relationships of planktonic foraminifera collected from surface waters. *Palaeogeography, Palaeoclimatology, Palaeoecology*, *202*(1–2), 143–152. https://doi.org/10.1016/S0031-0182(03)00633-3

Munsel, D., Kramar, U., Dissard, D., Nehrke, G., Berner, Z., Bijma, J., et al. (2010). Heavy metal incorporation in foraminiferal calcite: results from multi-element enrichment culture experiments with *Ammonia tepida*. *Biogeosciences*, *7*(8), 2339–2350.

Nielsen, L. C., DePaolo, D. J., & De Yoreo, J. J. (2012). Self-consistent ion-by-ion growth model for kinetic isotopic fractionation during calcite precipitation. *Geochimica et Cosmochimica Acta*, *86*, 166–181.

Numberger, L., Hemleben, C., Hoffmann, R., Mackensen, A., Schulz, H., Wunderlich, J.-M., & Kucera, M. (2009, November 13). Abundance patterns and isotopic signals of morphotypes of Globigerinoides ruber. *Supplement to: Numberger, L et Al. (2009): Habitats, Abundance Patterns and Isotopic Signals of Morphotypes of the Planktonic Foraminifer Globigerinoides Ruber (d'Orbigny) in the Eastern Mediterranean Sea since the Marine Isotopic Stage 12. Marine Micropa*. PANGAEA. https://doi.org/10.1594/PANGAEA.729188

Nürnberg, D. (1995). Magnesium in tests of *Neogloboquadrina pachyderma* sinistral from high northern and southern latitudes. *Journal of Foraminiferal Research - J FORAMIN RES*, *25*, 350–368. https://doi.org/10.2113/gsjfr.25.4.350

Nurnberg, D., Schubert, C. J., Spielhagen, R. F., & Wahsner, M. (1995). The depositional environment of the Laptev Sea continental margin : Preliminary results from the R / V POLARSTERN ARK IX-4 cruise, *8369*(August 2017). https://doi.org/10.3402/polar.v14i1.6650

Nürnberg, D., Bijma, J., & Hemleben, C. (1996). Assessing the reliability of magnesium in foraminiferal calcite as a proxy for water mass temperatures. *Geochimica et Cosmochimica Acta*, *60*(5), 803–814. https://doi.org/10.1016/0016-7037(95)00446-7

Orr, W. N. (1967). Secondary calcification in the foraminiferal genus globorotalia. *Science (New York, N.Y.)*, *157*(3796), 1554–1555. https://doi.org/10.1126/science.157.3796.1554

Pados, T., Spielhagen, R. F., Bauch, D., Meyer, H., & Segl, M. (2014). Oxygen and carbon isotope composition of modern planktic foraminifera and near-surface waters in the Fram Strait (Arctic Ocean) – a case-study. *Biogeosciences Discussions*, *11*(6), 8635–8672. https://doi.org/10.5194/bgd-11-8635-2014

R Core Team (2018) R: A Language and Environment for Statistical Computing. R Foundation for Statistical Computing, Vienna. https://www.R-project.org

Regenberg, M., Regenberg, A., Garbe-Schönberg, D., & Lea, D. W. (2014). Global dissolution effects on planktonic foraminiferal Mg/Ca ratios controlled by the calcite-saturation state of bottom waters. *Paleoceanography*, *29*(3), 127–142. https://doi.org/10.1002/2013PA002492

Reynolds, L. A., & Thunell, R. C. (1986). Seasonal production and morphologic variation of Neogloboquadrina pachyderma (Ehrenberg) in the northeast Pacific. *Micropaleontology*, *32*(1), 1–18.

Reynolds, C. E., Richey, J. N., Fehrenbacher, J. S., Rosenheim, B. E., & Spero, H. J. (2018). Environmental controls on the geochemistry of *Globorotalia truncatulinoides* in the Gulf of Mexico: Implications for paleoceanographic reconstructions. *Marine Micropaleontology*, *142*, 92–104.

Russell, A. D., & Spero, H. J. (2000). Field examination of the oceanic carbonate ion effect on stable isotopes in planktonic foraminifera. *Paleoceanography*, *15*(1), 43–52.

Russell, A. D., Hönisch, B., Spero, H. J., & Lea, D. W. (2004). Effects of seawater carbonate ion concentration and temperature on shell U, Mg, and Sr in cultured planktonic foraminifera. *Geochimica et Cosmochimica Acta*, *68*(21), 4347–4361.

Sadekov, A. Y., Eggins, S. M., & De Deckker, P. (2005). Characterization of Mg/Ca distributions in planktonic foraminifera species by electron microprobe mapping. *Geochemistry, Geophysics, Geosystems*, *6*(12). https://doi.org/10.1029/2005GC000973

Sadekov, A., Eggins, S. M., De Deckker, P., & Kroon, D. (2008). Uncertainties in seawater thermometry deriving from intratest and intertest Mg/Ca variability *in Globigerinoides ruber*. *Paleoceanography*, *23*(1).

Sadekov, A. Y., Eggins, S. M., Klinkhammer, G. P., & Rosenthal, Y. (2010). Effects of seafloor and laboratory dissolution on the Mg/Ca composition of *Globigerinoides sacculifer* and *Orbulina universa* tests - A laser ablation ICPMS microanalysis perspective. *Earth and Planetary Science Letters*, *292*(3–4), 312–324. https://doi.org/10.1016/j.epsl.2010.01.039

Sadekov, A. Y., Darling, K. F., Ishimura, T., Wade, C. M., Kimoto, K., Singh, A. D., et al. (2016). Geochemical imprints of genotypic variants of *Globigerina bulloides* in the Arabian Sea. *Paleoceanography*, *31*(10), 1440–1452. https://doi.org/10.1002/2016PA002947

Schiebel, R., Smart, S. M., Jentzen, A., Jonkers, L., Morard, R., Meilland, J., et al. (2018). Model ScienceDirect Advances in planktonic foraminifer research: New perspectives for paleoceanography ARTICLE IN PRESS. *Revue de Micropaleontologie*, *61*, 113–138. https://doi.org/10.1016/j.revmic.2018.10.001

Serreze, M. C., Walsh, J. E., Chapin, F. S., Osterkamp, T., Dyurgerov, M., Romanovsky, V., et al. (2000). Observational evidence of recent change in the northern high-latitude environment. *Climatic Change*, *46*(1), 159–207.

Serreze, M. C., Barrett, A. P., Stroeve, J. C., Kindig, D. N., & Holland, M. M. (2009). The emergence of surface-based Arctic amplification. *Cryosphere*, *3*(1), 11–19. https://doi.org/10.5194/tc-3-11-2009

Spero, H. J., & DeNiro, M. J. (1987). The influence of symbiont photosynthesis on the $\delta^{18}O$ and $\delta^{13}C$ values of planktonic foraminiferal shell calcite. *Symbiosis*, *4*(1–3), 213–228.

Spero, H. J., & Lea, D. W. (1996). Experimental determination of stable isotope variability in *Globigerina bulloides*: implications for paleoceanographic reconstructions. *Marine Micropaleontology*, *28*(3), 231–246. https://doi.org/https://doi.org/10.1016/0377-8398(96)00003-5

Spero, H. J., Bijma, J., Lea, D. W., & Bemis, B. E. (1997). Effect of seawater carbonate concentration on foraminiferal carbon and oxygen isotopes. *Nature*, *390*, 497. Retrieved from https://doi.org/10.1038/37333

Spero, H. J. (1998). Life History and Stable Isotope Geochemistry of Planktonic Foraminifera. *The Paleontological Society Papers*, *4*, 7–36. https://doi.org/DOI: 10.1017/S1089332600000383

Spero, H. J., Eggins, S. M., Russell, A. D., Vetter, L., Kilburn, M. R., & Hönisch, B. (2015). Timing and mechanism for intratest Mg/Ca variability in a living planktic foraminifer. *Earth and Planetary Science Letters*, *409*, 32–42. https://doi.org/10.1016/j.epsl.2014.10.030

Steinhardt, J., Cléroux, C., De Nooijer, L. J., Brummer, G. J., Zahn, R., Ganssen, G., & Reichart, G. J. (2015). Reconciling single-chamber Mg / Ca with whole-shell $\delta^{18}O$ in surface to deep-dwelling planktonic foraminifera from the Mozambique Channel. *Biogeosciences*, *12*(8), 2411–2429. https://doi.org/10.5194/bg-12-2411-2015

Tang, J., Dietzel, M., Böhm, F., Köhler, S. J., & Eisenhauer, A. (2008). Sr^{2+}/Ca^{2+} and $^{44}Ca/^{40}Ca$ fractionation during inorganic calcite formation: II. Ca isotopes. *Geochimica et Cosmochimica Acta*, *72*(15), 3733–3745.

Tesoriero, A. J., & Pankow, J. F. (1996). Solid solution partitioning of Sr^{2+}, Ba^{2+}, and Cd^{2+} to calcite. *Geochimica et Cosmochimica Acta*, *60*(6), 1053–1063.

Venegas, S. A., & Mysak, L. A. (2000). Is there a dominant timescale of natural climate variability in the Arctic? *Journal of Climate*, *13*(19), 3412–3434.

Weiner, S., & Dove, P. M. (2003). An overview of biomineralization processes and the problem of the vital effect. *Reviews in Mineralogy and Geochemistry*, *54*(1), 1–29.

Weldeab, S., Lea, D. W., Schneider, R. R., & Andersen, N. (2007). 155,000 Years of West African monsoon and ocean thermal evolution. *Science*, *316*(5829), 1303–1307. https://doi.org/10.1126/science.1140461

Weldeab, S., Lea, D. W., Oberhänsli, H., & Schneider, R. R. (2014). Links between southwestern tropical Indian Ocean SST and precipitation over southeastern Africa over the last 17 kyr. *Palaeogeography, Palaeoclimatology, Palaeoecology*, *410*, 200–212.

Wheeler, S. G., Russell, A. D., Fehrenbacher, J. S., & Morgan, S. G. (2016). Evaluating chemical signatures in a coastal upwelling region to reconstruct water mass associations of settlement-stage rockfishes. *Marine Ecology Progress Series*, *550*, 191–206.

Uhle, M. E., Macko, S. A., Spero, H. J., Engel, M. H., & Lea, D. W. (1997). Sources of carbon and nitrogen in modern planktonic foraminifera: the role of algal symbionts as determined by bulk and compound specific stable isotopic analyses. *Organic Geochemistry*, *27*(3–4), 103–113.

Urey, H. C., Lowenstam, H. A., Epstein, S., & McKinney, C. R. (1951). Measurement of paleotemperatures and temperatures of the Upper Cretaceous of England, Denmark, and the southeastern United States. *Geological Society of America Bulletin*, *62*(4), 399–416.

Van Dijk, I., Mouret, A., Cotte, M., Le Houedec, S., Oron, S., Reichart, G.-J., et al. (2019). Chemical heterogeneity of Mg, Mn, Na, S, and Sr in benthic foraminiferal calcite. *Frontiers in Earth Science*, *7*, 281.

Vázquez Riveiros, N., Govin, A., Waelbroeck, C., Mackensen, A., Michel, E., Moreira, S., et al. (2016). Mg/Ca thermometry in planktic foraminifera: Improving paleotemperature estimations for *G. bulloides* and *N. pachyderma* left. *Geochemistry, Geophysics, Geosystems*, *17*(4), 1249–1264.

Vetter, L., Spero, H. J., Eggins, S. M., Williams, C., & Flower, B. P. (2017). Oxygen isotope geochemistry of Laurentide ice-sheet meltwater across Termination I. *Quaternary Science Reviews*, *178*, 102–117. https://doi.org/10.1016/j.quascirev.2017.10.007

Yu, J., & Elderfield, H. (2007). B/Ca in planktonic foraminifera as a proxy for surface seawater pH, *22*. https://doi.org/10.1029/2006PA001347

SUPPLEMENTARY MATERIALS

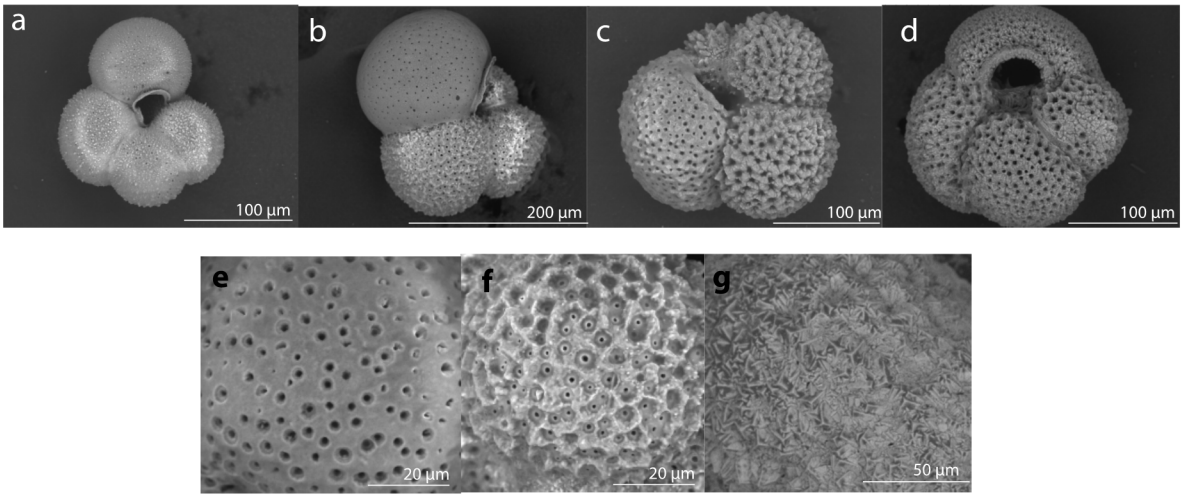

Figure S1. Scanning electron micrographs of cultured *N. pachyderma* demonstrating stages of calcification. Specimen in (a) contains only lamellar calcite and released gametes in culture with no evidence of crusting. Specimen (b) illustrates a very newly calcified F-chamber, with the earlier chambers starting to thicken. (c) shows early crust calcite on all chambers, and (d) is fully crusted and is comparable to specimens found in the fossil record. Higher magnification of (e) smooth lamellar calcite with round pores, (f) thicker lamellar calcite

with ridges and a more reticulate morphology, and (g) is a fully crusted specimen with distinct euhedral calcite and no visible pores.

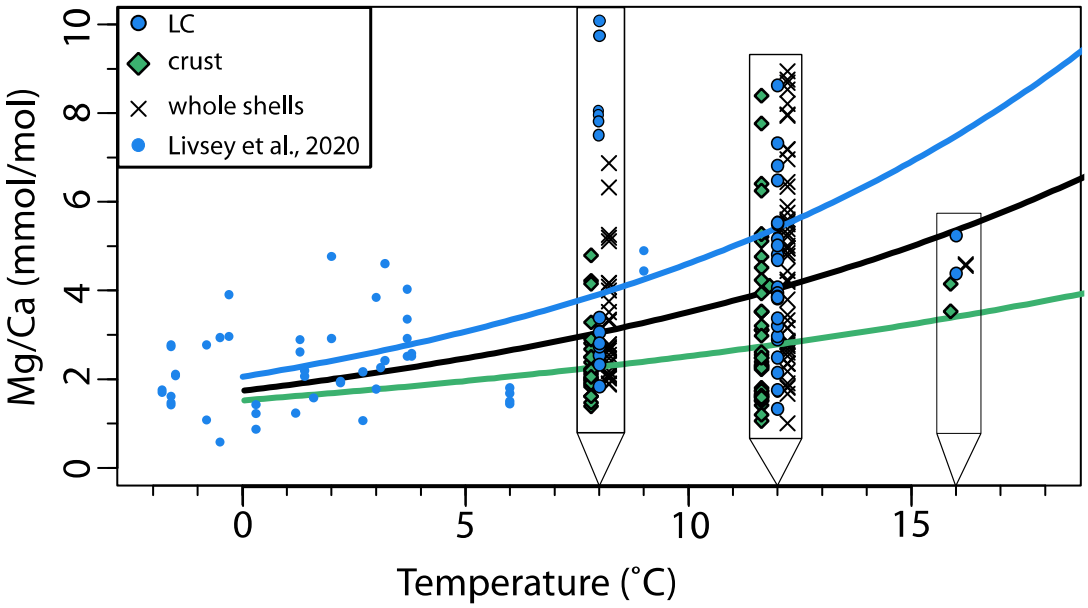

Figure S2. Plot of Mg/Ca (mmol/mol) versus temperature (ºC) from LA-ICPMS analyses on *N. pachyderma*. Data from Figure 4 supplemented with the whole shell values (combined LC and crust grown in the laboratory from single ablation profiles) in black x's and the crust results shown in green diamonds. Mg/Ca:temperature regressions for each of the three "types" of calcite (LC, crust, and whole) are shown in solid lines. Due to the large number of data points at 8, 12, and 16 ºC, the x-axis for these three temperatures is expanded slightly as indicated by the black rectangles.

Table S1. LA□ICPMS operating procedures and data reduction parameters.

ICPMS: Agilent 7700x	**Data reduction: LAtools**
RF Power: 1350 W	Despiking data: exponential decay and signal smoothing
Argon (carrier) gas flow: 0.95 – 1.0 L/min	
Ar coolant gas flow: 15 L/min	Background correction: 1D interpolation
Ar auxiliary gas flow: 1 L/min	Calibration: NIST 610-612
Dwell time per mass: 20-40 ms	Internal standard: ^{43}Ca
Total sweep time: 240 s	Filters: Sr/Ca
Laser-ablation system: UV Excimer Laser	
Energy density (fluence): 0.87-1.44 J/cm^2	
He gas flow: 1.05 L/min	
Laser repetition rate: 5 Hz	
Laser spot size: 40 µm square spot	
ThO+/Th+: <0.4%	

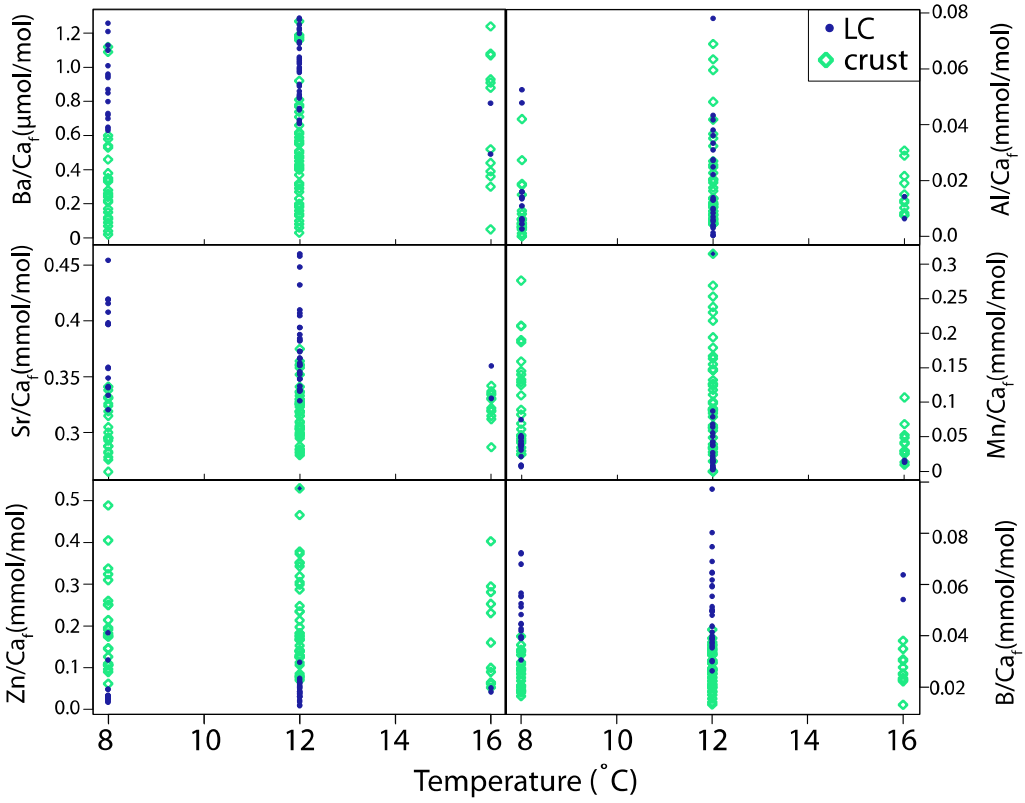

Figure S3. Plot of B/Ca (mmol/mol), Ba/Ca (μmol/mol), Al/Ca (mmol/mol), Mn/Ca (μmol/mol), Mg/Ca (mmol/mol), Sr/Ca (mmol/mol), and Zn/Ca (mmol/mol) in *N. pachyderma* foraminiferal calcite versus experimental seawater temperature (ºC). Crust calcite is shown in empty green diamonds, and LC in solid blue dots. Each point represents the average of one profile through each respective domain.

Table S2. Ablation times measuring the crust and lamellar calcite (sec) from selected *N. pachyderma* shells to calculate the proportion of each domain for individual ablation profiles.

Sample	crust (sec)	LC (sec)	%crust
3_3	9.40	10.79	**46.55**
3_3	6.61	32.02	**17.12**
3_3	5.22	13.57	**27.78**
3_5	9.40	5.92	**61.37**
3_5	8.35	6.96	**54.55**
3_17	10.44	9.75	**51.73**
3_17	20.88	11.14	**65.22**
3_18	13.92	71.00	**16.39**
3_42	29.24	25.76	**53.16**
3_42	15.31	29.58	**34.11**
3_47	12.88	32.02	**28.68**
3_47	2.09	24.36	**7.90**
3_48	10.79	15.31	**41.33**
3_48	17.75	27.50	**39.23**
3_58	14.62	53.25	**21.54**
3_62	12.18	23.67	**33.98**
3_62	4.52	11.14	**28.89**
3_64	10.09	12.53	**44.62**
3_65	10.44	19.84	**34.48**
3_66	8.70	40.03	**17.86**
3_66	11.49	27.15	**29.73**
3_67	13.92	13.23	**51.28**
4_11	7.66	10.09	**43.14**
4_11	17.06	24.71	**40.83**
4_12	6.96	6.61	**51.28**
4_12	7.31	19.84	**26.93**
4_18	7.31	17.75	**29.17**
4_18	8.35	13.57	**38.10**
4_18	8.35	9.40	**47.06**
4_18	9.40	11.48	**45.00**
4_38	3.48	24.71	**12.35**
4_38	6.61	25.41	**20.65**
4_64	33.42	17.40	**65.76**
4_64	30.98	26.80	**53.61**
4_64	14.97	28.19	**34.68**
4_69	5.57	6.26	**47.06**
4_69	5.22	6.27	**45.45**
4_69	16.01	9.75	**62.16**
4_70	6.96	7.31	**48.78**
4_70	13.58	3.48	**79.59**
4_70	15.66	9.05	**63.38**
4_70	11.14	12.53	**47.06**
4_71	13.57	16.36	**45.35**
4_71	11.14	5.57	**66.66**
4_71	19.14	6.61	**74.33**
		average	**42.1**

Table S3. Statistical coefficients comparing trace element concentrations from different domains in individual foraminifera. Values include Kruskal-Wallis (K-W) χ^2 and p-values, and Dunn's adjusted p-values between each of the three domains for trace elements that had significant K-W p-values. Statistically significant values denoted by an asterisk (*).

Trace element	K-W χ^2	K-W p-value	Dunn's LC:crust	Dunn's ocean:crust	Dunn's LC:ocean
B/Ca	18.6	0.0001*	0.0004*	0.0005*	0.417
Mg/Ca	22.62	$1e^{-5}$*	0.0001*	0.0000*	0.448
Al/Ca	15.18	0.0005*	0.58	0.0015*	0.052*
Mn/Ca	14.47	0.0007*	0.0025*	0.02*	0.006*
Zn/Ca	40.27	$1.8e^{-9}$*	$3.8e^{-9}$*	0.31	$3.8e^{-9}$*
Sr/Ca	202.56	0.00*	0.00*	0.00*	0.0001*
Ba/Ca	18.6	0.000009*	0.0008*	0.00005*	0.84

Table S4. Residual standard deviation for each TE/Ca for the crust (C) and lamellar calcite (LC) domains. Also included are the mean TE/Ca values $\pm 2\sigma$ for the crust and LC.

Trace element	max RSD% C	min RSD% C	max RSD% LC	min RSD% LC	mean crust	mean LC
B/Ca	80.24	11.14	54.1	7.08	0.00267 ± 0.001	0.051 ± 0.029
Mg/Ca	88.82	0.85	59.12	3.45	2.885 ± 0.88	6.02 ± 8.56
Al/Ca	230.85	4.71	264.59	13.43	0.017 ± 0.00223	0.15 ± 1.65
Mn/Ca	117.8	15.25	111.23	5.58	0.0105 ± 0.0069	0.034 ± 0.052
Zn/Ca	147.62	3.05	90.31	1.99	0.0205 ± 0.0123	0.45 ± 0.06
Sr/Ca	56.07	2.69	28.11	0.43	1.84 ± 0.889	0.36 ± 0.17
Ba/Ca	72.32	0.58	36.23	1.66	1.16 ± 0.675	2.44 ± 2.14

Table S5. Statistical values calculated for the relationships between TE/Ca in foraminiferal calcite and the seawater temperature for the crust, LC, and whole shells. Values include the Pearson product moment correlations (p-value), adjusted r^2 on the regressions, and the correlation coefficients (cc). Statistically significant p-values are denoted by an asterisk (*).

Trace element	crust p-value	LC p-value	whole p-value	crust r^2	LC r^2	whole r^2	crust cc	LC cc	whole cc
B/Ca	0.88	0.68	0.48	0.013	0.02	0.004	0.016	0.06	-0.06
Al/Ca	0.046*	0.93	0.13	0.041	0.027	0.012	0.23	-0.13	0.14
Mn/Ca	0.04*	0.08	0.14	0.04	0.04	0.01	-0.23	-0.25	-0.13

Zn/Ca	0.53	0.87	0.71	0.008	0.02	0.007	-0.07	0.025	0.03
Sr/Ca	0.009*	0.46	0.92	0.07	0.02	0.008	0.29	-0.11	0.009
Ba/Ca	0.008*	0.71	0.20	0.07	0.02	0.005	0.29	0.05	0.113

Table S6. Measured mean shell $Ba/Ca_{calcite}$ values for lamellar calcite (LC), crust, and ocean-grown calcite with calculated Ba/Ca_{sw} using D_{Ba} from Fehrenbacher et al., 2018. Mean and ±2SD for each domain of calcite also included.

Calcite domain	Sample	Mean shell $Ba/Ca_{calcite}$	Calculated Ba/Ca_{sw} using D_{Ba} = 0.11	average Ba/Ca_{sw} for domain	±2SD
LC	3_3_3	0.82	7.43		
LC	3_5_2	0.96	8.76		
LC	3_12_3	0.72	6.58		
LC	3_17_2	1.02	9.28		
LC	3_18_1	2.12	19.25		
LC	3_31_1	0.66	5.97		
LC	3_33_3	3.09	28.09		
LC	4_38_3	1.68	15.23		
LC	3_42_2	1.25	11.37		
LC	3_47_4	2.52	22.87		
LC	3_48_2	0.75	6.85		
LC	3_58_3	1.63	14.83		
LC	3_62_3	2.67	24.26		
LC	3_64_1	2.01	18.29		
LC	3_65_4	1.04	9.47		
LC	3_66_2	1.37	12.42		
LC	3_67_1	0.92	8.38		
LC	4_11_2	1.08	9.83		
LC	4_12_2	1.14	10.37		
LC	4_18_4	0.85	7.75		
LC	4_64_3	0.91	8.27		
LC	4_69_3	1.65	14.98		
LC	4_70_4	3.67	33.40		
LC	4_72_1	1.20	10.88		
LC	4_78_1	1.61	14.60	13.58	14.38
crust	3_3_3	0.63	5.73		
crust	3_5_2	0.87	7.94		
crust	3_17_2	1.95	17.70		
crust	3_18_2	0.72	6.57		
crust	3_31_3	0.59	5.32		
crust	3_42_2	0.91	8.25		
crust	3_47_2	2.39	21.68		
crust	3_48_3	0.61	5.57		
crust	3_62_2	0.89	8.08		
crust	3_58_1	0.96	8.72		
crust	3_64_4	0.83	7.54		
crust	3_65_1	1.15	10.47		

crust	3_66_3	2.59	23.58		
crust	3_67_4	0.72	6.54		
crust	3_73_3	2.07	18.83		
crust	4_11_4	0.96	8.69		
crust	4_12_3	1.00	9.10		
crust	4_18_4	0.75	6.84		
crust	4_21_3	1.08	9.85		
crust	4_38_2	0.84	7.63		
crust	4_30_4	1.25	11.37		
crust	4_33_4	2.53	23.01		
crust	4_64_3	0.75	6.85		
crust	4_69_4	0.93	8.44		
crust	4_70_4	1.10	9.97		
crust	4_71_3	0.90	8.18		
crust	4_72_1	1.21	11.03		
crust	4_72_3	1.18	10.71		
crust	4_78_2	1.17	10.66	10.51	10.42
ocean	4_4_2	1.21	10.97		
ocean	4_5_4	2.38	21.63		
ocean	4_6_4	2.91	26.49		
ocean	4_7_4	2.10	19.10		
ocean	4_8_4	1.51	13.73		
ocean	4_9_2	1.02	9.29		
ocean	4_10_2	1.28	11.62		
ocean	4_11_4	1.39	12.68		
ocean	4_12_4	2.07	18.79		
ocean	4_13_4	1.19	10.85		
ocean	4_14_4	1.79	16.28		
ocean	4_15_4	1.22	11.09		
ocean	4_16_4	5.09	46.26		
ocean	4_17_4	4.74	43.11		
ocean	4_18_4	1.19	10.86		
ocean	4_19_4	1.23	11.18		
ocean	4_20_4	2.31	21.02		
ocean	4_22_4	1.72	15.64		
ocean	4_23_4	1.88	17.11		
ocean	4_24_4	1.29	11.75		
ocean	4_25_3	2.07	18.82		
ocean	4_26_4	1.64	14.89		
ocean	4_27_4	0.98	8.95		
ocean	4_28_4	1.48	13.49		
ocean	4_30_2	1.33	12.11		
ocean	4_31_2	3.98	36.20		
ocean	4_32_5	1.74	15.80		
ocean	4_33_3	3.16	28.75		
ocean	4_34_4	3.57	32.41		
ocean	4_35_4	2.57	23.33		
ocean	4_36_4	3.86	35.13		
ocean	4_39_2	5.02	45.66		
ocean	4_40_4	3.72	33.83		
ocean	4_41_4	1.87	16.97		
ocean	4_42_4	3.98	36.20		
ocean	4_43_3	1.55	14.06		

ocean	4_44_4	2.88	26.17		
ocean	4_45_4	2.33	21.18		
ocean	4_46_4	1.83	16.66		
ocean	4_47_4	1.50	13.65		
ocean	4_49_4	1.34	12.22		
ocean	4_50_4	1.82	16.53		
ocean	4_51_3	2.10	19.07		
ocean	4_52_4	1.79	16.31		
ocean	4_53_4	1.65	15.03		
ocean	4_54_4	2.04	18.56		
ocean	4_56_4	3.85	35.00		
ocean	4_57_4	1.76	15.98		
ocean	4_58_2	1.94	17.62		
ocean	4_59_3	4.55	41.35		
ocean	4_60_4	2.97	27.04		
ocean	4_61_4	1.86	16.94		
ocean	4_62_4	1.76	16.02		
ocean	4_63_4	3.58	32.56		
ocean	4_64_3	1.89	17.18		
ocean	4_65_4	0.96	8.72		
ocean	4_66_4	1.67	15.14		
ocean	4_67_4	1.38	12.54		
ocean	4_68_4	1.31	11.92		
ocean	4_69_4	3.97	36.06		
ocean	4_70_4	4.76	43.25		
ocean	4_71_3	2.10	19.10		
ocean	4_73_4	2.26	20.52		
ocean	4_74_4	1.59	14.48		
ocean	4_75_3	1.78	16.21		
ocean	4_76_4	2.11	19.20		
ocean	4_77_4	1.16	10.54		
ocean	4_78_4	4.52	41.10		
ocean	4_79_4	2.11	19.15		
ocean	4_81_5	2.90	26.38		
ocean	4_82_4	1.75	15.94		
ocean	4_83_4	1.02	9.30		
ocean	4_84_4	0.89	8.08		
ocean	4_85_4	2.14	19.47		
ocean	4_86_4	2.32	21.11	20.39	19.90

Table S7. Ranges of residual standard deviations (RSD%) for Mg/Ca of the crust and LC in foraminifera grown at different temperatures (ºC).

	8 ºC	**12 ºC**	**16 ºC**
Mg/Ca crust	2.25- 88.82	10.98- 73.82	0.85- 63.06
Mg/Ca LC	4.26-40.77	3.45-59.11	25.03

Ch. 3: Fluctuating oxygen isotope signatures of Lake Agassiz meltwater through the Younger Dryas Event

Caitlin M. Livsey[1], Reinhard Kozdon[2], Hubert Vonhof[3], Tessa M. Hill[1], Howard J. Spero[1]

[1]*Department of Earth and Planetary Sciences, University of California Davis, Davis, CA 95616, USA.*

[2]*Department of Earth and Environmental Sciences and Lamont–Doherty Earth Observatory of Columbia University, 61 Route 9W, Palisades, NY 10964, USA.*

[3]*Department of Climate Geochemistry, Max Planck Institute for Chemistry, Mainz, Germany*

Summary

Quantifying patterns of freshwater outflow from the Arctic Ocean during deglaciation periods is critical to understanding the relationship between a warming climate and melting of Arctic ice. Throughout the last deglaciation there is evidence for multiple large inputs of ice-sheet derived meltwater into the global oceans, including a significant pulse at ~11,500 years ago in the Northern Hemisphere. This event was likely caused by the draining of glacial Lake Agassiz into the Arctic Ocean via the Mackenzie River that triggered a slowdown of global ocean circulation and initiated the Northern Hemisphere cold interval known as the Younger Dryas. However, the evolution of meltwater chemistry, route, and discharge rates in the Arctic Ocean associated with the Younger Dryas meltwater event remain poorly constrained. We combine trace element measurements from laser ablation inductively coupled plasma mass spectrometry with $\delta^{18}O_{calcite}$ analyses on *Neogloboquadrina pachyderma* shells to reconstruct the $\delta^{18}O$ of Lake Agassiz-derived Mackenzie River meltwater. Notably, these results indicate that the geochemistry of the meltwater entering the Arctic Ocean varies throughout the Younger Dryas event, revealing the inaccuracy of current model simulations that are restricted to using a single $\delta^{18}O$ value for meltwater. Further, we illustrate evidence that the meltwater pulse was not continuous throughout the interval, with at least one cessation of drainage that is linked to a shift in the $\delta^{18}O$ of the meltwater. Overall, the time-resolved isotopic evolution of meltwater in the Arctic Ocean through the Younger Dryas reveals the complexities of this meltwater pulse, which have important implications for our understanding of volumes and rates of freshwater discharge into the North Atlantic during past climate warming and provides insights on the locations and timing of melting during the Younger Dryas event.

The Arctic Ocean is very sensitive to changes in Earth's climate and is simultaneously one of the least studied oceanic regions of our planet (e.g., Johannessen et al., 2004; Stein, 2008, 2011; Jeffries et al., 2003). Paleoclimate reconstructions from this region are critically needed to understand the contribution and global implications of rapid inputs of cold, dense water flowing from the Arctic Ocean into the North Atlantic (e.g. Broecker, 1997; Serreze et al., 2000; Venegas and Mysak, 2000; Johannessen et al., 2004). The Arctic Ocean plays a unique role in global ocean circulation, primarily through the production of North Atlantic Deepwater (NADW). The cold and dense NADW forms in the relatively restricted Arctic Ocean basin as a result of the significant contribution of freshwater from river runoff as well as the stratification of the water column due to production of sea ice (Nørgaard-Pedersen et al., 2003; Kerr, 2012). The formation rate and volume of NADW directly influences the Atlantic Meridional Overturning Circulation (AMOC), which in turn modulates heat exchange between the tropics and the poles (Rooth, 1982; Broecker et al., 1989; Lambeck et al., 2002; Peltier, 2007). Previous paleoclimate studies indicate that changes in AMOC significantly impact global climate (Broecker, 1994; Alley, 2000; McManus et al., 2004), and therefore investigating the impact of meltwater inputs into the Arctic Ocean is vital to understand what to expect as our planet continues to warm due to anthropogenic forcing.

The Younger Dryas (YD; ~11.2-12.4 cal kyr) was an abrupt Northern Hemisphere cold interval within the last deglaciation that is hypothesized to have been initiated by the weakening of AMOC triggered by the sudden input of a large volume of meltwater (Rooth, 1982; Keigwin et al., 1991; Hughen et al., 1998; Muscheler et al., 2000; Clark et al., 2001; Teller et al., 2002; McManus et al., 2004). The exact routes and subsequent drainage locations of the YD meltwater pulse into the global ocean are still contested (Broecker et al., 1989; Lowell et al., 2005; Teller et al., 2005; Fisher, 2020), but evidence of meltwater reaching the central Arctic Ocean at this time

indicates that a substantial volume of freshwater drained through the Mackenzie River (Bauch et al., 2001; Hall and Chan, 2004; Keigwin et al., 2018). While we acknowledge the possibility that there were multiple outlets of meltwater draining preceding the YD, our data reveals strong evidence of multiple episodes of significant drainage into the Arctic Ocean throughout this time.

Ascertaining the $\delta^{18}O$ of the meltwater entering the Arctic Ocean through the Younger Dryas meltwater pulse will aid in elucidating the source, volume, and rates of drainage. The $\delta^{18}O$ of meltwater ($\delta^{18}O_{mw}$) is controlled by which ice sheet is contributing meltwater, which regions of the ice sheets are melting, and local hydrology. Many climate models have attempted to replicate the YD event through "hosing" experiments (i.e. Peltier et al., 2006; Tarasov and Peltier, 2005, 2006; Condron and Windsor, 2012), but are limited by only being able to constrain the amount or $\delta^{18}O$ signature of the freshwater, and therefore cannot determine the high-resolution cadence of meltwater dynamics. Further, the few isotope-enabled models that exist (Carlson, 2009; Liu et al., 2012) assume a single value for the oxygen signature of the freshwater input, which restricts the ability for models to characterize complexities within the event. While some models are complex enough to handle variatble $\delta^{18}O$ during a drainage event, they are inhibited by the lack of existing data providing estimates of $\delta^{18}O$ through time. The $\delta^{18}O_{mw}$ at higher resolution during the YD can be used to reconstruct the source water history of Lake Agassiz as well as constrain the regions of the Laurentide ice sheet that were contributing to Mackenzie River outflow during the thousand-year long YD event.

Here we present meltwater $\delta^{18}O$ reconstructions throughout the duration of the Younger Dryas meltwater pulse using *Neogloboquadrina pachyderma* shells from the AOS94b-17 box core on the Mendeleev Ridge (Figure 1). This study builds upon previous work showing that

paired Ba/Ca and $\delta^{18}O$ measurements made on numerous individual planktic foraminifera shells from a sediment population can be used to produce $\delta^{18}O$-salinity relationships and calculate the freshwater $\delta^{18}O$ during a meltwater release event (Vetter et al., 2017). Meltwater $\delta^{18}O$ from a sediment interval reflects the source(s) of freshwater in the Arctic from the Laurentide ice sheet, which can vary with melting source regions of the ice sheet and local hydrology. In areas of the ocean in proximity to major river outflows, Ba/Ca of the seawater can be used to calculate salinity, since barium has been shown to act conservatively at salinities greater than 15 psu (Coffey et al., 1997; Guay and Faulkner, 1997).

Paired Ba/Ca and $\delta^{18}O_{calcite}$ results from planktic foraminifera in core AOS94b-17 provide unique insights into the evolution of the meltwater pulse chemistry reaching the central Arctic Ocean throughout the Younger Dryas. Measured Ba/Ca, calculated salinity, and $\delta^{18}O$ of calcite in core AOS94b-17 illustrate the notable decreases in $\delta^{18}O_{sw}$ and salinity and coincident increase in Ba/Ca, which together indicate significant riverine input in the Arctic Ocean between ~20.5 and 10.5 cm (Figure 2). We interpret the source of the riverine input to be ice sheet meltwater that accumulated in Lake Agassiz before it entered the Mackenzie River and eventually drained into the Arctic Ocean based on the correlative drop in Lake Agassiz water levels indicated by paleo-strandlines (Broecker et al., 1989; Breckenridge, 2015). Our results on individual *N. pachyderma* shells build upon previous data from bulk sediments and illustrate that during the meltwater interval, the ranges in both Ba/Ca and $\delta^{18}O_{calcite}$ increase relative to samples outside the event (Hall and Chan, 2004). As trace element geochemistry (TE/Ca) both within and between single shells is highly variable (e.g., Katz et al., 2010), we present mean shell TE/Ca, or, when specified, mean TE/Ca for all shells within single depth intervals.

The $\delta^{18}O_{calcite}$ values range from an average of 1.91‰ outside of the meltwater event, to a minimum value of 0.1‰ at 11.4 ky. During the six samples within the meltwater pulse as indicated by elevated Ba/Ca, the ranges of Ba/Ca and $\delta^{18}O_{calcite}$ are 2.19 μmol/mol and 2.71‰, respectively, while the intervals before and after the event have ranges of 1.19 μmol/mol and 1.83‰. Larger variability in Ba/Ca and $\delta^{18}O_{calcite}$ in the absence of a coincident increase in the range of individual Mg/Ca (Table S1) indicates that the hydrologic cycle (i.e. salinity) was extremely dynamic throughout the event while the temperatures were relatively constant. The average Ba/Ca-calculated salinity within the meltwater pulse is 33.46 psu, with a range of 3.79 psu (Table S1).

Paired Ba/Ca-calculated salinity and $\delta^{18}O_{sw}$ for each sample (composed of 2-4 individual shells) from each depth interval indicate the relative influence of meltwater on the salinity during each time interval (Figure 3). The strong linear relationships between $\delta^{18}O_{sw}$ and salinity reveal that between 14.4 and 10.8 ka, the salinity in the Central Arctic Ocean was primarily controlled by the input of fresh meltwater through the Mackenzie River (Figure 3). Further, the y-intercepts of the regressions provide the $\delta^{18}O$ signature of the freshwater endmember, which is assumed to be LIS meltwater (Figure 4; Table S2). In the five analyzed intervals before and after the meltwater pulse (0.5, 4.5, 26.5, 30.5, and 35.5 cm), $\delta^{18}O_{sw}$ and Ba/Ca-calculated salinity do not covary, indicating that meltwater does not exert a strong control on salinity during these intervals, and Ba/Ca_{shell} records ambient Ba/Ca_{sw} (Table S2; Figure S2).

Reconstructing meltwater pulse(s)

The few isotope-enabled models that have been utilized to investigate the impact of Laurentide Ice Sheet (LIS) meltwater on global climate assume a constant $\delta^{18}O_{mw}$ value throughout

the event, with typical estimated $\delta^{18}O$ around -25 or -35‰ (Aharon, 2003, 2006; Hill et al., 2006; Obbink et al., 2010). Our data reveals that the relationship between salinity and $\delta^{18}O_{sw}$ is not constant through time, suggesting that the $\delta^{18}O$ of meltwater entering the Arctic Ocean is heterogeneous through the YD event (Figure 4). The heterogeneity of meltwater $\delta^{18}O$ throughout the meltwater event has direct implications on previous estimates of the volume of meltwater that entered the global ocean during the YD. Reconstructed $\delta^{18}O$ of meltwater using $\delta^{18}O_{calcite}$-calculated $\delta^{18}O_{sw}$ and Ba/Ca-calculated salinities vary between -24.4 and -9.5‰ from the initial appearance of the meltwater pulse to the end of the event (Figure 4; Table S2). The calculated $\delta^{18}O_{mw}$ values lie within the model estimated $\delta^{18}O_{ice}$ signatures of different regions within the LIS, with most depleted values aligning with reconstructions of the higher latitude/elevation regions (Vinther et al., 2009; Ferguson and Jasechko, 2015).

The overall trend toward progressively more enriched $\delta^{18}O_{mw}$ throughout the event is overprinted by smaller-scale oscillations, with a total range in $\delta^{18}O$ values of 14.9 ($\pm$0.26)‰ (Figure 4). The progressive relative enrichment in $\delta^{18}O$ can be explained by the melting and subsequent draining of different regions of the LIS that have distinct $\delta^{18}O$ signatures as a result of the varying conditions at which the ice formed due to Rayleigh Fractionation (Craig, 1961; Oerlemans, 1982; Bowen and Wilkinson, 2002). More fractionation of $\delta^{18}O$ occurs as moisture sources move towards higher altitudes and latitudes, so the ice in these regions will consist of the lowest $\delta^{18}O$ relative to the remainder of the ice sheet (Masson-Delmotte et al., 2008).

The earliest meltwater signal occurs at 20.5 cm and has a calculated meltwater $\delta^{18}O$ signature of -24.4 ($\pm$0.10)‰, which is the most depleted in $\delta^{18}O$ relative to the other meltwater intervals (Figure 4). This can be explained by high altitude ice melting during the Bølling-Allerød

warm interval and accumulating meltwater in Lake Agassiz, which subsequently drained through the Mackenzie River after a catastrophic ice dam collapse. This pulse of meltwater eventually entered the North Atlantic, likely following the path outlined in Condron and Windsor (2012), which ultimately triggered a weakening of the AMOC. The Northern Hemispheric cooling associated with a weaker AMOC likely resulted in the re-freezing of the high altitude (low $\delta^{18}O$) regions, while the lower elevation meltwater continued accumulating in Lake Agassiz. Therefore, the general trend towards less depleted $\delta^{18}O$ through the YD can be explained by the transition from initial Lake Agassiz meltwater, to subsequent prolonged melting of lower elevation regions of the LIS.

Further insights into the evolution of the YD meltwater pulse were revealed in targeted ^{14}C analyses on foraminifera based on their Ba/Ca concentrations (Table S3). Two discrete Ba/Ca populations of *N. pachyderma* (Kruskal-Wallis p-value$\gg$0.05) within sample 20.5 cm are offset in ^{14}C age by ~10 ka, suggesting that there may have been a hiatus in meltwater input after an initial pulse (Table S4). However, while isotope and Ba/Ca data indicate that the 20.5 cm interval is consistent with meltwater influence, we acknowledge that the ^{14}C age is difficult to interpret. The subset of samples with higher Ba/Ca record an older ^{14}C age, indicating that there was a period when the Western Arctic Ocean was experiencing significant contribution of river runoff, followed by a period with no meltwater signal, followed by elevated [Ba] again. It is probable that the calculated age for the initial meltwater pulse (24.5 ka) is erroneously old, as it is a result of mixing of water that was accumulating in Lake Agassiz throughout the deglaciation, and therefore the reservoir correction would be much older than for the subsequent samples. Therefore, this multi-proxy geochemical approach using *N. pachyderma* populations from the Arctic Ocean provides the opportunity to reconstruct salinity, $\delta^{18}O_{sw}$, $\delta^{18}O_{mw}$, and even tease apart multiple age

populations within a depth interval. The 20.5 cm interval was the only one analyzed using multiple ^{14}C samples separated by Ba/Ca concentrations, but a similar range in Ba/Ca from other intervals suggests similar patterns may be present throughout the YD (Table S1).

Superimposed over the general trend towards more enriched $\delta^{18}O_{mw}$ through the YD event are smaller oscillations that range between ±1.3 and 11.8‰ in $\delta^{18}O$ (Figure 4; Table S3). The mechanism behind the rapid shifts in $\delta^{18}O_{mw}$ is not readily evident, but it is likely that there are multiple reservoirs of meltwater that are contributing different amounts of water through the event. One potential explanation is that Lake Agassiz consisted of numerous disparate basins similar to the geometry suggested in Condron and Windsor (2012). Each of the individual basins likely had distinct geochemistries based on their respective drainage basins and therefore, through time, the meltwater $\delta^{18}O$ reflects the progressive draining of the various reservoirs. Another potential explanation is that the oscillations are caused by seasonal variations in melting patterns. Enhanced warming during the summer months promotes melting of higher elevation/latitude ice, resulting in a more depleted $\delta^{18}O_{mw}$ signal. The re-freezing of these regions during the colder winter months led to relatively enriched $\delta^{18}O_{mw}$ until the northern hemisphere warmed again in the summers. While it is unlikely that we would be able to resolve a seasonal signal in the individual foraminiferal samples, the influence of melting and re-freezing of regions on a seasonal cycle could be resolved when looking at the variation in individual foraminifera analyses (IFA) within larger populations (as demonstrated in Groeneveld et al., 2019).

Broad regional implications

Quantifying the time-resolved geochemistry of meltwater draining into the Arctic Ocean through the Younger Dryas provides vital insights into the dynamics of the deglaciation in the Northern Hemisphere. The oscillations of meltwater $\delta^{18}O$ entering the Arctic Ocean revealed by paired $\delta^{18}O_{sw}$ and Ba/Ca results from *N. pachyderma* shells present an unprecedented record of meltwater variability within a single event. These results illustrate the geochemical complexity and dynamic nature of the YD meltwater pulse and suggest that other meltwater pulses in the geologic record should be explored similarly. Furthermore, the time-resolved $\delta^{18}O_{mw}$ results have the potential to greatly improve isotope-enabled climate models and provide insights into volumes, timing, and routes of meltwater drainage. Mechanisms and details of rapid climate changes associated with meltwater inputs, such as the 8.2 ka event and MWP 1a at ~19 ka, are also widely debated, and are prime candidates for analogous investigation (Alley, 2000; Lambeck et al., 2002; Broecker, 2006).

Specifically, the calculated $\delta^{18}O_{mw}$ values can be used in combination with marine sedimentary $\delta^{18}O_{calcite}$ measurements to determine the time-resolved volumes of meltwater present at different locations. Site-specific mixing models that span the meltwater interval can be used to identify the proportion of meltwater at any given location and time. For example, $\delta^{18}O_{calcite}$ results from key locations related to global circulation, such as the Fram Strait, can be re-evaluated to calculate volumes of freshwater entering the North Atlantic through the event. Further, isotope-enabled climate models can directly input these calculated $\delta^{18}O_{meltwater}$ values into their simulations to track freshwater movement and subsequent oceanographic changes in the global oceans.

Multi-proxy geochemical analyses on planktic foraminifera reveal the isotopic evolution of meltwater entering the Arctic Ocean during the Younger Dryas event, significantly revising our previous understanding of the event. Understanding the impacts of meltwater on global ocean

circulation in the past will provide a more extensive view of the complexities of meltwater pulses to refine our future predictions. Further, these results elucidate the sensitivity of the Northern Hemispheric oceans to input of low-density meltwater. The apparent irregularity in timing and cadence of meltwater coincident with a shift in geochemistry suggests that meltwater pulses are much more complex than previously assumed and require to be evaluated further.

Materials and Methods

Box core AOS 94b-17 was collected from the Mendeleev Ridge (81 15.91'N, 178 58.05'E; 2217 m water depth) during the 1994 Trans-Arctic cruise (Figure 1). Core processing and initial sampling at 1 cm resolution are described in Osterman, 1998. For this study, individual *Neogloboquadrina pachyderma* were picked from the dried 125 μm fraction of selected depth intervals and cleaned to remove remnant organics using an oxidative 1:1 solution of 35% H_2O_2:0.1N NaOH in conjunction with 8 rinses in methanol, following the method of Mashiotta et al., (1999). All cleaned *N. pachyderma* were then mounted on carbon tape and imaged using a Hitachi TM300 scanning electron microscope (SEM) in the UC Davis Department of Earth and Planetary Sciences (Figure S1 for representative images). The resulting BSE images were visually reviewed to determine if any non-calcite materials were present on the shells and to note the orientation of the shells for subsequent analyses.

Settings and procedure for laser ablation inductively coupled plasma mass spectrometer (LA-ICPMS) trace element analyses and data reduction process were described previously in Livsey et al., 2020. Following data reduction, Ba/Ca (μmol/mol) ratios were averaged for each individual *N. pachyderma* shell and converted to salinity for each shell using a continent-specific

relationship (Vetter et al., 2017): S (psu) = 36.35(±0.008) - 1.734(±0.002)*(Ba/Ca_{shell}) (r^2 = 0.82, Eq. 2). This relationship was calculated using Ba/Ca_{shell} and salinity measurements collected in the Mississippi-Atchafalaya River system (Hanor and Chan, 1977; Joung and Shiller, 2014). As meltwater collecting in Lake Agassiz will become mixed within the glacial reservoir, we assume that the correlation between Ba/Ca and salinity during the deglaciation has not changed significantly from modern observations. Since Vetter et al. (2017) were also calculating Lake Agassiz meltwater draining from the southern outlet rather than a northern outlet, we opted to stay consistent and utilize the same relationship. We do note that this relationship utilizes the Ba/Ca_{shell} to Ba/Ca_{sw} equation determined for spinose foraminifera (Hönisch et al., 2011) rather than the equation calibrated using non-spinose foraminifera (Fehrenbacher et al., 2018). However, the slight difference in calculations would be consistent across all results, ultimately producing equivalent patterns.

Following LA-ICP-MS analysis, each shell was removed from the carbon tape using ethanol and roasted at 375°C *in vacuo* for 35 minutes to remove any remnant carbon tape. The shells were then individually weighed on a microbalance to obtain single shell masses. Samples were subsequently analyzed for $\delta^{18}O$ either as single shells on a Delta V gas bench mass spectrometer at the Max Planck Institute for Chemistry (MPIC), or 2-5 pooled shells analyzed on a common acid bath dual-inlet (CABDI) mass spectrometer at UC Davis. Two techniques were used for $\delta^{18}O$ analyses as a comparison to assess precision and accuracy, and no significant difference was identified between the two methods (Table S5; Figure 3). The CABDI method was utilized for the majority of the intervals. For the samples run via CABDI, roasted and weighed shells were grouped together by Ba/Ca, with inter-sample ranges < ~0.1 nmol/mol. Between two and five shells were pooled together to obtain masses large enough to run on the Optima CABDI,

with a combined mass ranging between 15 and 25 μg. Post-analysis, all single shell gas bench (SSGB) $\delta^{18}O$ data were averaged within samples following the same method that was used to combine the CABDI samples in order to standardize what is included in the data points in each of the two techniques.

The $\delta^{18}O_{calcite}$ results from foraminiferal shells within each measured interval were then used to calculate $\delta^{18}O_{seawater}$ using the paleotemperature equation of Kim and O'Neil (1997) and a temperature of 2ºC. We assume a calcification temperature of 2ºC, which is based on Arctic Ocean surface water temperature estimates (~-0.5-0ºC; Rudels et al., 1996) with assumed mixing with glacial lake waters, which typically are around 4ºC (Leopold, 2002). Adjusting the seawater temperature had only a negligible impact on the $\delta^{18}O_{sw}$ calculations (Table S6) and therefore 2ºC was used consistently for all intervals. The $\delta^{18}O_{sw}$ values were plotted against the Ba/Ca-calculated salinities (Eq. 2) for each sample within the depth interval (Figure 3) to identify time periods where $\delta^{18}O$ and salinity covary, indicating that the meltwater is controlling the salinity. For depth intervals within the meltwater pulse, a linear regression through the data is calculated to determine the y-intercepts of the regressions, which represent the $\delta^{18}O_{sw}$ signature when salinity is equal to 0, and therefore provide the $\delta^{18}O$ of the fresh/meltwater endmember for each time interval.

Eight intervals in box core AOS 94b-17 were previously dated using accelerator mass spectrometry ^{14}C measurements on samples containing ~2,000 individual *N. pachyderma* at Lawrence Livermore National Laboratory, Livermore, CA (Poore et al., 1999). These ^{14}C ages were corrected using a marine reservoir age of 800 years (Dyke et al., 2003) and converted to calendar years using the CALIB program (Stuiver and Reimer, 1993). Additional 14C ages were measured on the 18.5 cm and 20.5 cm intervals, and these ages were corrected and converted consistent with the previous measurements. We produced an age model using the ten ^{14}C ages

and their depths in the core to create a linear interpolation assuming constant sedimentation rates between the dated intervals (Figure S3). The original ^{14}C results on foraminifera from the 20.5 cm interval produced an age that pre-dated the YD event by ~15 kyr, but elevated Ba/Ca results indicated the presence of meltwater in the shells. Therefore *N. pachyderma* from this interval were separated into two groups by Ba/Ca concentration (using a threshold of 2 μmol/mol) and analyzed for ^{14}C separately to investigate if there were multiple age populations in this interval (Table S4).

FIGURES AND TABLES

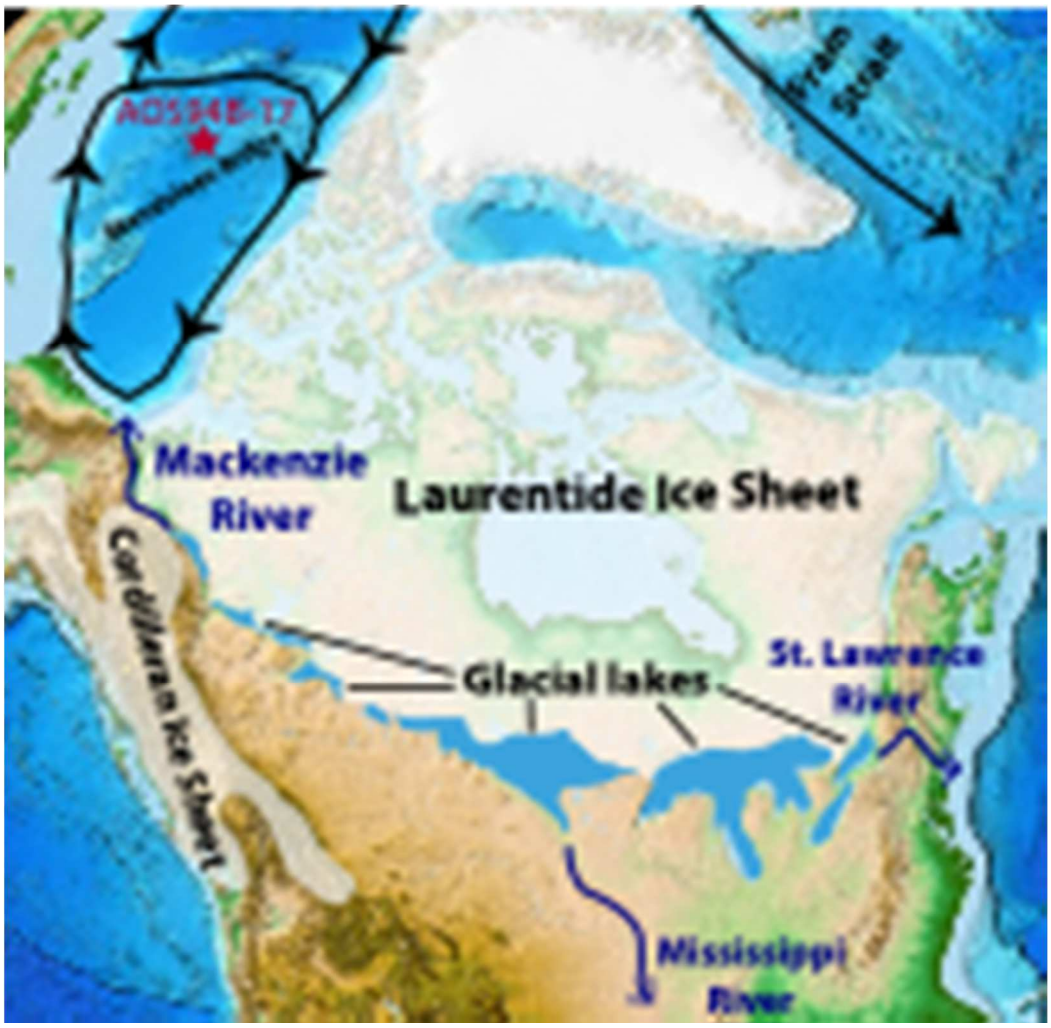

Figure 1. Map of study area with location of box core AOS94b-17 (red star), simplified cold currents (black arrows), approximate location and extent of the Laurentide and Cordilleran Ice Sheets during the Younger Dryas event (from Dyke, 2004), location of proglacial lakes (modified from Murton et al., 2010), and major river drainages with arrows indicating direction of primary drainage.

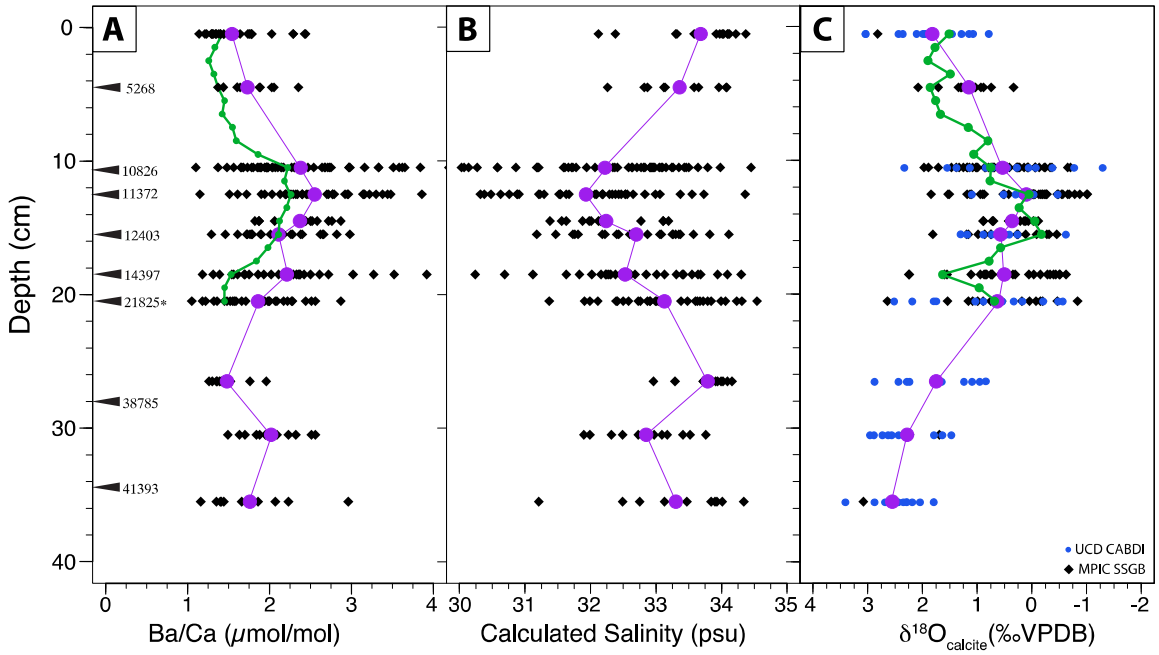

Figure 2. Ba/Ca (panel A; μmol/mol), calculated salinity (panel B; psu), and $\delta^{18}O_{calcite}$ (panel C; ‰VPDB) results from *N. pachyderma* from core AOS94b-17 with depth through core. Published AMS ^{14}C-derived ages on *N. pachyderma* from 8 depths indicated by arrows (Poore et al., 1999; Table SX). The ^{14}C age measured from depth 20.5 cm (indicated by an *) is interpreted to be within the meltwater pulse and therefore an anomalous age (more detailed information on this sample described in the methods). For each plot, black diamonds represent data from both individual samples and single shells, with the mean for each depth indicated by larger purple dots. In panel C, grouped single shells run on the UC Davis IRMS (UCD CABDI) are shown in blue dots, and single shells measured at the Max Planck Institute of Chemistry (MPIC SSGB) are shown in black diamonds. Published analyses on pooled *N. pachyderma* for Ba/Ca and $\delta^{18}O$ from Hall and Chan (2004) shown in green lines.

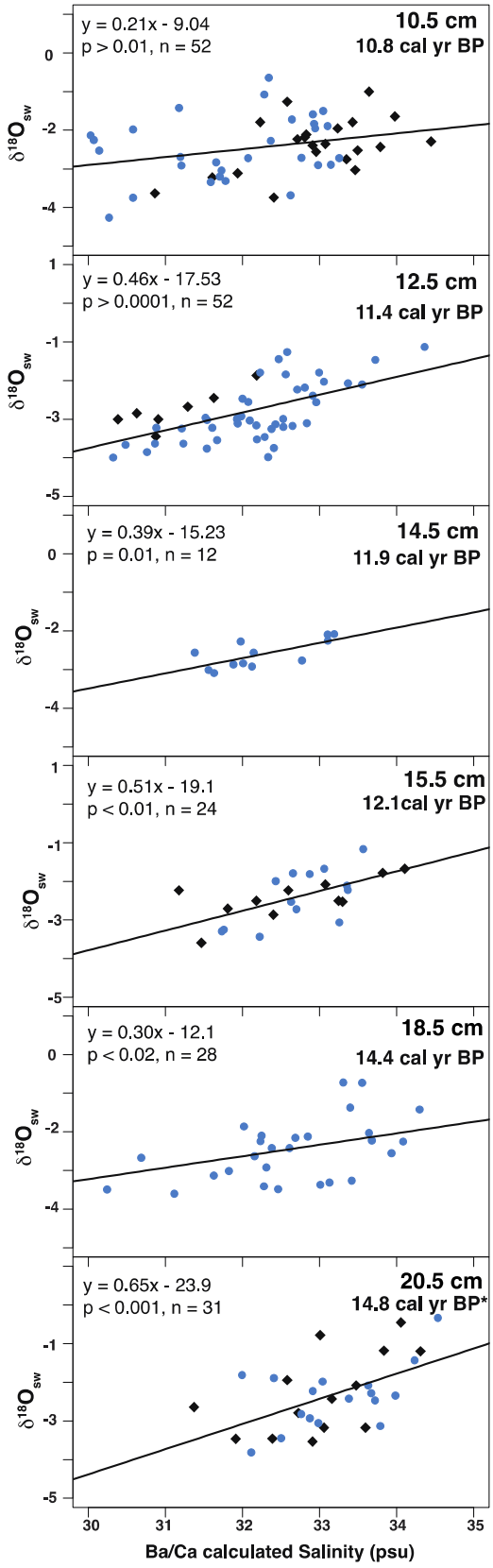
y = 0.21x - 9.04
p > 0.01, n = 52
10.5 cm
10.8 cal yr BP
y = 0.46x - 17.53
p > 0.0001, n = 52
12.5 cm
11.4 cal yr BP
y = 0.39x - 15.23
p = 0.01, n = 12
14.5 cm
11.9 cal yr BP
y = 0.51x - 19.1
p < 0.01, n = 24
15.5 cm
12.1cal yr BP
y = 0.30x - 12.1
p < 0.02, n = 28
18.5 cm
14.4 cal yr BP
y = 0.65x - 23.9
p < 0.001, n = 31
20.5 cm
14.8 cal yr BP*
δ18Osw
Ba/Ca calculated Salinity (psu)

Figure 3. Compilation of Ba/Ca calculated salinity vs. $\delta^{18}O_{sw}$ regressions for the YD meltwater pulse within AOS94b-17. Black diamonds are MPIC pooled single foraminifera data, and blue circles are CABDI results. Each plot represents a single depth interval with calculated ^{14}C ages. Equations for the linear regressions are shown in the top left corner of the plot, with the Pearson's coefficient and the number of samples (n) included for each.

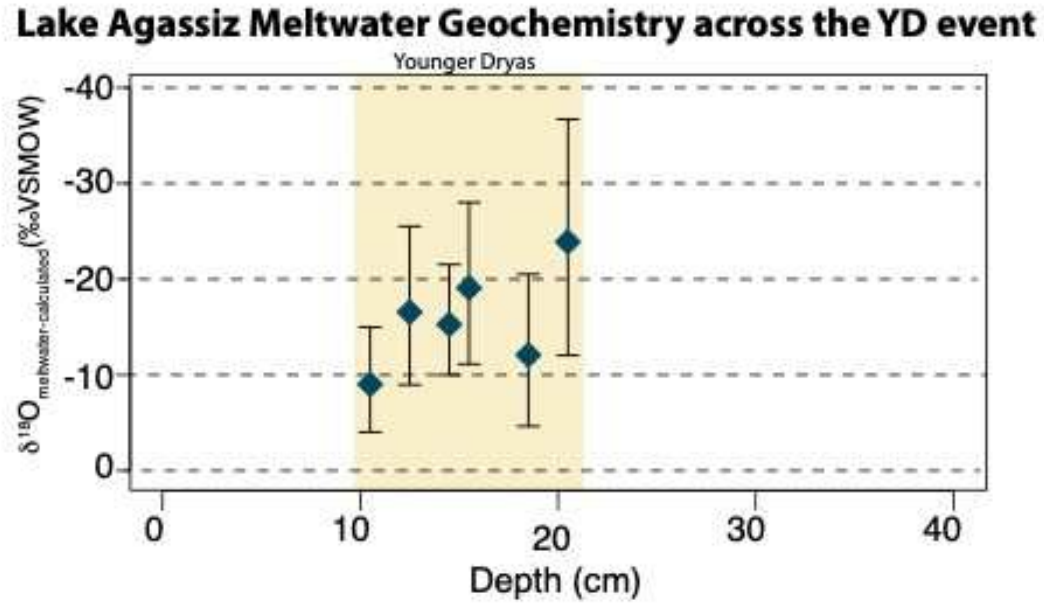

Figure 4. Depth in core vs. $\delta^{18}O_{meltwater}$ (‰VPDB) for the six intervals within the meltwater pulse shown with 2σ standard deviation. Yellow bar demarcates the YD meltwater interval.

REFERENCES

Aharon, P. (2003). Meltwater flooding events in the Gulf of Mexico revisited: implications for rapid climate changes during the last deglaciation. *Paleoceanography*, *18*(4).

Aharon, P. (2006). Entrainment of meltwaters in hyperpycnal flows during deglaciation superfloods in the Gulf of Mexico. *Earth and Planetary Science Letters*, *241*(1–2), 260–270.

Alley, R. B. (2000). Ice-core evidence of abrupt climate changes. *Proceedings of the National Academy of Sciences*, *97*(4), 1331–1334.

Bauch, H. (2001). A multiproxy reconstruction of the evolution of deep and surface waters in the subarctic Nordic seas over the last 30,000 yr. *Quaternary Science Reviews*, *20*(4), 659–678. https://doi.org/10.1016/S0277-3791(00)00098-6

Bauch, H. (2001). A multiproxy reconstruction of the evolution of deep and surface waters in the subarctic Nordic seas over the last 30,000yr. *Quaternary Science Reviews*, *20*(4), 659–678.

Breckenridge, A. (2015). The Tintah-Campbell gap and implications for glacial Lake Agassiz drainage during the Younger Dryas cold interval. *Quaternary Science Reviews*, *117*, 124–134.

Bowen, G. J., & Wilkinson, B. (2002). Spatial distribution of $\delta^{18}O$ in meteoric precipitation. *Geology*, *30*(4), 315–318.

Broecker, W. S., Kennett, J. P., Flower, B. P., Teller, J. T., Trumbore, S., Bonani, G., & Wolfli, W. (1989). Routing of meltwater from the Laurentide Ice Sheet during the Younger Dryas cold episode. *Nature*, *341*(6240), 318–321. https://doi.org/10.1038/341318a0

Broecker, W. S. (1994). Massive iceberg discharges as triggers for global climate change. *Nature*, *372*(6505), 421–424. https://doi.org/10.1038/372421a0

Broecker, W. S. (1997). Thermohaline circulation, the Achilles heel of our climate system: Will man-made CO_2 upset the current balance? *Science*, *278*(5343), 1582–1588.

Broecker, W. S., & Stocker, T. F. (2006). The Holocene CO_2 rise: Anthropogenic or natural? *Eos, Transactions American Geophysical Union*, *87*(3), 27. https://doi.org/https://doi.org/10.1029/2006EO030002

Carlson, A. E. (2009). Geochemical constraints on the Laurentide Ice Sheet contribution to Meltwater Pulse 1A. *Quaternary Science Reviews*, *28*(17–18), 1625–1630. https://doi.org/10.1016/j.quascirev.2009.02.011

Clark, P. U., Marshall, S. J., Clarke, G. K. C., Hostetler, S. W., Licciardi, J. M., & Teller, J. T. (2001). Freshwater forcing of abrupt climate changes during the last glaciation. *Science*, *293*(July), 283–287.

Coffey, M., Dehairs, F., Collette, O., Luther, G., Church, T., & Jickells, T. (1997). The behaviour of dissolved barium in estuaries. *Estuarine, Coastal and Shelf Science*, *45*(1), 113–121.

Condron, A., & Winsor, P. (2012). Meltwater routing and the Younger Dryas. *Proceedings of the National Academy of Sciences*, *109*(49), 19928 LP – 19933. https://doi.org/10.1073/pnas.1207381109

Craig, H. (1961). Isotopic Variations in Meteoric Waters. *Science*, *133*(3465), 1702 LP – 1703. https://doi.org/10.1126/science.133.3465.1702

Dyke, A., Moore, A., & Robertson, L. (2003). *Deglaciation of North America*. *Geological Survey of Canada*. https://doi.org/10.4095/214399

Fehrenbacher, J. S., Russell, A. D., Davis, C. V., Spero, H. J., Chu, E., & Hönisch, B. (2018). Ba/Ca ratios in the non-spinose planktic foraminifer *Neogloboquadrina dutertrei*: Evidence for an organic aggregate microhabitat. *Geochimica et Cosmochimica Acta*, *236*, 361–372. https://doi.org/10.1016/j.gca.2018.03.008

Ferguson, G., & Jasechko, S. (2015). The isotopic composition of the Laurentide Ice Sheet and fossil groundwater. *Geophysical Research Letters*, *42*(12), 4856–4861. https://doi.org/10.1002/2015GL064106

Fisher, T. G. (2020). Megaflooding associated with glacial Lake Agassiz. *Earth-Science Reviews*, *201*(September), 102974. https://doi.org/10.1016/j.earscirev.2019.102974

Groeneveld, J., Ho, S. L., Mackensen, A., Mohtadi, M., & Laepple, T. (2019). Deciphering the variability in Mg/Ca and stable oxygen isotopes of individual foraminifera. *Paleoceanography and Paleoclimatology*, *34*(5), 755–773.

Guay, C. K., & Falkner, K. K. (1997). Barium as a tracer of Arctic halocline and river waters. *Deep-Sea Research Part II: Topical Studies in Oceanography*, *44*(8), 1543–1569. https://doi.org/10.1016/S0967-0645(97)00066-0

Hall, J. M., & Chan, L.-H. (2004). Ba/Ca in *Neogloboquadrina pachyderma* as an indicator of deglacial meltwater discharge into the western Arctic Ocean. *Paleoceanography*, *19*(1), n/a-n/a. https://doi.org/10.1029/2003PA000910

Hanor, J. S., & Chan, L.-H. (1977). Non-conservative behavior of barium during mixing of Mississippi River and Gulf of Mexico waters. *Earth and Planetary Science Letters*, *37*(2), 242–250.

Hill, H. W., Flower, B. P., Quinn, T. M., Hollander, D. J., & Guilderson, T. P. (2006). Laurentide ice sheet meltwater and abrupt climate change during the last glaciation. *Paleoceanography*, *21*(1), 1–9. https://doi.org/10.1029/2005PA001186

Hönisch, B., Allen, K. A., Russell, A. D., Eggins, S. M., Bijma, J., Spero, H. J., et al. (2011). Planktic foraminifers as recorders of seawater Ba/Ca. *Marine Micropaleontology*, *79*(1–2), 52–57. https://doi.org/10.1016/j.marmicro.2011.01.003

Hughen, K. A., Overpeck, J. T., Lehman, S. J., Kashgarian, M., Southon, J., Peterson, L. C., et al. (1998). Deglacial changes in ocean circulation from an extended radiocarbon calibration. *Nature*, *391*(6662), 65–68. https://doi.org/10.1038/34150

Jeffries, M., Overland, J., & Perovich, D. (2013). The Arctic shifts to a new normal. *Physics Today*, *66*, 35. https://doi.org/10.1063/PT.3.2147

Johannessen, O. M., Bengtsson, L., Miles, M. W., Kuzmina, S. I., Semenov, V. A., Alekseev, G. V, et al. (2004). Arctic climate change: observed and modelled temperature and sea-ice variability. *Tellus A: Dynamic Meteorology and Oceanography*, *56*(4), 328–341.

Joung, D., & Shiller, A. M. (2014). Dissolved barium behavior in Louisiana Shelf waters affected by the Mississippi/Atchafalaya River mixing zone. *Geochimica et Cosmochimica Acta*, *141*, 303–313.

Katz, M. E., Cramer, B. S., Franzese, a., Honisch, B., Miller, K. G., Rosenthal, Y., & Wright, J. D. (2010). Traditional and Emerging Geochemical Proxies in Foraminifera. *The Journal of Foraminiferal Research*, *40*(2), 165–192. https://doi.org/10.2113/gsjfr.40.2.165

Keigwin, L. D., Jones, G. A., Lehman, S. J., & Boyle, E. A. (1991). Deglacial meltwater discharge, North Atlantic deep circulation, and abrupt climate change. *Journal of Geophysical Research*, *96*(C9). https://doi.org/10.1029/91jc01624

Keigwin, L. D., Klotsko, S., Zhao, N., Reilly, B., Giosan, L., & Driscoll, N. W. (2018). Deglacial floods in the Beaufort Sea preceded Younger Dryas cooling. *Nature Geoscience*, *11*(8), 599–604. https://doi.org/10.1038/s41561-018-0169-6

Kerr, R. A. (2012). Ice-free Arctic sea may be years, not decades, away. American Association for the Advancement of Science.

Lambeck, K., Esat, T. M., & Potter, E.-K. (2002). Links between climate and sea levels for the past three million years. *Nature*, *419*(6903), 199–206.

Leopold, L. B. (2002). Temperature profiles and bathymetry of some high mountain lakes. *Proceedings of the National Academy of Sciences*, *97*(12), 6267–6270. https://doi.org/10.1073/pnas.97.12.6267

Liu, Z., Carlson, A. E., He, F., Brady, E. C., Otto-Bliesner, B. L., Briegleb, B. P., et al. (2012). Younger Dryas cooling and the Greenland climate response to CO_2. *Proceedings of the National Academy of Sciences*, *109*(28), 11101–11104.

Livsey, C. M., Kozdon, R., Bauch, D., Brummer, G. J. A., Jonkers, L., Orland, I., et al. (2020). High-Resolution Mg/Ca and $\delta^{18}O$ Patterns in Modern *Neogloboquadrina pachyderma* From the Fram Strait and Irminger Sea. *Paleoceanography and Paleoclimatology*, *35*(9). https://doi.org/10.1029/2020PA003969

Lowell, T., Waterson, N., Fisher, T., Loope, H., Glover, K., Comer, G., et al. (2005). Testing the Lake Agassiz meltwater trigger for the Younger Dryas. *Eos, Transactions American Geophysical Union*, *86*(40), 365–372.

Mashiotta, T., Lea, D. W., & Spero, H. J. (1999). Glacial-interglacial changes in subantartic sea surface temperature and $\delta^{18}O$-water using foraminiferal Mg. *Earth and Planetary Science Letters*, *170*(May), 417–432.

Masson-Delmotte, V., Hou, S., Ekaykin, A., Jouzel, J., Aristarain, A., Bernardo, R. T., et al. (2008). A review of antarctic surface snow isotopic composition: Observations, atmospheric circulation, and isotopic modeling. *Journal of Climate*, *21*(13), 3359–3387. https://doi.org/10.1175/2007JCLI2139.1

McManus, J. F., Francois, R., Gherardl, J. M., Kelgwin, L., & Drown-Leger, S. (2004). Collapse and rapid resumption of Atlantic meridional circulation linked to deglacial climate changes. *Nature*, *428*(6985), 834–837. https://doi.org/10.1038/nature02494

Muscheler, R., Beer, J., Wagner, G., & Finkel, R. C. (2000). Changes in deep-water formation during the Younger Dryas event inferred from ^{10}Be and ^{14}C records. *Nature*, *408*(6812), 567–570.

Nørgaard Pedersen, N., Spielhagen, R. F., Erlenkeuser, H., Grootes, P. M., Heinemeier, J., & Knies, J. (2003). Arctic Ocean during the Last Glacial Maximum: Atlantic and polar domains of surface water mass distribution and ice cover. *Paleoceanography*, *18*(3).

Obbink, E. A., Carlson, A. E., & Klinkhammer, G. P. (2010). Eastern North American freshwater discharge during the Bølling-Allerød warm periods. *Geology*, *38*(2), 171–174. https://doi.org/10.1130/G30389.1

Oerlemans, J. (1982). Glacial cycles and ice-sheet modelling. *Climatic Change*, *4*(4), 353–374.

O'Neil, J., & Kim, S.-T. (1997). Equilibrium and nonequilibrium oxygen isotope effects in synthetic carbonates. *Geochimica et Cosmochimica Acta*, *61*(16), 3461–3475.

Peltier, W. R., Vettoretti, G., & Stastna, M. (2006). Atlantic meridional overturning and climate response to Arctic Ocean freshening. *Geophysical Research Letters*, *33*(6), 2–5. https://doi.org/10.1029/2005GL025251

Peltier, W. R. (2007). Rapid climate change and Arctic Ocean freshening. *Geology*, *35*(12), 1147–1148.

Poore, R. Z., Osterman, L., Curry, W. B., & Phillips, R. L. (1999). Late Pleistocene and Holocene meltwater events in the western Arctic Ocean, (August 2009), 759–762. https://doi.org/10.1130/0091-7613(1999)027<0759

Rooth, C. (1982). Hydrology and ocean circulation. *Progress in Oceanography*, *11*(2), 131–149. https://doi.org/10.1016/0079-6611(82)90006-4

Rudels, B., Anderson, L. G., & Jones, E. P. (1996). Formation and evolution of the surface mixed layer, *101*, 8807–8821.

Serreze, M. C., Walsh, J. E., Chapin, F. S., Osterkamp, T., Dyurgerov, M., Romanovsky, V., et al. (2000). Observational evidence of recent change in the northern high-latitude environment. *Climatic Change*, *46*(1), 159–207.

Stein, R. (2008). *Arctic Ocean sediments: processes, proxies, and paleoenvironment*. Elsevier.

Stein, R. (2011). The great challenges in Arctic Ocean paleoceanography. *IOP Conference Series: Earth and Environmental Science*, *14*, 12001. https://doi.org/10.1088/1755-1315/14/1/012001

Stuiver, M., Reimer, P.J., and Reimer, R.W., 2021, CALIB 8.2 [WWW program] at http://calib.org, accessed 2021-8-12

Tarasov, L., & Peltier, W. R. (2005). Arctic freshwater forcing of the Younger Dryas cold reversal. *Nature*, *435*(7042), 662–665.

Tarasov, L., & Peltier, W. R. (2006). A calibrated deglacial drainage chronology for the North American continent: evidence of an Arctic trigger for the Younger Dryas. *Quaternary Science Reviews*, *25*(7–8), 659–688. https://doi.org/10.1016/j.quascirev.2005.12.006

Teller, J. T., Leverington, D. W., & Mann, J. D. (2002). Freshwater outbursts to the oceans from glacial Lake Agassiz and their role in climate change during the last deglaciation. *Quaternary Science Reviews*, *21*(8–9), 879–887.

Teller, J. T., Boyd, M., Yang, Z., Kor, P. S. G., & Fard, A. M. (2005). Alternative routing of Lake Agassiz overflow during the Younger Dryas: New dates, paleotopography, and a re-evaluation. *Quaternary Science Reviews*, *24*(16–17), 1890–1905. https://doi.org/10.1016/j.quascirev.2005.01.008

Venegas, S. A., & Mysak, L. A. (2000). Is there a dominant timescale of natural climate variability in the Arctic? *Journal of Climate*, *13*(19), 3412–3434.

Vetter, L., Spero, H. J., Eggins, S. M., Williams, C., & Flower, B. P. (2017). Oxygen isotope geochemistry of Laurentide ice-sheet meltwater across Termination I. *Quaternary Science Reviews*, *178*, 102–117. https://doi.org/10.1016/j.quascirev.2017.10.007

Vinther, B. M., Buchardt, S. L., Clausen, H. B., Dahl-Jensen, D., Johnsen, S. J., Fisher, D. A., et al. (2009). Holocene thinning of the Greenland ice sheet. *Nature*, *461*(7262), 385–388.

SUPPLEMENTARY MATERIALS

Sample naming description:

Each set of samples that were run on for trace elements and subsequently for $\delta^{18}O_{calcite}$ were given a letter designation (A-O). As some intervals were run in multiple sets, these depths have multiple sample letters

associated with them. Letters correspond to sample names in LA-ICPMS data, as well as $\delta^{18}O$ results. For IRMS results that consisted of pooled shells, "A" or "B" were added after the sample letter to distinguish from data on single shells.

Depth interval	Letter designation
0.5	D
4.5	O
10.5	H, J
12.5	G, L
14.5	M
15.5	E, I
18.5	N
20.5	A, K
26.5	F
30.5	C
35.5	B

Table S1. Average measured and calculated geochemistry for samples from the eleven measured depth intervals in box core AOS17-b as well as the ranges for each component. The average values across all measured intervals and the average for meltwater pulse samples (10.5-20.5 cm) also shown below.

Depth (cm)	mean $\delta^{18}O_{cal}$ (‰ VPDB)	mean Mg/Ca (mmol/mol)	mean Ba/Ca (μmol/mol)	mean salinity (psu)	range Mg/Ca (mmol/mol)	range Ba/Ca (μmol/mol)	range $\delta^{18}O_{cal}$ (‰ VPDB)	range salinity (psu)
0.5	1.82	1.08	1.54	33.68	1.21	1.30	2.25	2.25
4.5	1.15	1.25	1.73	33.36	1.16	1.05	1.75	1.8
10.5	0.53	1.18	2.38	32.22	1.86	3.09	3.62	5.37
12.5	0.10	1.03	2.55	31.93	1.65	2.72	2.86	4.71
14.5	0.36	0.96	2.37	32.24	1.01	1.04	1.01	1.81
15.5	0.57	1.09	2.11	32.70	1.21	1.69	2.43	2.93
18.5	0.50	1.04	2.21	32.53	0.83	2.74	2.88	4.76
20.5	0.63	1.15	1.86	33.13	1.18	1.83	3.48	3.17
26.5	1.75	1.72	1.48	33.79	1.94	0.7	2.04	1.21
30.5	2.28	1.93	2.02	32.85	0.77	1.07	1.48	1.86
35.5	2.55	2.6	1.76	33.30	2.8	1.81	1.61	3.13
average	**1.91**	**1.37**	**1.70**	**33.39**	**1.42**	**1.19**	**1.83**	**2.05**

average MWP	**0.45**	**1.08**	**2.24**	**32.46**	**1.29**	**2.19**	**2.71**	**3.79**

Table S2. Measured $\delta^{18}O_{calcite}$, calculated $\delta^{18}O_{sw}$ using 2ºC, the coefficients from the $\delta^{18}O_{sw}$ vs. Ba/Ca-calculated salinity regressions for each depth interval, the Pearson's coefficient on the regressions, and the number of samples used to calculate the regressions.

Depth (cm)	mean $\delta^{18}O_{cal}$ (‰ VPDB)	mean $\delta^{18}O_{sw}$ (‰ VPDB)	y-int ($\delta^{18}O_{mw}$)	slope	Pearson coefficient	Number of samples
0.5	1.82	-1.16	no rel.	no rel.	-	12
4.5	1.15	-1.82	no rel.	no rel.	-	11
10.5	0.53	-2.45	-9.0	0.21	0.01	52
12.5	0.10	-2.88	-17.5	0.46	0.0001	52
14.5	0.36	-2.61	-15.2	0.39	0.01	12
15.5	0.57	-2.41	-19.1	0.51	0.01	24
18.5	0.50	-2.48	-12.1	0.30	0.02	28
20.5	0.63	-2.35	-23.9	0.65	0.001	31
26.5	1.75	-1.23	no rel.	no rel.	-	11
30.5	2.28	-0.64	no rel.	no rel.	-	13
35.5	2.55	-0.46	no rel.	no rel.	-	14

Table S3. Summary of radiocarbon dates obtained from *N. pachyderma* from core AOS 84b-17. Reservoir age of 800 was chosen based on estimates from Hanslik et al., 2010 and Dyke et al., 2011. Samples included were all *N. pachyderma* from AOS 84b-17 including those published in Poore (1999), and additional intervals measured in this study. The 20.5 cm interval includes three values: high Ba/Ca shells (H), low Ba/Ca shells (L), and then a typical "bulk" group (more details in Table S4).

Sample depth (cm)	raw ^{14}C age (measured)	Reference	reservoir age	ΔR (reservoir age-550)	corrected age (cal yr BP)
0	0	N/A	800	250	0
5.5	7150	Poore	800	250	5268
10.5	11690	Poore	800	250	10826
12.5	12250	Poore	800	250	11372
16.5	13040	Poore	800	250	12403
18.5	14454	This study	800	250	14397
20.5_L	14727	This study	800	250	14754

20.5_H	23344	This study	800	250	24518
20.5_bulk	20822	This study	800	250	21825
20.5	29400	Poore	800	250	30691
27.5	36970	Poore	800	250	38785
34.5	41480	Poore	800	250	41393

Table S4. Summary of subsamples of interval 20.5 cm that were analyzed individually for ^{14}C with the corrected ages using a reservoir age of 800 years.

Sample name	# shells	Ba/Ca level	average Ba/Ca (μmol/mol)	$\pm$2SD	calculated ^{14}C (cal. yr. BP)
20.5_L	35	low	1.17	0.43	14754
20.5_H	36	high	2.45	0.93	24518
20.5_bulk	51	mix	1.67	0.31	21825

Table S5. Summary of oxygen and carbon isotope measurements on all samples measured from AOS 94b-17 on individual *N. pachyderma* on at MPIC, and grouped shells at UC Davis (IRMS).

Depth Interval (cm)	Sample name	MPIC $\delta^{18}O$ measured (‰ VPDB)	MPIC $\delta^{13}C$ measured (‰ VPDB)		Depth Interval (cm)	Sample name	UCD IRMS $\delta^{18}O$ (‰ VPDB)	UCD IRMS $\delta^{13}C$ (‰ VPDB)
0.5	D1	2.430	0.563		4.5	O13	0.74	0.81
0.5	D2	1.080	1.194		4.5	O14	2.08	0.92
0.5	D3	1.142	1.940		4.5	O15	1.30	0.63
0.5	D4	2.360	0.152		4.5	O16	1.03	0.7
0.5	D5	1.940	1.181		4.5	O17	1.05	0.76
0.5	D6	1.080	0.306		4.5	O18	1.28	1.06
0.5	D7	3.040	0.133		4.5	O19	1.71	0.81
0.5	D12	1.290	1.355		4.5	O20	1.34	0.73
0.5	D13	2.110	-0.292		4.5	O21	0.93	0.94
0.5	D14	1.460	0.704		4.5	O22	0.88	0.96
0.5	D15	1.910	1.158		4.5	O23	0.33	0.95
0.5	D16	1.980	0.918		10.5	HA2	1.33	0.32
0.5	D18	0.790	0.934		10.5	H2	1.14	0.22
10.5	H1	1.144	0.401		10.5	HA8	1.18	0.51
10.5	H2	2.327	0.389		10.5	H8	1.549	0.25

10.5	H3	-0.068	0.257
10.5	H6	0.283	-0.025
10.5	H8	0.437	0.673
10.5	H9	-0.372	0.502
10.5	H11	0.269	0.917
10.5	H12	0.617	0.233
10.5	H14	1.382	0.634
10.5	H15	0.996	0.262
10.5	H16	0.054	0.175
10.5	H17	-0.765	0.539
10.5	H18	1.752	0.137
10.5	H20	1.676	0.000
10.5	H22	0.607	0.408
10.5	H24	-1.287	0.846
10.5	H25	3.261	0.051
10.5	H27	1.549	0.197
10.5	H40	0.058	-0.088
12.5	G1	0.596	0.164
12.5	G2	-0.159	0.270
12.5	G3	1.205	0.103
12.5	G4	1.736	0.261
12.5	G16	0.309	0.245
12.5	G18	1.916	-0.011
12.5	G19	1.201	0.146
15.5	E1	0.520	0.197
15.5	E3	0.010	-0.092
15.5	E4	-1.580	0.390
15.5	E6	0.740	0.311
15.5	E7	0.470	0.504
15.5	E8	1.190	0.375
15.5	E9	1.300	0.459
15.5	E10	-0.820	0.175
15.5	E16	0.890	0.377
15.5	E18	-0.620	0.983
20.5	A2	2.520	0.117
20.5	A3	1.790	-0.170
20.5	A5	0.710	0.354
20.5	A6	0.020	0.191
20.5	A9	0.442	0.126

10.5	H12	1.16	0.42
10.5	HA13	0.41	0.36
10.5	H13	1.03	0.58
10.5	HA15	0.79	0.36
10.5	H15	0.98	0.11
10.5	H16	1.15	0.22
10.5	HA17	1.71	0.86
10.5	H17	1.6	0.25
10.5	HA18	-0.77	0.51
10.5	H18	1.18	0.51
10.5	H19	1.04	0.2
10.5	H20	-0.14	0.25
10.5	H21	-0.25	0.49
10.5	H22	-0.66	0.21
10.5	HB1	0.07	-0.4
10.5	HB2	-0.34	0.15
10.5	HB3	-0.23	0.17
10.5	HB4	0.26	0.07
10.5	HB5+15	1.08	0.36
10.5	HB6	0.7	0.26
10.5	HB7	-0.07	0.16
10.5	HB8	0.25	0.03
10.5	HB9	1.02	-0.27
10.5	HB10	1.25	-0.11
10.5	HB11	0.25	0.39
10.5	HB12	0.08	-0.09
10.5	HB13	0.99	0
10.5	HB14	1.47	0.33
10.5	HB17	-0.71	0.54
10.5	HB16+18	0.14	0.68
10.5	HB20	0.86	0.16
12.5	G1	0.98	0.12
12.5	G2	1.65	-0.03
12.5	G3	0.02	0.14
12.5	G5	-0.8	0.32
12.5	G6	-0.8	0.28
12.5	G7	1.65	0.05
12.5	G8	-0.96	0.31
12.5	GA1	1.83	0.34

20.5	A11	-0.557	-0.023
20.5	A12	-0.991	-0.070
20.5	A14	0.300	0.210
20.5	A16	0.330	0.120
20.5	A18	-0.328	-0.166
20.5	A23	-0.324	0.098
20.5	A26	-0.198	-0.113
20.5	A27	0.030	0.119
20.5	A28	-0.080	-0.550
20.5	A30	0.520	-0.330
20.5	A31	2.840	0.160
20.5	A32	0.890	-0.110
20.5	A33	2.190	0.070
20.5	A34	-0.080	-0.550
20.5	A37	0.572	-0.127
20.5	A38	2.385	-0.079
20.5	A40	-0.495	0.087
26.5	F1	0.840	0.836
26.5	F3	2.880	0.697
26.5	F5	0.950	0.562
26.5	F8	2.250	0.842
26.5	F9	2.280	1.021
26.5	F10	1.240	0.783
26.5	F11	1.790	0.839
26.5	F12	1.090	0.694
26.5	F14	1.650	1.554
26.5	F18	2.440	0.942
30.5	C1	2.920	1.065
30.5	C3	2.950	0.805
30.5	C4	2.350	0.516
30.5	C5	1.640	1.099
30.5	C6	2.240	1.162
30.5	C7	2.243	0.876
30.5	C13	1.785	1.122
30.5	C14	2.734	1.081
30.5	C16	2.635	0.868
30.5	C17	1.472	0.851
30.5	C18	2.426	0.845
30.5	C19	2.586	0.883

12.5	GA2	1.5	0.33
12.5	GA3	0.36	0.89
12.5	GA4	0.93	0.6
12.5	GA5	-0.14	0.36
12.5	GA6	-0.22	0.12
12.5	GA7	-0.03	0.37
12.5	GA8	-1.03	0.63
12.5	G9	-0.56	-0.16
12.5	G10	-0.08	0.27
12.5	G11	-0.01	-0.06
12.5	G12	-0.58	0.31
12.5	G13	-0.01	0.25
12.5	G14	-0.26	0.28
12.5	G15	-1.04	0.24
12.5	GA1	1.84	0.4
12.5	GB1	1.18	-0.11
12.5	GA2	1.51	0.38
12.5	GB2	0.05	-0.15
12.5	GA3	0.9	0.42
12.5	GB3	-0.66	-0.05
12.5	GA4	0.94	0.65
12.5	GB4	0.5	-0.1
12.5	GA5	-0.13	0.41
12.5	GB5	-0.03	0.05
12.5	GA6	-0.2	0.18
12.5	GB6	1.53	-0.15
12.5	GA7	-0.02	0.43
12.5	GB7	-0.49	0.11
12.5	GA8	-1.01	0.69
12.5	GB8	-0.88	-0.11
12.5	GA9	-0.55	-0.11
12.5	GB9	-0.69	0.09
12.5	GA10	-0.06	0.33
12.5	GB10	-0.19	0.15
12.5	GA11	0	0
12.5	GB11	1.13	0.4
12.5	GA12	-0.57	0.36
12.5	GB12	-0.27	0.09
12.5	GA13	0.01	0.3

35.5	B1	2.298	0.713
35.5	B5	2.876	1.067
35.5	B6	2.662	0.991
35.5	B7	2.682	1.180
35.5	B9	2.519	1.109
35.5	B12	2.347	0.942
35.5	B13	2.461	1.019
35.5	B14	2.448	0.967
35.5	B15	2.189	0.998
35.5	B16	2.053	1.072
35.5	B17	2.879	0.901
35.5	B18	1.804	0.658
35.5	B19	3.412	0.720

12.5	GB13	-0.23	0.08
12.5	GA14	-0.25	0.33
12.5	GB14	-0.79	-0.1
12.5	GA15	-1.02	0.3
12.5	GB15	0.42	-0.4
12.5	GB16	0.87	-0.1
12.5	GB17	-0.16	-0.1
12.5	GB18	-0.28	0.09
12.5	GB19	-0.05	-0.2
14.5	M1	0.70	0.18
14.5	M2	0.72	-0.15
14.5	M3	0.06	0.25
14.5	M4	0.88	0.01
14.5	M5	-0.03	0.08
14.5	M6	-0.12	0.2
14.5	M7	0.11	0.22
14.5	M8	0.41	0.05
14.5	M9	0.21	-0.02
14.5	M10	0.14	0.2
14.5	M11	0.89	0.13
14.5	M12	0.42	0.15
15.5	E19	1.71	0.81
15.5	E1	1.3	-0.3
15.5	E3	0.445	0.08
15.5	IB1	0.11	0.06
15.5	IB2	1.3	-0.3
15.5	IB3	0.44	0.08
15.5	IB4	1.81	0.06
15.5	IB5+6	0.86	0.19
15.5	IB7+8	-0.28	0.24
15.5	IB9+10	0.75	0.06
15.5	IB11	1.18	0.19
15.5	IB12+13	-0.09	0.33
15.5	IB14+15	0.25	-0.1
15.5	IB16	-0.46	0.61
15.5	IB17	0.98	0.97
15.5	IB18	1.16	1.17
15.5	IB19	-0.32	0.37
18.5	N1	1.55	0.04

18.5	N2	0.72	0.25
18.5	N3	0.42	0.21
18.5	N4	0.75	0.14
18.5	N5	0.94	0.09
18.5	N6	2.24	-0.17
18.5	N7	-0.29	0.01
18.5	N8	1.6	0.19
18.5	N9	2.25	-0.1
18.5	N10	-0.34	1.13
18.5	N11	-0.4	0.25
18.5	N13	0.85	0.01
18.5	N14	0.82	0.17
18.5	N15	0.55	0.07
18.5	N16	-0.51	0.25
18.5	N17	0.55	0.06
18.5	N18	0.05	-0.04
18.5	N19	-0.44	0
18.5	N20	0.87	0.02
18.5	N21	0.73	0.63
18.5	N22	0.34	0.02
18.5	N23	1.11	-0.07
18.5	N24	-0.04	0
18.5	N25	-0.16	0.24
18.5	N27	-0.63	0.26
18.5	N28	0.3	0.28
18.5	N29	-0.52	-0.03
18.5	N30	0.57	0.13
20.5	A2	1.51	0.1
20.5	KB1	2.64	0.1
20.5	KB2	1.54	0.05
20.5	KB3	0.63	0.57
20.5	KB4	-0.16	0.17
20.5	KB5	0.5	-0.03
20.5	KB6	0.69	0.36
20.5	KB7	0.89	0.22
20.5	KB8	2.74	0.5
20.5	KB9	0.55	-0.03
20.5	KB10	0.99	-0.06
20.5	KB11	-0.08	0.19

20.5	KB12	0.75	0.21
20.5	KB13	0.04	0.19
20.5	KB14	0.15	0.37
20.5	KB15	-0.47	0.67
20.5	KB16	1.08	0.19
20.5	KB17	-0.84	-0.02
20.5	KB18	1.16	0.2
26.5	F9	1.97	0.76
26.5	F10	1.66	0.22
26.5	F11	2.65	0.73
26.5	F12	0.67	0.97
26.5	F13	0.88	0.98
26.5	F16	0.58	0.89
26.5	F15	2.03	1.16

Table S6. Calculated y-intercepts ($\delta^{18}O_{mw}$) for the meltwater-influenced depth intervals across various temperatures with 2σ standard error on each of the regressions.

Interval (cm)	Temperature (ºC)	y-intercept	2σ std. error
10.5	0	-10.08	0.21
12.5	0	-17.60	0.06
14.5	0	-16.32	0.05
15.5	0	-20.13	0.07
18.5	0	-13.14	0.09
20.5	0	-24.93	0.10
10.5	2	-9.52	0.21
14.5	2	-15.76	0.05
12.5	2	-17.05	0.06
15.5	2	-19.57	0.07
18.5	2	-12.58	0.09
20.5	2	-24.37	0.10
10.5	4	-8.97	0.21
12.5	4	-16.50	0.06
14.5	4	-15.22	0.05
15.5	4	-19.03	0.07
18.5	4	-12.04	0.09
20.5	4	-23.83	0.10

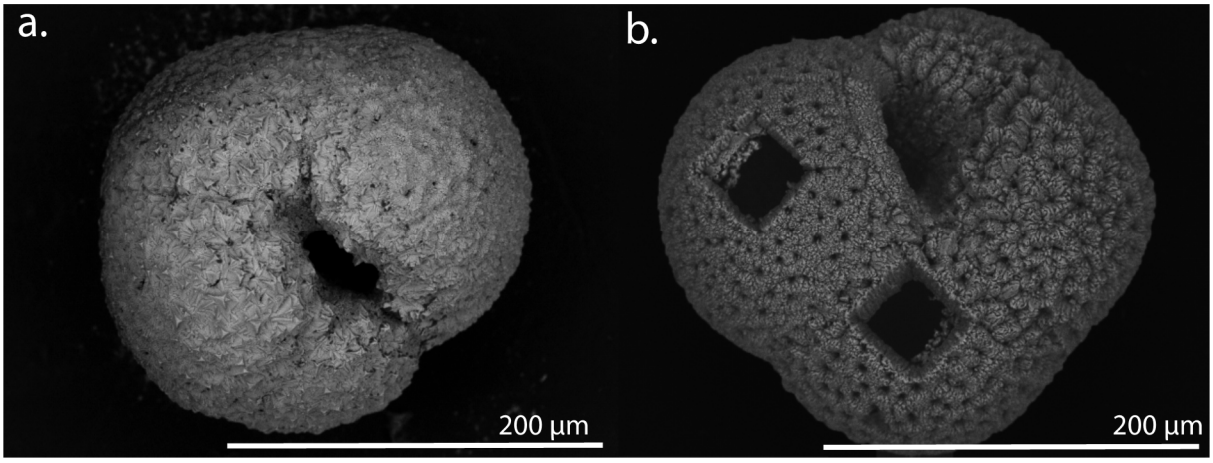

Figure S1. Scanning electron micrographs of representative *N. pachyderma* samples analyzed from box core AOS 84b-17. (a) whole shell after oxidative cleaning and (b) shell after LA-ICPMS analysis with two square ablation spots evident on two newest chambers.

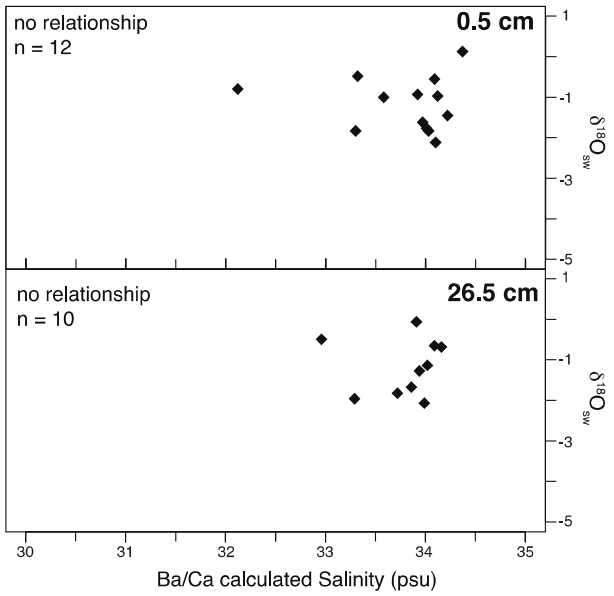

Figure S2. Compilation of Ba/Ca calculated salinity vs. $\delta^{18}O_{sw}$ regressions for two intervals outside of the YD meltwater pulse within AOS94b-17.

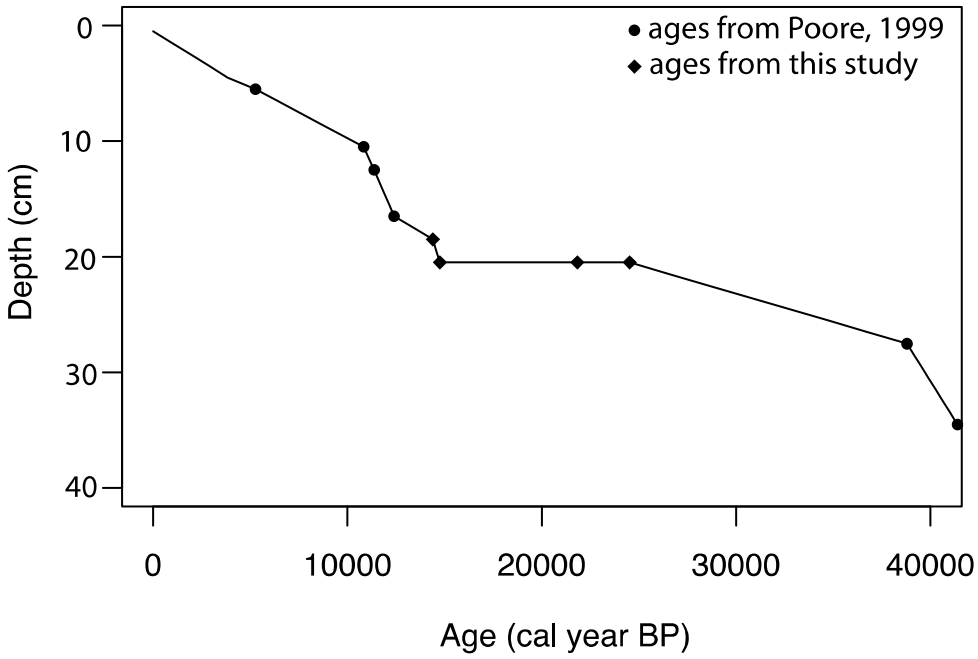

Figure S3. Age model for boxcore AOS 84b-17 based on ^{14}C ages measured by Poore (1999) and in this study, with a reservoir age of 800 years. Corrected ages (cal year BP) shown for sampled intervals with Poore data shown in circles, and new data from this study in diamonds. Three ages are shown for depth interval 20.5 cm as discussed in the text.

Methods for combining shells for IRMS $\delta^{18}O$:

Samples analyzed for $\delta^{18}O$ on the UC Davis common acid bath dual-inlet mass spectrometer (CABDI) were picked, cleaned, and analyzed for trace elements following the same methods as all other samples (described in methods). Following LA-ICPMS analysis, samples were roasted at 325ºC for 30 minutes to remove any remnant carbon tape, and then individually weighed using a microbalance. Reduced trace element data (averages for each foraminifera) were sorted by Ba/Ca concentrations, and two to five shells were grouped together to obtain masses between 15-25 μg. Mg/Ca concentrations were also scrutinized to ensure that no shells were grouped together if they had over 1 mmol/mol difference in Mg/Ca. For each CABDI sample, the average trace element concentrations for each shell included in the sample were averaged together to obtain single TE/Ca values for that sample.

Methods prior to additional ^{14}C analysis:

Approximately 40 shells from interval 18.5, and ~100 shells from 20.5 cm were picked from the dried 125 μm fraction and oxidatively cleaned following the same methods as other samples. Approximately 70 of the shells from 20.5 cm were analyzed for trace elements as described in the methods. After LA-ICPMS analyses, shells were removed from carbon tape, roasted at 325 ºC for 30 min to remove remnant carbon tape, and then split into two samples by their Ba/Ca concentrations. All shells with average Ba/Ca> 2 μmol/mol were combined in one sample (high Ba/Ca), while all shells < 2 μmol/mol were combined into a "low" sample. These samples subsequently produced ^{14}C ages and were reservoir corrected and converted to calendar years BP using the CALIB program. Data from the 20.5 cm samples shown in Table S4. For the age model, the new ages from the 18.5 cm and 20.5 cm samples were combined with the previous ages presented by Poore (1999). For 20.5 cm, the three new ages were used, with the intervals before and after the 20.5 cm interval interpolated using the youngest and oldest of the measured ages respectively. Between each measured depth, a sedimentation rate is calculated and used to calculate other depths between the measurements. Age model shown in Figure S2.